



State University of Londrina
Center of Technology and Urbanization
Department of Electrical Engineering
Electrical Engineering Master Program

Lígia May Taniguchi

Channel Modeling and Combiner Design For Massive MIMO and Extra
Large Scale MIMO Systems with Impairment

Londrina,
June 14, 2021

Lígia May Taniguchi

Channel Modeling and Combiner Design For Massive MIMO and Extra
Large Scale MIMO Systems with Impairment

A Dissertation submitted to the Electrical Engineering Graduate Program at the State University of Londrina in fulfillment of the requirements for the degree of Master of Science in Electrical Engineering.

Area: Telecommunications Systems

Supervisor: Taufik Abrão

Londrina,
June 14, 2021

Taniguchi, Lígia May

Channel Modeling and Combiner Design For Massive MIMO and Extra Large Scale MIMO Systems with Impairment. Londrina, 2021. 132 p.

Supervisor: Taufik Abrão

Dissertation (Master of Science) – Department of Electrical Engineering – State University of Londrina

1. Massive MIMO Systems, 2. XL-MIMO systems, 3. Randomized Kaczmarcz, 4. Combining, 5. Telecommunications Systems

Lígia May Taniguchi

Channel Modeling and Combiner Design For Massive MIMO and Extra
Large Scale MIMO Systems with Impairment

A Dissertation submitted to the Electrical Engineering Graduate Program at the State University of Londrina in fulfillment of the requirements for the degree of Master of Science in Electrical Engineering.

Area: Telecommunications Systems

Examination Board

Dr. Taufik Abrão
Department of Electrical Engineering
State University of Londrina
Supervisor

Dr. José Carlos Marinello Filho
Department of Electrical Engineering
UTFPR - CP
External Member

Dr. Paulo Rogério Scalassara
Department of Electrical Engineering
UTFPR - CP
External Member

Londrina,
June 14, 2021

Acknowledgements

First, I would like to thank my advisor, professor Taufik Abrão, for his contribution to the development of this work.

To my parents, Maria Neusa and Gilberto, to my sisters, Maiara, Karen, Emy and Laís, and to my boyfriend, Bruno, for their support and understanding throughout the process, which were essential for the completion of the work.

To my friends and lab colleagues, for the fellowship and good times, making this process much lighter and more pleasant.

To the State University of Londrina for the support for the development of the work.

This study was financed in part by the Coordenação de Aperfeiçoamento de Pessoal de Nível Superior - Brasil (CAPES) - Finance Code 001.

Abstract

With hundreds of antennas, Massive MIMO (M-MIMO) is the main candidate to increase substantially the capacity in wireless communication systems. In addition to M-MIMO, another operating regime recently proposed in the literature is the so-called extra large MIMO (XL-MIMO), where the antenna elements are arranged in a large dimension structure. Both M-MIMO and XL-MIMO are challenging in terms of implementation, since channel measures demonstrate that increasing the number of antennas results in some characteristics not observed with a small number of antennas, *e.g.*, the *hardening channel* and *favorable propagation* phenomenon. Among the challenges are the choice of the appropriate combination scheme and channel modeling, both addressed in this work. Regarding the channel models, in this academic work we compared the stochastic models based on correlation *against* geometry-based models, where both are evaluated in the context of M-MIMO and XL-MIMO systems. The analyzes show that the models based on geometry represent more accurately a propagation environment than a model based on correlation; however, the implementation of the geometry-based models presents further challenging due to the computational complexity of this model being much higher than those channel correlation-based models. For the combiner schemes analyses, accuracy of channel modeling is paramount, because it can state that the emulated environment (channel and system) ensures that the estimated performance is close to the real one. Thus, when evaluating the combination schemes, we compare the performance between the channel models based on geometric *versus* correlation. Due to the large number of antennas in both analysed systems (M-MIMO or XL-MIMO), the combiner schemes must present very low computational complexity. Thus, the maximum ratio combining (MRC), zero-forcing (ZF) and regularized ZF (RZF) schemes are evaluated, where the last one is modeled by the randomized iterative Kaczmarz (rKA) algorithm in the last part of this work. As a result, all of these schemes have low computational complexity; however, a fourth scheme of high complexity called multicell MMSE (M-MMSE) also is evaluated due to the unlimited spectral efficiency presented in the literature, *i.e.*, it is able to eliminate the pilot contamination. These schemes are analyzed for spectral and energy efficiency.

Keywords: massive MIMO (M-MIMO); Extra-large MIMO (XL-MIMO); stochastic channel models; randomized Kaczmarz; M-MMSE combining.

Resumo

Com centenas de antenas, *massive MIMO* (M-MIMO) é o principal candidato para aumentar substancialmente a capacidade dos sistemas de comunicação sem fio. Além de M-MIMO, outro regime operacional recentemente proposto na literatura é o chamado *extra large MIMO* (XL-MIMO), onde os elementos da antena são dispostos em uma estrutura de grande dimensão. Ambos os sistemas, M-MIMO e XL-MIMO, apresentam desafios para implementação, pois as medidas de canal demonstram que o aumento do número de antenas resulta em algumas características não observadas com um pequeno número de antenas, *e.g.*, o *hardening channel* e *favorable propagation*. Entre os desafios estão a escolha do esquema de combinação apropriado e a modelagem de canais, ambos abordados neste trabalho. Em relação aos modelos de canal, neste trabalho, nós comparamos os modelos estocásticos baseados em correlação *versus* os modelos baseados em geometria, onde ambos são avaliados no contexto dos sistemas M-MIMO e XL-MIMO. As análises mostram que os modelos baseados na geometria representam com mais precisão um ambiente de propagação do que um modelo baseado na correlação; no entanto, a implementação dos modelos baseados em geometria apresenta mais desafios, devido à complexidade computacional desse modelo ser muito maior do que os modelos baseados em correlação de canais. Para as análises de esquemas de combinação, a precisão da modelagem de canais é fundamental, pois pode garantir que o ambiente emulado (canal e sistema) garanta que o desempenho estimado seja próximo ao real. Assim, ao avaliar os esquemas de combinação, comparamos o desempenho de acordo com os modelos de canais baseados em correlação *versus* geométricos. Devido ao grande número de antenas nos dois sistemas (M-MIMO e XL-MIMO), os esquemas de combinação devem apresentar complexidade computacional muito baixa. Assim, são avaliados os esquemas maximum-ratio combining (MRC), zero-forcing (ZF) e o regularized ZF (RZF), sendo o último modelado pelo algoritmo iterativo randomized Kaczmarz (rKA). Como resultado, todos esses esquemas têm baixa complexidade computacional; no entanto, um quarto esquema de alta complexidade chamado MMSE multicelular (M-MMSE) também é avaliado devido à eficiência espectral ilimitada apresentada na literatura, ou seja, é capaz de eliminar a contaminação piloto. Esses esquemas são analisados quanto à eficiência espectral e energética.

Palavras-chave: extra-large mimo; modelos de canais estocásticos; randomized Kaczmarz; combinador M-MMSE.

List of abbreviations and acronyms

5G	5th Telecommunication Generation
AoA	Angle-of-Arrive
AWGN	Additive White Gaussian Noise
BS	Base Station
CN	Condition Number
GBSM	Correlation-Based Stochastic Model
EE	Energy Efficiency
GBSM	Geometry-Based Stochastic Model
MIMO	Multiple-Input Multiple-Output
M-MIMO	Massive Multiple-Input Multiple-Output
XL-MIMO	Extra Large Multiple-Input Multiple-Output
M-MMSE	Multicell Minimum Mean-Square Error
MMSE	Minimum Mean-Square Error
MRC	Maximal-ratio combining
RKZF	Randomized Kaczmarz Regularized Zero-Forcing
RZF	Regularized Zero-Forcing
SE	Spectral Efficiency
SINR	Signal-To-Interference-Plus-Noise Ratio
SNR	Signal-to-Noise Ratio
SVD	Singular Value Decomposition
UE	User Equipment
UL	Uplink
ULA	Uniform Linear Array
UPA	Uniform Planar Array

VR Visibility Region

ZF Zero-Forcing

List of Notations

- a** vectors are denoted by lower case bold letters;
- A** matrices are denoted by upper case bold letters;
- $[\mathbf{A}]_{j,k}$ element present in the j th row and k th column of **A**
- \mathbf{A}^{-1} matrix inversion;
- \mathbf{A}^T matrix transposition;
- \mathbf{A}^H Hermitian operation;
- $\|\mathbf{A}\|_2$ norm-2 of **A**;
- \mathbf{I}_N $N \times N$ identity matrix;
- i $\sqrt{-1}$
- \setminus set exclusion

List of Symbols

- M number of antennas at base station;
- K number of user equipment;
- d distance between the transmitter and the receiver;
- χ fluctuations of the shadowing;
- α path loss exponent;
- \mathcal{L}_0 channel average gain;
- τ_c number of samples of the coherence block;
- τ_d length of the downlink data;
- τ_p length of the pilot sequence;
- τ_u length of the uplink data;
- ρ_{ul} Pilot signal power;
- ϕ Pilot sequence;
- σ_{ul} Standard Deviation of Received Noise;
- Φ_{li}^j correlation matrix of the estimated channel;
- γ SINR;
- ρ Correlation factor ;
- σ_{shad} Standard Deviation of Shadowing;
- ξ RZF regularization factor;
- θ Azimuth angle;
- \mathcal{L} Path loss term;
- f Pilot reuse factor;
- η SNR;
- B_T Total bandwidth;
- C_b Number of active clusters;

List of Figures

Figure 1.1 – Signal Propagation in an urban environment, where the UE is surrounded by compact and large antennas arrays.	31
Figure 1.2 – Cross-correlation. (a) Correlated Signals. (b) Uncorrelated Signals.	32
Figure 1.3 – Antenna array sketch indicating the correlation between antennas.	33
Figure 1.4 – Antenna array arrangement identifying the correlation between antennas.	34
Figure 1.5 – Uniform Linear Array.	35
Figure 1.6 – Uniform Planar Array.	36
Figure 2.1 – Stochastic Channel Models.	44
Figure 2.2 – Geometry-based Stochastic Model in Uplink mode where the BS is equipped with linear array. The BS and user are far, thus, the wavefront can be approximated to a plane.	46
Figure 2.3 – Typical XL-MIMO scenario: each cluster defines the VR length (L_{VR_j}) in the antennas array.	50
Figure 2.4 – Adopted channel clustering distribution following two representative scenarios.	51
Figure 2.5 – CBSM exponential model. Capacity as a function of a) number of antennas; (b) correlation factor assuming $M = 100$	55
Figure 2.6 – Uncorrelated fading: a) Upper bound of capacity \times number of antennas for different values of standard deviation of shadowing (σ_{shad}); b) Shadowing amplitude when the standard deviation is increased.	55
Figure 2.7 – Correlated-based stochastic	56
Figure 2.8 – Capacity analysis in geometric-based stochastic models (GBSM) according to the AoA considering ULA arrangements. a) Illustration of the relation between capacity and nominal AoA. b) Capacity analysis <i>vs</i> AoA and Δ	58
Figure 2.9 – a) Condition number when the angular spread is increased; b) Singular values for different angular spread.	59
Figure 2.10–One-ring model with $M = 100$ antennas. Capacity analysis according to a) Δ ; b) AoA; c) number of antennas; d) distance between antennas.	60
Figure 2.11–Singular values decomposition analysis for the GBSM Gaussian local scattering model	61
Figure 2.12–Gaussian Local Scattering Model (approximate expression). Capacity analysis according to: a) ASD; b) AoA; c) increasing M ; d) normalized distance between antennas.	62

Figure 2.13–One-ring Model with UPA. Capacity analysis according to: a) the nominal angles of azimuth and elevation; b) increasing M_h and M_v simultaneously; c) the azimuth nominal angle; d) increasing the horizontal and vertical spacing between the antennas.	64
Figure 2.14–Gaussian Model where BS is equipped with UPA. Capacity according to: a) increasing the number of antennas; b) azimuth nominal angle.	65
Figure 2.15–Average correlation coefficient according to the ULA number of antennas : channel measurement vs CBSM and GBSM channel models with adjusted parameters.	67
Figure 2.16–VR generation algorithm considering ULA with $M = 33$ antennas: a) Example of three VR, where the obstacles result in a received power equal to zero; b) histogram of the number of active antennas.	68
Figure 2.17–Attainable SINR as a function of number of users (K) for two schemes of clusters distribution: a) Correlation matrix \mathbf{R} is modelled by Uncorrelated and One-ring models; b) \mathbf{R} is modelled by Exponential channel model. c) Second scheme of clusters distribution: \mathbf{R} is modeled by Uncorrelated and One-ring model; d) \mathbf{R} is modeled by Exponential channel model.	70
Figure 3.1 – Geometric illustration of how the combining vector \mathbf{v}_{jk} can reject the channel from the interfering user $\hat{\mathbf{h}}_{li}^j$	77
Figure 3.2 – Simulation scenario.	78
Figure 3.3 – SE analysis according to the number of antennas (a) and SNR (b).	79
Figure 3.4 – Sketch of the uplink XL-MIMO system: (top) Combiner and channel estimation blocks; (botton) the double-scattering channel model; (in between) M -antennas linear array with B subarrays. The distance between linear scattering-elements is d_s , while d_r holds for distance between antenna elements at BS.	83
Figure 3.5 – MSE \times Iterations for the rKA-emulating the RZF combiner, $K \in [16, 32, 64]$ users.	90
Figure 3.6 – Interference analysis between two users, considering the a) double-scattering b) single-scattering model.	91
Figure 3.7 – Sketch of the scenario for the SE versus SNR analysis.	93
Figure 3.8 – SE vs SNR, considering the ZF and MMSE combiner, where $C = [1; 8; 12; 16]$ clusters, $M = 256$ antennas.	94
Figure 3.9 – SE \times VR length, for the RKZF, ZF and MMSE combiners and different VR profiles and θ	97
Figure 3.10–EE vs VR length, considering the RKZF, ZF and MMSE combiner ($\theta = 5^\circ$).	98

List of Tables

Table 1.1 – Path loss exponent for different environments.	30
Table 1.2 – Standard deviation of shadow fading.	30
Table 2.1 – Parameter values adopted in the numerical simulations for M-MIMO and XL-MIMO channels.	54
Table 2.2 – Parameter values adopted for CBSMs.	54
Table 2.3 – Adopted values for GBSMs channel parameters.	57
Table 2.4 – Parameter values adopted in the numerical simulations for channel cor- relation analysis.	66
Table 3.1 – Parameter values adopted in the numerical simulations.	77
Table 3.2 – Parameters values adopted for MSE evaluation.	89
Table 3.3 – Parameters values adopted for SE \times SNR evaluation.	92
Table 3.4 – Parameters values adopted for EE, SE \times M analysis.	96

Contents

1	INTRODUCTION	27
1.1	Concepts and Motivation	27
1.1.1	Scenarios and Fading	29
1.1.2	Correlation	31
1.1.3	Statistical Channel Models	34
1.1.3.1	Correlation-based Stochastic Models (CBSM)	34
1.1.3.2	2D Geometry-based Stochastic Models (GBSM)	35
1.1.3.3	3D Geometry-based Stochastic Models (GBSM)	36
1.1.3.4	Extra Large Scale Massive MIMO Channels	36
1.1.4	Figures of Merit	37
1.1.4.1	Capacity	37
1.1.4.2	MSE-RKZF Metric	37
1.1.4.3	Interference between users	37
1.1.4.4	Spectral Efficiency in XL-MIMO with Linear Combiners	38
1.1.4.5	Energy Efficiency (EE)	39
1.2	Goals	40
1.2.1	General Goals	40
1.2.2	Specific Goals	41
1.3	Organization of the text	41
1.3.1	Contributions	41
2	CHANNEL MODELS	43
2.1	Channel Models for M-MIMO and XL-MIMO	43
2.1.1	CBSM	43
2.1.1.1	Exponential Spatial Correlation	44
2.1.1.2	Uncorrelated Fading with Large-Scale Fading	44
2.1.1.3	Exponential Spatial Correlation with Large-Scale Fading	44
2.1.2	2D GBSM	45
2.1.2.1	One-ring Model	46
2.1.2.2	Gaussian Local Scattering Model	47
2.1.3	3D GBSM	48
2.1.3.1	One-ring Model	48
2.1.3.2	Gaussian Local Scattering Model	49
2.1.4	Extreme Large Massive MIMO Channels	49
2.1.5	Downlink Transmission in XL-MIMO with Linear Precoding	52

2.2	Numerical Results	53
2.2.1	CBSM	53
2.2.1.1	Exponential	53
2.2.1.2	Uncorrelated Fading	53
2.2.1.3	Exponential Model with Large Scale Fading	56
2.2.2	GBSM	56
2.2.2.1	One-ring Model with ULA	57
2.2.2.2	Gaussian Model with ULA	59
2.2.3	3D Models	62
2.2.3.1	One-ring Model with UPA	62
2.2.3.2	Gaussian Model with UPA	63
2.2.4	CBSM and GBSM Compared to Channel Measurements	65
2.2.5	XL-MIMO channel model	67
2.3	Conclusions	70
3	LINEAR COMBINERS FOR MASSIVE AND EXTRA LARGE SCALE MIMO	73
3.1	Massive MIMO systems	73
3.1.1	Uplink mode for M-MIMO systems	73
3.1.2	Linear Combiners	74
3.1.2.1	MRC Scheme	74
3.1.2.2	ZF Combining Scheme	75
3.1.2.3	M-MMSE Combining Scheme	75
3.1.3	Asymptotic Analysis	75
3.1.4	Illustrative Numerical Results	77
3.2	Extra Large MIMO systems	79
3.2.1	System Model	79
3.2.1.1	Uplink XL-MIMO	79
3.2.2	Channel Model	81
3.2.2.1	Double-scattering Model	81
3.2.2.2	Single-scattering Model	82
3.2.3	Processing Each Subarray	84
3.2.4	Linear Combiners	84
3.2.4.1	Zero-forcing Combiner (ZF) for XL-MIMO	84
3.2.4.2	Randomized Kaczmarz Regularized Zero-Forcing (rKZF)	85
3.2.4.3	MMSE Combiner for XL-MIMO	88
3.2.5	Numerical Results	88
3.2.5.1	Mean Squared Error of XL-MIMO Channel Estimates	89
3.2.5.2	Favourable Propagation in XL-MIMO	90
3.2.5.3	Spectral Efficiency in XL-MIMO Single-scattering Model	91

3.2.5.4	Energy Efficiency in XL-MIMO with Linear Combiners	95
3.3	Conclusions	95
4	CONCLUSIONS AND FUTURE DIRECTIONS	99
	BIBLIOGRAPHY	101
	 APPENDIX	 107
	APPENDIX A – FULL PAPER PUBLISHED IN THE JOURNAL ” <i>TRANSACTIONS ON EMERGING TELECOMMUNICATIONS TECHNOLOGIES</i> ”	109
	APPENDIX B – FULL PAPER SUBMITTED IN THE JOURNAL ” <i>TRANSACTIONS ON EMERGING TELECOMMUNICATIONS TECHNOLOGIES</i> ”	111

1 Introduction

In this chapter, we introduce some basic concepts used in the course of the work. We present concepts related to the characteristics of the channels and some figures of merit. At the end of the chapter, we present the objectives of the work and the organization of the dissertation text.

1.1 Concepts and Motivation

In the last decades, wireless communications have become increasingly indispensable, so numerous applications have been created improving the demand of capacity and reliability of wireless system (LU et al., 2014). One way to develop these requirements is applying the Massive MIMO (M-MIMO) technology, considered the key technology, in which tens or hundreds of antennas are employed at the Base Station (BS) (LARSSON et al., 2014). With an even greater number of antennas and a large array size, a system called extra large scale massive MIMO (XL-MIMO) has recently been proposed. In this system, it is possible to obtain a better performance, as it allows the spatial multiplexing of a large number of users in the same time-frequency resources (AMIRI et al., 2020).

The fact of M-MIMO and XL-MIMO have many hundreds or thousands of antennas impacts in some unique characteristics, such as favorable propagation, hardening channel (MARZETTA et al., 2016), elevation characteristics due to 2D or 3D antennas array, spherical wave-front assumption (TAMADDONDAR; NOORI, 2017) and spatial non-stationarity (ALI et al., 2019; CARVALHO et al., 2019). The favorable propagation offer a mutual orthogonality between channel vectors and hence linear signal processing techniques result in an optimal performance (MARZETTA et al., 2016) (BJÖRNSON et al., 2016). The antenna elements may be arranged in different structures and generate a radiation pattern according to its structure (VESA et al., 2015). Most works consider a uniform linear array (ULA) structure; however, only 2D or 3D structures such as uniform planar array (UPA) and uniform cylindrical array (UCA) offer control of angle of elevation, resulting in an increase of spatial resolution, *i.e.*, an increasing on the desired signal strength and reduction in users' interference (ZHENG et al., 2014). The spherical wave channel modeling based on electromagnetic field describes with more accuracy the near-field propagation if compared to plane-wave propagation; hence the models present different results in capacity (MIAO et al., 2018) (TAMADDONDAR; NOORI, 2017). Moreover, the non-stationary properties of the channel clusters can be observed over the large antenna arrays due to the possibility of different antenna elements observe different sets of clusters (CHEN et al., 2017). This property is paramount in scenarios XL-MIMO and must be considered from a spatial perspective.

In the literature, there are two approaches for physical massive MIMO channel modeling: deterministic and statistical (IMOIZE et al., 2021). The first approach is based on electromagnetism theory and is considered more accurate; however, the computational burden makes the model unworkable in practical terms. Although the statistical channel models result less accurate, they present reduced computational complexity, making expedite their implementation and analysis.

Among the models of statistical M-MIMO channels, there are two kinds of channel models, namely, *correlation-based stochastic models* (CBSM) and *geometry-based stochastic models* (GBSM). The GBSM is categorized in 2D and 3D according to the antenna array used. Such models are usually accurate and flexible for describing different scenarios, because the model can consider the environmental characteristics. In GBSM, such characteristics result in a correlation degree between the antennas signals; however, in CBSM, this correlation degree is only modeled by a correlation factor, making the CBSM model less complex than the GBSM model.

For XL-MIMO, the main idea consists in distribute the antenna elements, for instance, on the wall of buildings, creating antenna arrays with large dimension and number of antenna elements. Therefore, unlike the previous models available in the literature, the channel modeling needs to consider the non-stationarities. As said, the non-stationarities is related to the fact of the antennas array be large and/or the users is near to the antennas array, thus, there is a significant difference in the received signal power between each antenna element. In M-MIMO systems, the non-stationarity also is presented, however, this characteristic in XL-MIMO is essential, because its effect is more expressive.

The study in channel models is important to understand how parameters influence the model and to compare them to find models that can describe the propagation of signals more accurately. From this study, we can analyze the performance of combining schemes, considering a channel model more realistic. The linear combiners are good candidates to apply in M-MIMO systems due to its performance near to nonlinear precoding and the low complexity. Among the combining schemes, we can cite the conjugate beamforming (CB) and the zero forcing (ZF). Recently, was proposed a lower complexity algorithm to performs the ZF and the regularized ZF (RZF) combining called randomized Kaczmarz (rKA) (BOROUJERDI et al., 2018), where complementary analyzes were developed in (RODRIGUES et al., 2019; ROSA et al., 2019). The rKA presents a lower complexity and, mainly, the algorithm was presented as a robust model to the imperfect knowledge of the channel. In pratical terms, the perfect channel estimation is not realizable, because the number of pilot sequence is limited, resulting in a phenomenon called pilot contamination.

Although pilot contamination is a limiting factor to the performance of the system (MARZETTA, 2010), in (BJÖRNSON et al., 2018) it was presented that in a massive MIMO system it is possible to achieve unlimited spectral efficiency by mitigating the

pilot contamination. The analysis consists of employing a MMSE combining scheme to a multicell scenario, considering a MMSE estimator. This combiner estimates the channel from users of the own cell and the neighboring cells such that is generated a combining vector for each user, where the combiner can eliminate the channel of users that shares the same pilot sequence, resulting a significative gain, mainly, when there are users near to the cell edge. Thus, from this perspective, this work aims to investigate different channel models for M-MIMO and XL-MIMO systems and to describe the MMSE combining for a XL-MIMO system in order to mitigate the pilot contamination. However, this scenario presents some conceptual differences as the environment of implementation, without a multicellular scenario which is considered for analysis of the system.

The 5G network was designed employing several network improvements, such as improvements in spectral performance and energy efficiency, high reliability and low latency. All of these requirements are widely studied by the research community, with the M-MIMO system being developed and more recently, the XL-MIMO system in which both have the ability to substantially increase the data transfer rate. As these are recent proposals, some problems are open, such as channel models and signal processing techniques.

Thus, due to the high relevance in this study, we decided to address in this dissertation two classes of channel models that can be used in both systems. Regarding signal processing, we chose two recent techniques in comparison to traditional techniques for comparison in XL-MIMO systems.

1.1.1 Scenarios and Fading

In a wireless communication system, an electromagnetic wave travels from a transmitter to a receiver through space. The propagation environment is formed by many obstacles, therefore, the signal suffers the effects of reflection, scattering and diffraction, resulting in several different paths for the same signal (KIM, 2015; CHIUEH et al., 2012). These variations of the received signal are classified into two levels: slow or long-term variations and fast or short-term variations (FONTAN; ESPIEIRA, 2008). The first term is composed by a deterministic effect on the signal variations and is due to the distance between the BS and the UE, and a second part caused by a random variable describing the shadowing. The latter effect is a consequence of variations due to multipath and presents a random behavior.

Considering the shadowing and the distance that the user moves away from the transmitter, the power of the two combined effects is calculated as:

$$\mathcal{L}[\text{dB}] = \mathcal{L}_0 - 10\alpha \log_{10} \left[\frac{d}{d_0} \right] + \chi \quad (1.1)$$

where \mathcal{L}_0 is the channel average gain at the reference distance of $d_0 = 1\text{m}$, α is the path loss exponent and determines how fast the signal power decays with the distance, d is the

distance between the transmitter and the receiver and $\chi \sim \mathcal{N}(0, \sigma_{shad}^2)$ are the random fluctuations of the shadowing. Rewriting the Equation (1.1) in linear scale:

$$\mathcal{L} = 10^{\frac{\epsilon_0}{10}} 10^{-\alpha \log_{10}(d)} 10^{\frac{\chi}{10}} \quad (1.2)$$

$$\mathcal{L} = 10^{\frac{\epsilon_0}{10}} d^{-\alpha} 10^{\frac{\chi}{10}} \quad (1.3)$$

Thus, in terms of power received, the such effects attenuate the transmitted power as follows:

$$P_r[W] = P_t \underbrace{L_0 d^{-\alpha}}_{\text{very slow variations}} \underbrace{10^{\frac{\chi}{10}}}_{\text{shadowing}} \quad (1.4)$$

where P_t is the transmit power and L_0 is the channel gain $10^{\frac{\epsilon_0}{10}}$ viewed in Equation (1.3).

The path loss exponent α and the standard deviation of the shadowing σ_{shad} are determined according to each scenario. The path loss exponent has a strong impact in urban environments, especially if the environment contains many buildings. However, in rural settings, the loss is less severe, as show in Table 1.1 (DESIMONE et al., 2015).

Table 1.1 – Path loss exponent for different environments.

Environment	Path Loss Exponent (α)
Free Space	2
Urban area cellular radio	2.7 to 3.5
Shadowed urban cellular radio	3 to 5
In building line-of-site	1.6 to 1.8
Obstructed in building	4 to 6
Obstructed in factories	2 to 3

For the shadowing, the standard deviation also varies for different surroundings, even with a same distance between the BS and the UE (MIAH et al., 2011). The shadowing is resulted of trees (foliage) or discontinuous objects in the signal propagation, where the standard deviation has high values for NLoS (non-line-of-sight) case and in large cells. The variations of the shadowing are presented by the table below (KYÖSTI et al., 2008).

Table 1.2 – Standard deviation of shadow fading.

Environment	Standard Deviation of Shadowing (σ_{shad})	
	LoS [dB]	NLoS [dB]
Urban macrocell	4 - 6	8
Suburban macrocell	4 - 6	8
Urban microcell	3	4
Outdoor to indoor	-	10
Open Rural Macrocell	4 - 6	8

The effects mentioned above have slow variations in the transmitted signal. However, we have also the fast variations on the signal due to multiple reflections and diffraction of solid objects. This variations are more common in urban environments in which the signal travel in different paths resulting in several copies of the original signal. Each copy of the signal arrives in the receiver with different amplitudes and phases, where the sum of the resulting signal can be affected constructively or destructively.

Moreover, the channel is categorized between line-of-sight (LoS) and non-line-of-sight (NLoS). The first refers to the channel when the transmitter and the receiver have a direct line without obstructions, and the second term refers to the channel when the transmitter does not have a direct line of propagation to receiver. To exemplify a signal propagation, Figure 1.1 shows a case where the user is in a urban environment, where we have some scatterers as the car, the buildings and the trees.

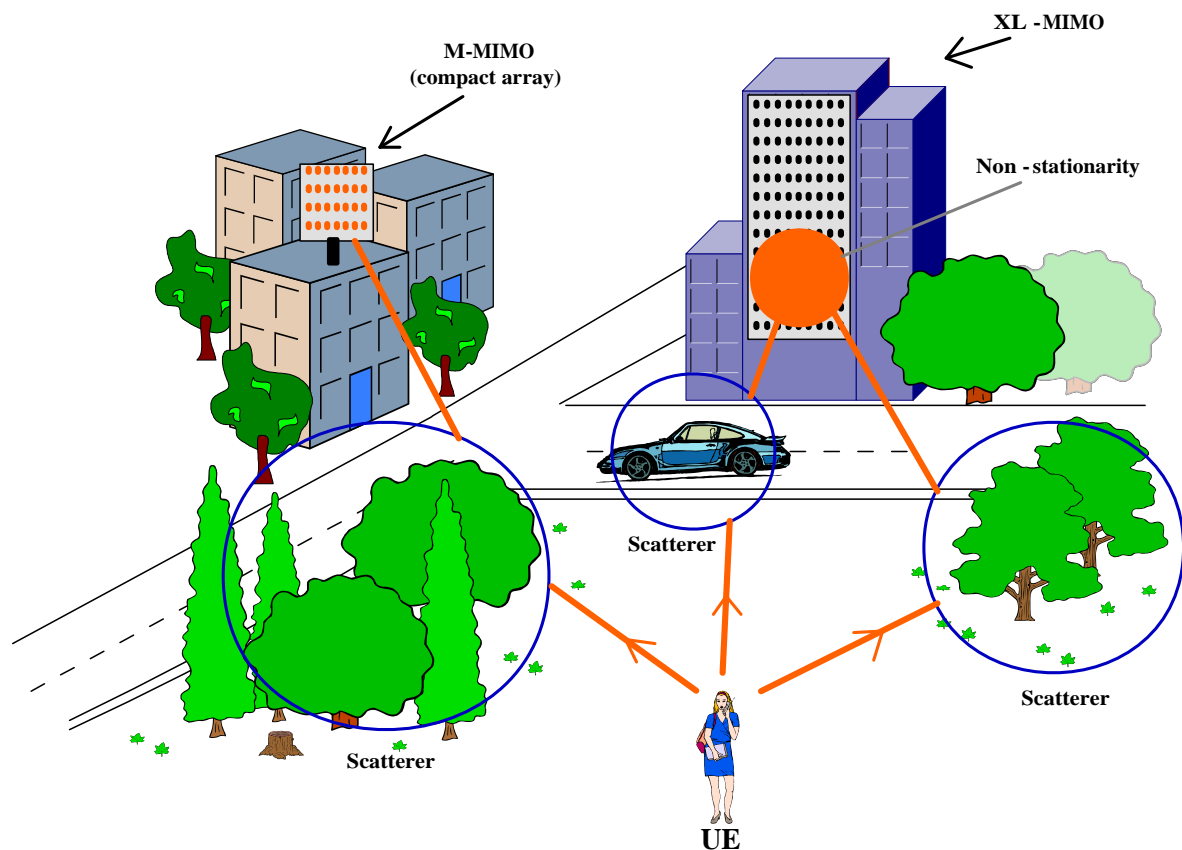
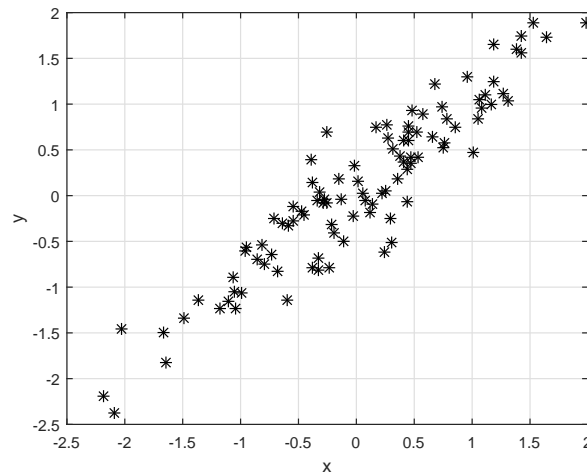


Figure 1.1 – Signal Propagation in an urban environment, where the UE is surrounded by compact and large antennas arrays.

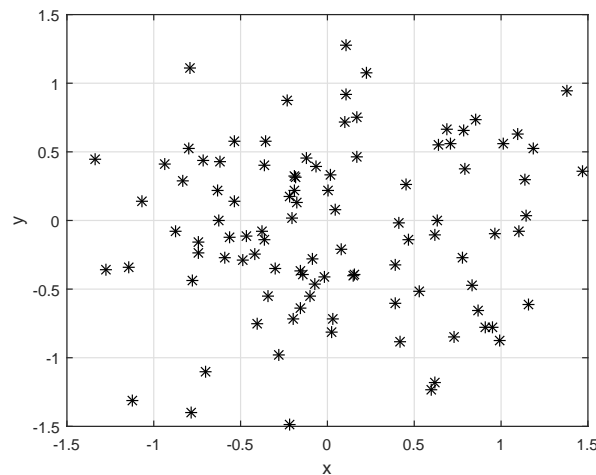
1.1.2 Correlation

Correlation refers to a measure of similarity between variables. The value or degree of similarity between such signals is expressed by a correlation factor defined between -1 and 1. If the correlation factor is positive and very close to 1, we have that the variables have strong correlation so that the variables are proportional as shown in Figure 1.2a. In

the opposite case, where the correlation factor is negative and very close to -1, we have that the variables are strongly correlated, but as one variable grows, the other decreases. Finally, a value close to 0 indicates that the variables are uncorrelated, as shown in Figure 1.2b. In wireless communication, correlation is present in received signals referring to a user or signals from different users.



(a)



(b)

Figure 1.2 – Cross-correlation. (a) Correlated Signals. (b) Uncorrelated Signals.

In the previous section, we comment about the multiple copies of the transmitted signal. When such copies arrive in the receiver antenna, the signals can be correlated mainly if the paths of these copies are similar. In general, the received signals are correlated and its normalized correlation factor can be calculated by:

$$r_{x,y} = \frac{\mathbb{E}\{(x - \mathbb{E}\{x\})(y - \mathbb{E}\{y\})^*\}}{\sqrt{\mathbb{E}\{(x - \mathbb{E}\{x\})^2\}\mathbb{E}\{(y - \mathbb{E}\{y\})^2\}}} \quad (1.5)$$

where x and y represent random variables of a process. In addition to the correlation being represented in the aspect of the propagation environment, one can also verify the

degree of similarity between the signals from different antennas. This happens according to antenna spacing and the array geometry. An example is illustrated in Figure 1.4, where the antennas are arranged side by side. In this example, we can see that if the distance $d_{1,2}$ is small, the antennas 1 and 2 will receive very similar signals, that is, high correlation degree. However, if the spacing is very large, it implies an increase in the size of the antenna array and in the presence of grating lobes, which means that the array has equally strong signal radiation in other directions than desired.

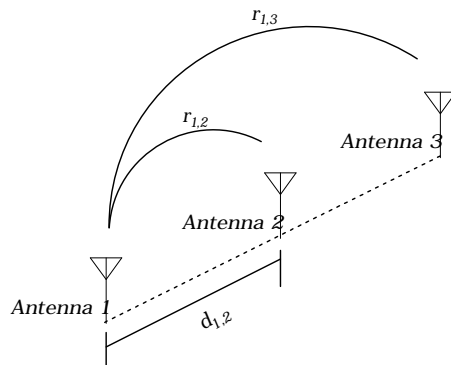


Figure 1.3 – Antenna array sketch indicating the correlation between antennas.

There are tractable methods for calculating antenna correlation according to the spacing between the antennas. However, a common correlation model in the literature is the zeroth order Bessel function of the first kind. The model is described below without considering effects as mutual coupling and fixing a uniform Power Azimuth Spectrum.

$$r(d_H) = J_0\left(\frac{2\pi d_H}{\lambda}\right) \quad (1.6)$$

where λ is the wavelength calculated by the ratio between speed of light and carrier frequency. In this case, we can see below the variations of correlation according to the distance between two antennas. If we analyze the envelope, the correlation factor decreases exponentially when d_H increases.

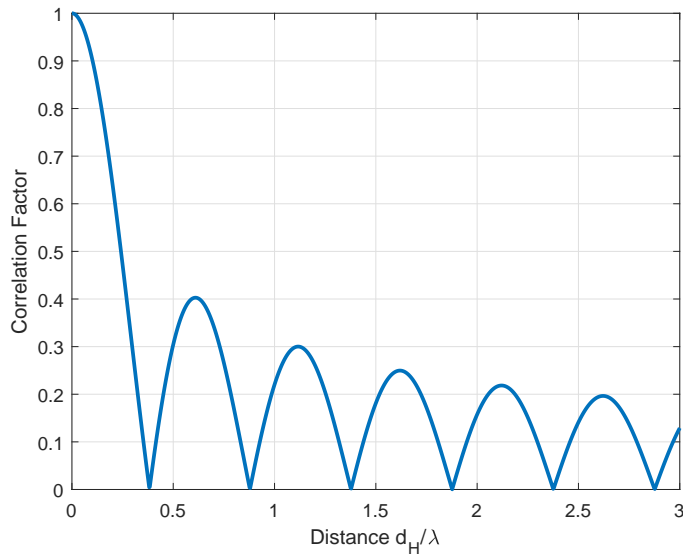


Figure 1.4 – Antenna array arrangement identifying the correlation between antennas.

Next, we will see some channel models that define the correlation factor explicitly and implicitly from the aspect of signal propagation and antennas.

1.1.3 Statistical Channel Models

Two stochastic modelling approaches known as Geometry-Based Stochastic Models (GBSMs) and Correlation-Based Stochastic Models (CBSMs) have been widely used to simulate wireless channels (WU et al., 2015). A GBSM is derived from the knowledge of the scatterers, that is, as electromagnetic waves propagate in the environment. Another type of stochastic modelling is the CBSM, which are models more simple and the correlation properties are modeled explicitly (WANG et al., 2007).

A channel model is developed for different purposes, based on which we can classify them into two types: system simulation models and calibration models (WANG et al., 2010). System simulation models try to represent the real-world channels as realistically as possible, because these models are used for accurate performance assessments of different algorithms and systems. Calibration channel models, on the other hand, are simplified channel models developed for conformance testing of different products and technologies. In general, GBSMs tend to be better system simulation models, such that the model is accurate at the cost of higher computational complexity, while CBSMs tend to be better calibration models, which such models present less implementation complexity, however, the CBSM accuracy is generally compromised (ZHENG et al., 2014).

1.1.3.1 Correlation-based Stochastic Models (CBSM)

In certain situations, a low-complexity and mathematically tractable massive MIMO channel model is preferred when analyzing and simulating system performance (WANG

et al., 2016). Thus, many researches work with channel models based in correlation as in (LIM et al., 2017; ALBDRAN et al., 2016) due to the CBSMs being relatively simple and computationally efficient. They also explicitly address the correlation properties of channel matrices, providing a useful reference for system designers. The drawback of CBSMs comes from the oversimplification and consequently an unrealistic representation. The classic i.i.d. Rayleigh fading channel and the correlated models as exponential are examples of CBSM.

1.1.3.2 2D Geometry-based Stochastic Models (GBSM)

The GBSMs are usually accurate and flexible for describing different scenarios, because the model can consider the environment characteristics and the antenna array type. Besides, the spatial temporal correlation properties are not explicitly specified in the model and need to be further derived from other parameters. Thus, they are complex and computationally inefficient if compared to the CBSM.

GBSM can be classified into: 2D and 3D channel models. 2D models classify antenna arrays that control signal propagation on a 2D plane such as the linear array of antennas. Similarly, 3D models are arrays that can control the radiation of signals to any direction in 3D space, such arrays can be spherical, cylindrical and rectangular.

In addition, we can classify GBSMs according to propagation environments as: One-ring model, Two-ring model and Elliptical model. The One-ring model is appropriate for describing environments, in which the base station is elevated and unobstructed, whereas the mobile station is surrounded by a large number of local scatterers, while the two-ring and elliptical model is appropriate for environments, in which both base station and the users are surrounded by local scatterers (PTZOLD, 2012).

In this work, we present the 2D model for One-ring scenarios, where scatterers are evenly spread around the user and also for a scenario called Gaussian Local Scattering, where its model is similar to One-ring, however, the location of the scatterers have gaussian distribution. For the 2D model, we consider that the antennas are linearly arranged as shown in Figure 1.5 also known as Uniform Linear Array (ULA).

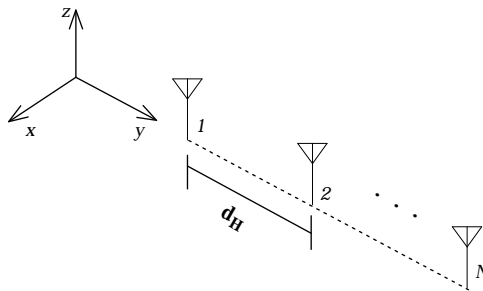


Figure 1.5 – Uniform Linear Array.

1.1.3.3 3D Geometry-based Stochastic Models (GBSM)

The 3D GBSMs are structure as planar, cylindrical and spherical capable of creating beams controlled by two angles, azimuth and elevation (ZHENG et al., 2014). The advantages in control both angles are, per example, in urban or suburban scenarios where one user is on a floor of a building and another user is ground floor, that is, we need to separate the user in elevation angles. In M-MIMO systems, many works consider 2D models, however, the 3D models are better candidates when deploying a large number of antennas in a more compact structure (XIE et al., 2015).

In the Figure 1.6, we present the planar structure known as Uniform Planar Array (UPA), where the structure is analyzed with the One-ring model and the Gaussian Local Scattering model.

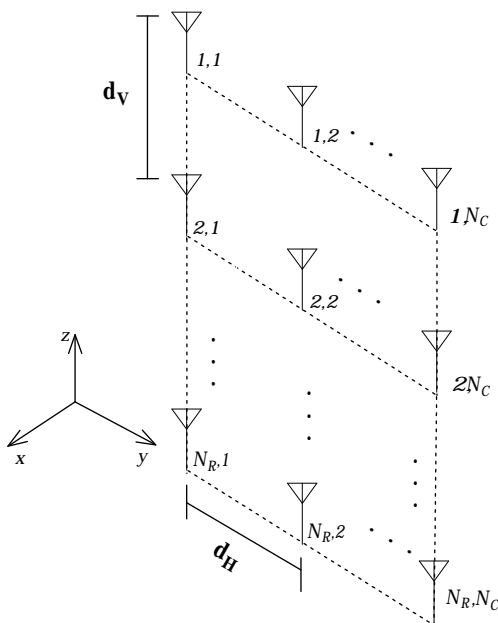


Figure 1.6 – Uniform Planar Array.

1.1.3.4 Extra Large Scale Massive MIMO Channels

Massive MIMO is a system in which the BS is equipped with hundreds of antennas, normally, arranged in a compact structure. However, in XL-MIMO the number of antennas and the array dimension can be considered extremely large, while the users distance to the array is very short compared to the array size (see Fig. 1.1). Thus, two properties are observed in this scenario: spherical wave-front and spatial non-stationary.

The first property indicates that there are angular variations between the signals arriving at each antenna element, *i.e.*, the far-field assumption does not hold. As the antennas array is very large, because the elements of antennas are incorporated in a building of large dimension, the received power from a user is only observed by a antennas set closer to the user. Such antennas set that observe the user is called visibility region (VR)

(CHEN et al., 2017) and result in a significant non-stationarities across antennas elements when the mobile terminals are close to the antenna array, as reported by measurements in (CARVALHO et al., 2019), being necessary consider from a spatial perspective (OESTGES; CLERCKX, 2007).

1.1.4 Figures of Merit

In this section, we revisit relevant performance metrics aiming at comparing and analysing the M-MIMO and XL-MIMO systems.

1.1.4.1 Capacity

The ergodic channel capacity is given by:

$$C = \mathbb{E} \left\{ \log_2 \left[\det \left(\mathbf{I} + \frac{\eta}{M} \mathbf{H} \mathbf{H}^H \right) \right] \right\} \quad (1.7)$$

where η is the average signal-to-noise ratio, M is the number of antennas in BS and \mathbf{H} is the channel matrix.

As the capacity is a concave function (logarithmic function), we can apply the Jensen's inequality to obtain the following upper bound (UB) on the mean (ergodic) capacity (LOYKA, 2001) .

$$C_{\text{ub}} = \log_2 \left[\det \left(\mathbf{I} + \frac{\eta}{M} \mathbb{E}\{\mathbf{R}\} \right) \right] \quad (1.8)$$

where \mathbf{R} is the channel matrix defined by each channel model. Thus, the upper bound on ergodic capacity C_{ub} was analyzed to all channel models, assuming high signal-to-noise ratio.

1.1.4.2 MSE-RKZF Metric

The MSE metric is a measure of perfection in emulating the RZF combiner performance, defined as:

$$\text{MSE} = \frac{1}{MKN} \sum_{n=1}^N \sum_{k=1}^K \sum_{m=1}^M |v_{ml}^{\text{RZF}}(n) - v_{ml}^{\text{rKZF}}(n)|^2 \quad (1.9)$$

where M is the number of antennas at BS, K is the number of users, N is the number of realizations, $v_{ml}^{\text{RZF}}(n)$ is the (ml) th element of the n th realization of the combining matrix calculated by the conventional regularized ZF (RZF) (3.28), and $v_{ml}^{\text{rKZF}}(n)$ is the combiner vector element using rKA algorithm to emulate the RZF combiner.

1.1.4.3 Interference between users

With the aim of analyzing the interference that the UEs cause to each other when considered the single and double-scattering channel model, the variance of the favourable

propagation is measured by:

$$\varsigma_{j,k} = \mathbb{V} \left\{ \frac{\mathbf{h}_{ji}^H \mathbf{h}_{ki}}{\sqrt{\mathbb{E}\{\|\mathbf{h}_{ji}\|^2\} \mathbb{E}\{\|\mathbf{h}_{ki}\|^2\}}} \right\} = \frac{\text{tr}(\mathbf{\Phi}_{ji} \mathbf{\Phi}_{ki})}{\text{tr}(\mathbf{\Phi}_{ji}) \text{tr}(\mathbf{\Phi}_{ki})} \quad (1.10)$$

where \mathbf{h}_{ji} is the channel from the i -th active cluster of the user j . This metric can perform how close the spatial correlation matrices related to the j th and k th users are, in which small values of variance $\varsigma_{j,k}$ results in small interference between the UEs channels, *i.e.*, the channels are closed to the orthogonality.

For this analysis, we evaluate the *interference* using the correlation matrix of each subarray separately. Thus, for single-scattering (SS) model (3.25), the correlation matrix of the i th cluster corresponding to the k th user is $\mathbf{\Phi}_{ki}^{\text{SS}} = \mathbf{R}_i$. For the double-scattering (DS) in eq. (3.20), the channel matrix can be calculated as (NADEEM et al., 2019):

$$\mathbf{\Phi}_{ki}^{\text{DS}} = \text{tr}(\tilde{\mathbf{R}}_{i,k}) \mathbf{R}_i \quad (1.11)$$

1.1.4.4 Spectral Efficiency in XL-MIMO with Linear Combiners

The spectral efficiency (SE) measures the number of bits that can be transmitted across the channel free of errors, over a given channel bandwidth or equivalently per channel use (pcu) (MARZETTA et al., 2016). The sum-SE in the UL of XL-MIMO is defined according to:

$$\text{SE}^{\text{ul}} = \frac{\tau_u}{\tau_c} \sum_{b=1}^B \sum_{l \in \mathcal{K}_b} \sum_{i \in \mathcal{C}_{kb}} \log_2(1 + \gamma_{li(b)}^{\text{ul}}) \quad [\text{pcu}] \quad (1.12)$$

where $\mathcal{K}_b = \{l = 1, \dots, L_s\}$ and $\mathcal{C}_{kb} = \{i = 1, \dots, C_s\}$, with L_s users and C_s clusters active in the b th subarray (SA). The signal-to-interference-plus-noise ratio (SINR) is given by

$$\gamma_{ki(b)}^{\text{ul}} = \frac{|\mathbf{v}_{ki(b)}^H \hat{\mathbf{h}}_{ki(b)}|^2}{\mathbf{v}_{ki(b)}^H \left(\sum_{l \in \mathcal{K}_b} \sum_{i \in \mathcal{C}_{kb}} \hat{\mathbf{h}}_{li(b)} (\hat{\mathbf{h}}_{li(b)})^H - \hat{\mathbf{h}}_{ki(b)} (\hat{\mathbf{h}}_{ki(b)})^H + \mathbf{Z}(b) \right) \mathbf{v}_{ki(b)}} \quad (1.13)$$

where $\hat{\mathbf{h}}_{ki(b)}$ and $\mathbf{v}_{ki(b)}$ is the estimate channel and the combining vector from the i -th cluster of the k -th user corresponding to the b -th subarray, respectively. τ_u is the UL data length, given by:

$$\tau_u = \tau_c - \tau_p - \tau_d \quad (1.14)$$

being τ_p and τ_d the length of the pilot sequence and downlink data, respectively. Notice that τ_c holds for the number of samples per coherence block, *i.e.*, the factor $\frac{\tau_u}{\tau_c}$ in eq. (1.12) refers to the fraction of samples per coherence block that is used for the UL data transmission. Indeed, inside the τ_c time interval occur the transmission of the pilot sequences (for channel estimation purpose), the DL data and UL data.

1.1.4.5 Energy Efficiency (EE)

The EE measures the amount of information that can be reliably transmitted per unit of energy, which is defined as the ratio of the sum-rate to the total power consumption:

$$\text{EE} = \frac{\text{SE}}{\text{ETP} + \text{P}_{\text{CP}}} \quad \left[\frac{\text{pcu}}{\text{W}} \right] \quad (1.15)$$

where ETP is the effective transmit power, calculated as $\text{ETP} = P_{\text{TX}}^{\text{ul}} + P_{\text{TX}}^{\text{tr}}$ and P_{CP} is the circuitry power. The variables $P_{\text{TX}}^{\text{ul}}$ and $P_{\text{TX}}^{\text{tr}}$ represent the power consumed by the RF amplifiers in the UL and UL pilot and data transmissions. It is common to find models that consider the circuit power as a constant term, normally, denominated P_{FIX} . However, this model is not accurate since it does not take accounts, *e.g.*, the digital signal processing and the network load. Thus, as presented in (BJÖRNSON et al., 2015; FILHO et al., 2019), a realistic way to compute the circuit power consumption P_{CP} is given by:

$$\text{P}_{\text{CP}} = \text{P}_{\text{FIX}} + \text{P}_{\text{TC}} + \text{P}_{\text{CE}} + \text{P}_{\text{C/D}} + \text{P}_{\text{BH}} + \text{P}_{\text{LP}} \quad (1.16)$$

where P_{FIX} is a fixed power consumption corresponding, *e.g.*, to the control site-cooling and control signaling. The P_{TC} is the power consumption of the transceiver chains and calculated as:

$$\text{P}_{\text{TC}} = \text{P}_{\text{LO}} + M_b \text{P}_{\text{BS}} + K \text{P}_{\text{UE}} \quad (1.17)$$

where P_{LO} is the power consumed by the local oscillator, P_{BS} is the circuit power of each BS antenna and P_{UE} is the circuit power of each single-antenna UE. P_{CE} is the power consumption for the channel estimation, where the *computational efficiency* at the BS \mathcal{L}_{BS} is considered. The P_{CE} is calculated as:

$$\text{P}_{\text{CE}} = \frac{B_T \mathcal{C}_{\text{CHEST}}}{\tau_c \mathcal{L}_{\text{BS}}} \quad (1.18)$$

where B_T the total bandwidth and $\mathcal{C}_{\text{CHEST}}$ is the number of complex multiplications, divisions, sums and subtractions to compute the channel estimate via (3.16), given by:

$$\mathcal{C}_{\text{CHEST}} = \sum_{b=1}^B C_b (2M_b^2 - M_b) + B (2M_b \tau_u - M_b) \quad (1.19)$$

considering C_b as the number of active clusters and M_b as the number of antennas, both associated with the subarray b . For the sake of simplicity, the complexity to estimate and compute the terms related to the correlation matrices are dropped. This assumption is reasonable as the channel spatial correlation changes slower with time than the channel small-scale fading term, enabling the reuse of the computed matrices during many channel coherence blocks.

Also, the $\text{P}_{\text{C/D}}$ is the power consumption of the channel coding and decoding, given by:

$$\text{P}_{\text{C/D}} = B_T \text{SE} (\mathcal{P}_{\text{COD}} + \mathcal{P}_{\text{DEC}}) \quad (1.20)$$

where \mathcal{P}_{COD} and \mathcal{P}_{DEC} are the coding and decoding power densities, respectively. P_{BH} is the backhaul consumption power and it is calculated as:

$$P_{\text{BH}} = B_T S E \mathcal{P}_{\text{BT}} \quad (1.21)$$

where \mathcal{P}_{BT} is the backhaul traffic power density. Lastly, the power consumption of the linear processing at the BS P_{LP} that depends on the computational complexity of the combining/precoding.

Finally, the power consumed due to the signal processing is defined as:

$$P_{\text{LP}} = B_T \left(1 - \frac{\tau_u}{\tau_c} \right) \frac{\mathcal{C}_{\text{RECEP}}}{\mathcal{L}_{\text{BS}}} + \frac{B_T \mathcal{C}_{\text{COMB}}}{\tau_c \mathcal{L}_{\text{BS}}} \quad (1.22)$$

where the first term represents the power consumed by the UL reception of the data signals, and the second one is the power consumed to compute the combining scheme. For the first term, the signal reception complexity of computing the combined signal, estimated by the number of complex operations to compute eq. (3.19), is equal to:

$$\mathcal{C}_{\text{RECEP}} = \sum_{b=1}^B (2M_b C_b \tau_u - C_b \tau_u) \quad (1.23)$$

Furthermore, the $\mathcal{C}_{\text{COMB}}$ complexity depends on each combiner; hence, for the ZF, RKZF and MMSE combiners the complexities is given by $\mathcal{C}_{\text{COMB}}^{(\text{ZF})}$, $\mathcal{C}_{\text{COMB}}^{(\text{RKZF})}$, and $\mathcal{C}_{\text{COMB}}^{(\text{MMSE})}$, respectively. The number of complex operations to compute the ZF combining matrix is defined as:

$$\mathcal{C}_{\text{COMB}}^{(\text{ZF})} = \sum_{b=1}^B \left(\frac{7}{3} C_b^3 + 3M_b C_b^2 - \frac{1}{2} C_b^2 - \frac{1}{2} C_b \right), \quad (1.24)$$

while, the complexity for the RKZF is computed by

$$\mathcal{C}_{\text{COMB}}^{(\text{RKZF})} = \sum_{b=1}^B \left[C_b T_{rKA} (4M_b + 4) + 2C_b^2 + 4M_b C_b - 3C_b \right] \quad (1.25)$$

Similarly to (RODRIGUES et al., 2019), we estimate the number of complex operations of the RKZF combiner by computing the most complex steps, indicated in the lines 12, 13 and 18 of Algorithm 3. Lastly, the complexity to compute the MMSE combining matrix is equal to

$$\mathcal{C}_{\text{COMB}}^{(\text{MMSE})} = \sum_{b=1}^B \left(\frac{7}{3} M_b^3 + 3M_b^2 C_b - \frac{1}{2} M_b^2 - \frac{1}{2} M_b \right) \quad (1.26)$$

1.2 Goals

1.2.1 General Goals

The objective of this dissertation is to investigate M-MIMO and XL-MIMO systems regarding channel models and combination schemes.

1.2.2 Specific Goals

- Conduct an extensive study of the recent advances in the literature in M-MIMO and XL-MIMO systems;
- Within this study, focus on the main signal processing techniques and on the channel models used for both systems;
- Present a comprehensive analysis of the channel models, incorporating comparisons between models based on correlation and geometry, as well as proposing a channel model for XL-MIMO;
- Perform analysis and comparisons of the combinator scheme in order to confirm theoretical concepts and obtain intuitions for application in XL-MIMO.

1.3 Organization of the text

The first part of the Dissertation analyses the the channel modeling for massive and extra-large (XL) MIMO systems. In this first part, two topics are developed: channel modeling and combining schemes. Both topics are discussed aiming to develop a new scenario in massive MIMO, the XL-MIMO system, where the choice of the combining scheme and the channel modeling are new, been not explored yet in the literature. Hence it provides some insights for coming massive and XL-MIMO system implementation.

Thus, a detailed study on massive and XL-MIMO channel models was developed, comparing both the CBSM and GBSM models, respectively. Such models are presented in Chapter 2, while in Appendix A the associated scientific paper is presented as published in the ETT-Wiley journal.

Next, in the second part of the Dissertation, different combining schemes under extra-large number of antennas configurations are analyzed in order to mitigate the channel effects, while demonstrate effectiveness and feasibility for implementation purpose. Among the analyzed combining schemes, we have explored the randomized Kaczmarz algorithm (rKA), and the M-MMSE for massive MIMO system in Chapter 3. In Appendix B, we show the summary of the submitted paper related to this study.

1.3.1 Contributions

- L. M. Taniguchi, T. Abrão. **Stochastic channel models for massive and extreme large multiple-input multiple-output systems**. Transactions on Emerging Telecommunications Technologies (IF=1.594, A2-Eng. IV in QUALIS-CAPES). Volume 31, Issue 9. September 2020. pp. e4099. <https://doi.org/10.1002/ett.4099>. Copy of the summary of the published article presented in Appendix A.

- L. M. Taniguchi, J. Souza, D. W. Guerra, T. Abrão. **Resource Efficiency and Pilot Decontamination in XL-MIMO Double-Scattering Correlated Channels.** Full paper submitted to the Transactions on Emerging Telecommunications Technologies (IF=1.594, A2-Eng. IV in QUALIS-CAPES), revised R1 version submitted on May 2021. Copy of the submitted article presented in Appendix B.

2 Channel Models

This chapter introduces the types of channel models. The channel is a fundamental part of wireless transmission, because it is responsible for causing effects on the transmitted signal, so the information received is not the same as the transmitted one. In order to the receiver detect the right information, we need to understand how the environment can affect the signal, being this the theme of the chapter. We know that there are several models that try to represent the channel, therefore, we selected some stochastic channel models and evaluated their performance using the capacity, SINR, singular value decomposition (SVD) and condition number (CN) as merit figures. From channel knowledge, we can then study methods to mitigate their effects using combining schemes described in the next chapter.

2.1 Channel Models for M-MIMO and XL-MIMO

The stochastic channel models are defined in CBSM and GBSM as illustrate in Fig. 2.1. The CBSMs can be categorized into two types known as classic i.i.d. Rayleigh fading channel model and correlated channel models (WANG *et al.*, 2016) that describe the characteristics by correlation matrices. To GBSM, works usually assume the one-ring, two-ring and elliptical-ring scenarios (YU; OTTERSTEN, 2002; BAKHSHI *et al.*, 2008; ARIAS; MANDERSSON, 2002). These models are frequently implemented in scenarios where the BS can employ hundreds of antennas in compact arrays. However, a recent scenario, called XL-MIMO, was proposed to improve the area throughput in wireless networks. In this scenario, the antennas elements are disposed in a large surface, where the number of antenna elements is of order of five hundreds or even thousands (BJÖRNSON *et al.*, 2019) antenna elements. Next, we describe the propagation channel models considered.

2.1.1 CBSM

In certain situations, a low-complexity and mathematically tractable massive MIMO channel model is preferred when analysing and simulating system performance (WANG *et al.*, 2016). Thus, many researches work with channel models based in correlation. The first model is the classical exponential model of correlation matrix described below and, next, we analyzed the uncorrelated and exponential with large-scale fading.

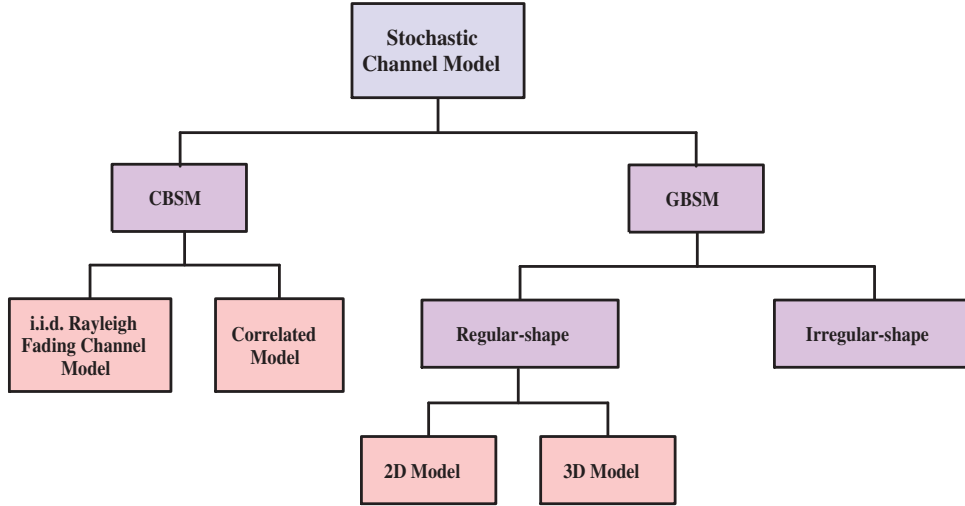


Figure 2.1 – Stochastic Channel Models.

2.1.1.1 Exponential Spatial Correlation

The first model is the classical exponential model (LOYKA, 2001) of a toeplitz correlation matrix described by:

$$[\mathbf{R}]_{m,n} = \begin{cases} \rho^{n-m}, & \text{if } m \leq n \\ \rho_{nm}^*, & \text{otherwise} \end{cases} \quad (2.1)$$

where (m, n) are elements of the matrix that correspond to the antennas elements of the array and ρ is the correlation factor defined between 0 and 1.

2.1.1.2 Uncorrelated Fading with Large-Scale Fading

A consideration of an uncorrelated model is common in the literature where normally the correlation matrix is described by $\mathbf{R} = \beta \mathbf{I}_M$, where β is the path loss term defined as squared amplitude. Adding the effects of the shadowing (BJÖRNSON et al., 2018), the model is described as:

$$\mathbf{R} = \beta \text{diag}(10^{\frac{f_1}{10}}, \dots, 10^{\frac{f_M}{10}}) \quad (2.2)$$

where $f_1, \dots, f_M \sim \mathcal{N}(0, \sigma_{\text{shad}})$ are the random fluctuation of the large-scale fading.

2.1.1.3 Exponential Spatial Correlation with Large-Scale Fading

A model presented by (BJÖRNSON et al., 2018) and based in (LOYKA, 2001) is exponential spatial correlation with the presence of shadowing effects.

$$[\mathbf{R}]_{m,n} = \beta \cdot \rho^{|n-m|} \cdot e^{i(n-m)\theta} \cdot 10^{\frac{f_m+f_n}{20}} \quad (2.3)$$

where θ is the Angle-of-Arrive (AoA). This latter model is more complete as it encompasses more features than the first two.

2.1.2 2D GBSM

GBSM can be classified according to the distribution of the scatterers combined with the number of dimensions of the antenna elements placement. When the propagation environment is analyzed, the GBSM can be classified in *regular-shape* (RS-GBSM) and *irregular-shape* (IR-GBSM) geometry-based stochastic models. In this case, the scatterers can be distributed on regular shapes (for example one-ring, two-ring and ellipse) or irregularly (randomly distributed) (YIN; CHENG, 2016).

The One-ring channel model is appropriate for describing environments, in which the base station is elevated and unobstructed, whereas the user equipment (UE) is surrounded by a large number of local scatterers, while the two-ring and elliptical model is appropriate for environments in which both base station and the users are surrounded by local scatterers (PTZOLD, 2012). Although these models are well established in the literature, such models do not accurately describe M-MIMO and XL-MIMO configurations and scenarios. Although currently there is no model that describes all the characteristics present in the XL-MIMO environment, methodologies that partially describe such scenario have been elaborated, including the effects of the non-stationary and spherical wave-front characteristics.

In addition, the GBSMs can be classified into 2D and 3D antenna elements arrangements. Such classification is useful since antenna arrays can be classified according to its ability in control the signal propagation on 2D plane (such as the linear array of antennas) or 3D space, such as spherical, cylindrical and cubic arrays shape. Indeed, 3D-GBSM models combine geometry-based stochastic channel models with input-output arrays that can control the radiation of signals to any direction in 3D space; such arrays can be spherical, cylindrical and cubic. In practical systems, 3D models are more likely to be more widely used (ZHENG et al., 2014).

In this section, we use the 2D and 3D RS-GBSMs classification, considering the One-ring and Gaussian Local Scattering to define the distribution of the scatterers. In One-ring scenarios, the scatterers are uniformly spread around the user while for a scenario called Gaussian Local Scattering, similar to One-ring, the location of the scatterers present Gaussian distribution. For the 2D model, we consider that the antennas are linearly arranged, also known as ULA, where the array response is given by (BJÖRNSON et al., 2017):

$$\mathbf{a}_n = g_n [1 e^{2\pi i d_H \sin(\bar{\varphi}_n)} \dots e^{2\pi i d_H (M-1) \sin(\bar{\varphi}_n)}]^T \quad (2.4)$$

where $g_n \in \mathbb{C}^M$ is the average gain of the n-th multipath component, the $\bar{\varphi}$ is the angle of an arbitrary multipath component and d_H is the antenna spacing in wavelength of the array. Thus, the channel response \mathbf{h} is the superposition of the array responses of the N_{path} components as show:

$$\mathbf{h} = \sum_{n=1}^{N_{path}} \mathbf{a}_n \quad (2.5)$$

Hence, we have the correlation matrix of the channel presented in eq. (2.5) as:

$$\mathbf{R} = \mathbb{E} \left\{ \sum_{n=1}^{N_{\text{path}}} \mathbf{a}_n \mathbf{a}_n^H \right\} \quad (2.6)$$

where we can rewrite the equation above for the (m,n)th element of \mathbf{R} as:

$$[\mathbf{R}]_{m,n} = \sum_{n=1}^{N_{\text{path}}} \mathbb{E}\{|g_n|^2\} \mathbb{E}\{e^{2\pi i d_H(m-1)\sin(\bar{\varphi}_n)} e^{-2\pi i d_H(n-1)\sin(\bar{\varphi}_n)}\} \quad (2.7)$$

Considering the total average gain of the multipath components $\mathbb{E}\{|g_n|^2\}$ as β and applying the expectation operator, we have:

$$[\mathbf{R}]_{m,n} = \beta \int_{-\infty}^{\infty} e^{2\pi i d_H(m-n)\sin(\bar{\varphi})} f(\bar{\varphi}) d\bar{\varphi} \quad (2.8)$$

where $f(\bar{\varphi})$ is the PDF of $\bar{\varphi}$.

The model in eq. (2.8) is a generic model to GBSM which $f(\bar{\varphi})$ can assume uniform, gaussian and laplace distribution. Illustratively, we describe geometrics models as in Fig. 2.2, where multiple signals arrives in all antennas. In the figure, φ_1 is the nominal angle and δ_1 is the angular standard deviation derivated of mutipath signals, being both originated from the scatterer S_1 .

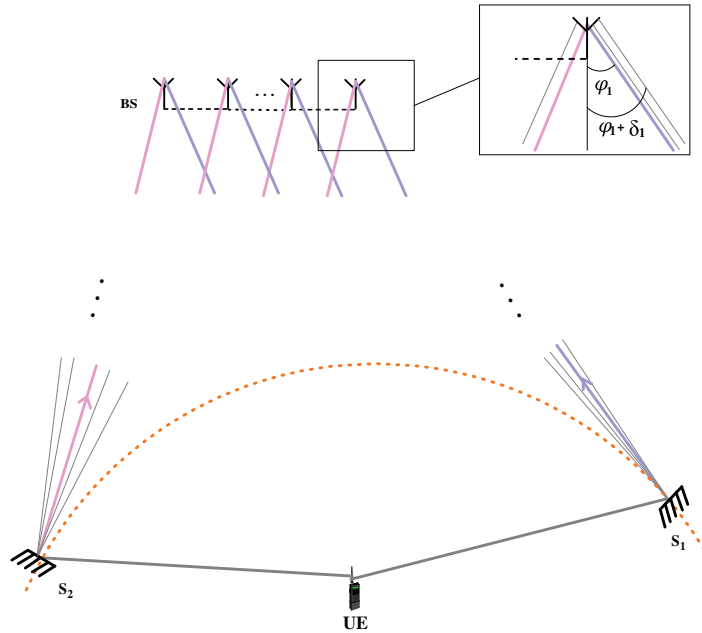


Figure 2.2 – Geometry-based Stochastic Model in Uplink mode where the BS is equipped with linear array. The BS and user are far, thus, the wave-front can be approximated to a plane.

2.1.2.1 One-ring Model

If we consider $f(\bar{\varphi})$ as a uniform distribution, we have the one-ring model which will be presented below. The one-ring model is defined as a local scattering, around to UE,

distributed uniformly as $f(\bar{\varphi}) \sim \mathcal{U}(\varphi - \Delta, \varphi + \Delta)$. Thus, the correlation matrix will result in:

$$[\mathbf{R}]_{m,n} = \frac{\beta}{2\Delta} \int_{\varphi-\Delta}^{\varphi+\Delta} e^{2\pi i d_H(m-n)\sin(\bar{\varphi})} d\bar{\varphi} \quad (2.9)$$

Considering that $\bar{\varphi} = \varphi + \delta$ the equation can be rewritten as:

$$[\mathbf{R}]_{m,n} = \frac{\beta}{2\Delta} \int_{-\Delta}^{\Delta} e^{2\pi i d_H(m-n)\sin(\varphi+\delta)} d\delta \quad (2.10)$$

where φ is the nominal angle of arrival (AoA) and δ is the variation around to nominal angle, Δ is the range in which the multi components are disposed. Such variables, AoA and Δ , represent the degree of channel correlation. Thus, the correlation between the signals can be modeled by the angular interval at which the signals arrive while the degree of correlation between the antennas can be modeled from AoA.

2.1.2.2 Gaussian Local Scattering Model

Another channel model based in geometry is the Gaussian local scattering model described in (BJÖRNSON et al., 2017), where the correlation matrix is described by:

$$[\mathbf{R}]_{m,n} = \beta \int_{-\infty}^{\infty} e^{2\pi i d_H(m-n)\sin(\bar{\varphi})} \frac{1}{\sqrt{2\pi\sigma_{\bar{\varphi}}}} e^{-\frac{(\bar{\varphi}-\varphi)^2}{2\sigma_{\bar{\varphi}}^2}} d\bar{\varphi} \quad (2.11)$$

Taking the same consideration as the one-ring model, $\bar{\varphi} = \varphi + \delta$, the eq. in (2.11) can be rewritten as:

$$[\mathbf{R}]_{m,n} = \beta \int_{-\infty}^{\infty} e^{2\pi i d_H(m-n)\sin(\varphi+\delta)} \frac{1}{\sqrt{2\pi\sigma_{\varphi}}} e^{-\frac{\delta^2}{2\sigma_{\varphi}^2}} d\delta \quad (2.12)$$

where σ_{φ} is the angular standard deviation (ASD) of the multiple signal components around the nominal angle. An approximation can be done if σ_{φ} has small values, below 15° resulting in a close-form expression:

$$[\mathbf{R}]_{m,n} = \beta e^{2\pi i d_H(m-n)\sin(\varphi)} e^{-\frac{\sigma_{\varphi}^2}{2}(2\pi d_H(m-n)\cos(\varphi))^2} \quad (2.13)$$

Some channel measurements showed the presence of shadowing (GAO et al., 2015) and in (SANGUINETTI et al., 2020) the correlation matrix for the gaussian model was presented as:

$$[\mathbf{R}]_{m,n} = \beta 10^{\frac{f_m+f_n}{10}} \frac{1}{S} \sum_{s=1}^S e^{2\pi i d_H(m-n)\sin(\varphi_s)} e^{-\frac{\sigma_{\varphi}^2}{2}(2\pi d_H(m-n)\cos(\varphi_s))^2} \quad (2.14)$$

where S is the number of scatterers and φ_s is the nominal angle of arrival of the s-th scatterer.

2.1.3 3D GBSM

The 3D GBSMs are structure as planar, cylindrical and spherical capable of creating beams controlled by two angles, azimuth and elevation (ZHENG et al., 2014). Most of the channel model described for the MIMO system considers 2D models, however, for applications on M-MIMO systems, the 3D models are better candidates due to the large number of antennas that M-MIMO proposes (XIE et al., 2015). Based on (BJÖRNSON et al., 2017), a planar structure, known as Uniform Planar Array (UPA), will be analyzed with the One-ring model and the Gaussian Local Scattering model.

When we consider that the user is far enough from the antennas array, the plane wave can be evaluated as:

$$\mathbf{k}(\bar{\varphi}, \bar{\theta}) = \frac{2\pi}{\lambda} \begin{bmatrix} \cos(\bar{\theta}) \cos(\bar{\varphi}) \\ \cos(\bar{\theta}) \sin(\bar{\varphi}) \\ \sin(\bar{\theta}) \end{bmatrix} \quad (2.15)$$

where $\bar{\varphi}$ and $\bar{\theta}$ are the azimuth and elevation angles of each received signal. The location of the m -th antenna on the x , y , and z axis for the planar array can be described as:

$$\mathbf{u}_m = \begin{bmatrix} 0 \\ p_y(m)d_H\lambda \\ p_z(m)d_V\lambda \end{bmatrix} \quad (2.16)$$

where $p_y(m) = \text{mod}(m-1, M_H)$ and $p_z(m) = \lfloor (m-1)/M_H \rfloor$ are the horizontal and vertical index of antenna m , respectively. Thus, we can write the correlation matrix as:

$$[\mathbf{R}]_{m,n} = \beta \int \int e^{j2\pi d_V [p_z(m)-p_z(n)] \sin(\bar{\theta})} e^{j2\pi d_H [p_y(m)-p_y(n)] \cos(\bar{\theta}) \sin(\bar{\varphi})} f(\bar{\varphi}, \bar{\theta}) d\bar{\varphi} d\bar{\theta} \quad (2.17)$$

2.1.3.1 One-ring Model

From eq. (2.17), if we consider that elevation and azimuth angles with uniform distribution, we have a 3D one-ring. Thus, the one-ring model for a UPA is described as:

$$[\mathbf{R}]_{m,n} = \frac{\beta}{4\Delta_\varphi\Delta_\theta} \int_{\theta-\Delta_\theta}^{\theta+\Delta_\theta} \int_{\varphi-\Delta_\varphi}^{\varphi+\Delta_\varphi} e^{i2\pi d_V [p_z(m)-p_z(n)] \sin(\bar{\theta})} e^{i2\pi d_H [p_y(m)-p_y(n)] \cos(\bar{\theta}) \sin(\bar{\varphi})} d\bar{\varphi} d\bar{\theta} \quad (2.18)$$

where $\bar{\theta} \in [-\pi/2, \pi/2)$ and $\bar{\varphi} \in [-\pi, \pi)$, Δ_θ and Δ_φ are the angular spread in elevation and azimuth domain, $p_z(m)$ and $p_y(m)$ refers to the index of the m -th antenna on the z and y axis, respectively, in the same sense, $p_z(n)$ and $p_y(n)$ refers to the index of the n -th antenna on the z and y axis. The horizontal and vertical distances are defined by d_H and d_V with the antenna element placed by x (row index) and y (column index) and β describes the macroscopic large-scale fading.

Considering $\bar{\varphi} = \varphi + \delta_\varphi$ and $\bar{\theta} = \theta + \delta_\theta$, the eq. (2.18) is rewritten as:

$$[\mathbf{R}]_{m,n} = \frac{\beta}{4\Delta_\varphi\Delta_\theta} \int_{-\Delta_\theta}^{\Delta_\theta} \int_{-\Delta_\varphi}^{\Delta_\varphi} e^{i2\pi d_V [p_z(m)-p_z(n)] \sin(\theta+\delta_\theta)} e^{i2\pi d_H [p_y(m)-p_y(n)] \cos(\theta+\delta_\theta) \sin(\varphi+\delta_\varphi)} d\delta_\varphi d\delta_\theta \quad (2.19)$$

As with 2D models, for 3D models, both azimuth and elevation angles play a fundamental role in channel modeling, incorporating information that defines the degree of correlation of the antennas. In addition, correlation can also be modeled by the angular interval, Δ_φ and Δ_θ , in which it defines the correlation between the signals.

2.1.3.2 Gaussian Local Scattering Model

From eq. (2.17), we will analyze the scattering with Gaussian distribution shown as:

$$[\mathbf{R}]_{m,n} = \frac{\beta}{2\pi\sigma_\varphi\sigma_\theta} \int_{-\infty}^{\infty} \int_{-\infty}^{\infty} e^{i2\pi d_V [p_z(m)-p_z(n)] \sin(\theta)} e^{i2\pi d_H [p_y(m)-p_y(n)] \cos(\theta) \sin(\varphi)} e^{\frac{1}{2\sigma_\varphi^2} (\bar{\varphi}-\varphi)^2} e^{\frac{1}{2\sigma_\theta^2} (\bar{\theta}-\theta)^2} d\bar{\varphi} d\bar{\theta} \quad (2.20)$$

where σ_φ and σ_θ describe the angular standard deviation of the azimuth and elevation angles. Considering $\bar{\varphi} = \varphi + \delta_\varphi$ and $\bar{\theta} = \theta + \delta_\theta$, the eq. (2.20) is rewritten as:

$$[\mathbf{R}]_{m,n} = \frac{\beta}{2\pi\sigma_\varphi\sigma_\theta} \int_{-\infty}^{\infty} \int_{-\infty}^{\infty} e^{i2\pi d_V [p_z(m)-p_z(n)] \sin(\theta)} e^{i2\pi d_H [p_y(m)-p_y(n)] \cos(\theta) \sin(\varphi)} e^{\frac{\delta_\varphi^2}{2\sigma_\varphi^2} + \frac{\delta_\theta^2}{2\sigma_\theta^2}} d\delta_\varphi d\delta_\theta \quad (2.21)$$

2.1.4 Extreme Large Massive MIMO Channels

Massive MIMO is a system in which the BS is equipped with hundreds of antennas. The large number of antennas impacts in some unique characteristics, such as spherical wave-front assumption and spatial non-stationarity. In MIMO system, the assumption of the plane wave-front is reasonable since the size of antennas array is smaller, *i.e.*, the power variations between the antennas can be assumed approximately a constant. However, in XL-MIMO the number of antennas and the array dimension can be considered extreme large, while the users distance to the array is very short compared to the array size. Thus, the far-field assumption does not hold, being necessary the spherical wave-front assumption. The far-field is often taken to exist for distances greater than the Rayleigh distance, given as:

$$Z = \frac{2D^2}{\lambda} \quad (2.22)$$

where D is the maximum dimension of the antenna or antenna array, and λ represents the wavelength.

The non-stationary properties associated to the channel clusters can be observed on large antenna arrays due to the possibility of different antenna elements observe different sets of clusters (CHEN et al., 2017), where the set of antenna elements observed is called visibility region (VR). In massive MIMO configurations, it is observed significant non-stationarities across antennas elements when the mobile terminals are close to the antenna array, as reported by measurements in (CARVALHO et al., 2020), being necessary consider from a spatial perspective (OESTGES; CLERCKX, 2007). The XL-MIMO principle consists in incorporating the elements of antennas in a building of large dimension, thus, the non-stationarities and the spherical wave-front features become essential considerations. The physical XL-MIMO channel scenarios with a linear array and C_j channel clusters can be represented as in Fig. 2.3. To build the XL-MIMO channel model, one can follow the steps as determine the number of cluster and the geographical position; generate the VR for each cluster; determine the pathloss for each antenna element; and generate the channel coefficient from each user according to the antenna correlation model.

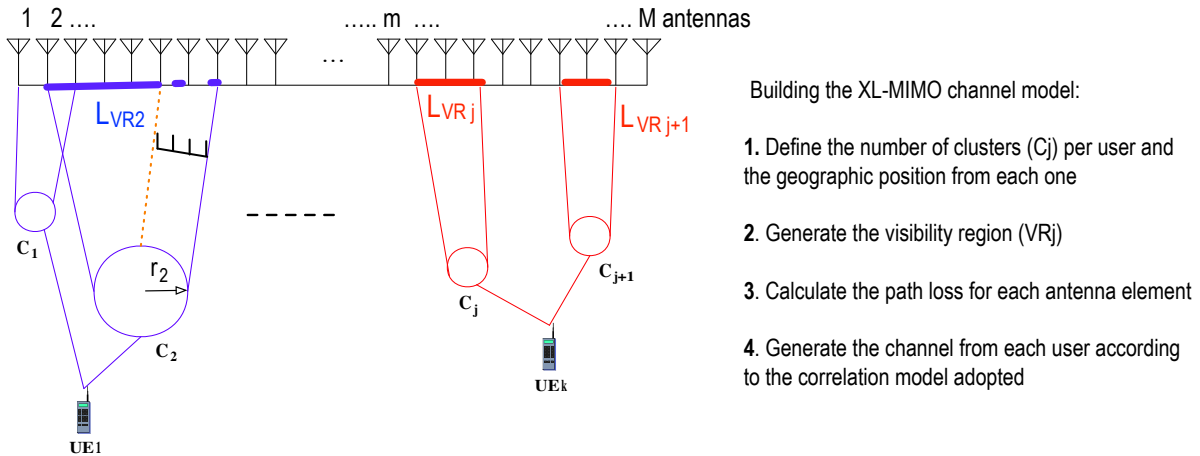


Figure 2.3 – Typical XL-MIMO scenario: each cluster defines the VR length ($L_{VR,j}$) in the antennas array.

From the perspective of clustering position, in this work we analyzed two schemes scenarios, as depicted in Fig. 2.4. In the first configuration, a distance d_1 corresponding to an equal distance between the center of the BS and any cluster positioning in the valid distribution cluster region. Thus, the d_1 and azimuth angle will determine the cluster localization, as well as the received power in each BS antenna array. In the second scheme, the cluster distribution region is parallel to the BS and the distance between the region and the array is determined by d_2 .

In step 2 of Fig. 2.3, we need to define the size of each cluster, because it will determine the VR size. Hence, in Fig. 2.3 one can see that the cluster C_2 is able to see a larger number of antennas compared to cluster C_1 due to the cluster size. In this work, we define the cluster radius r and the VR size region L_{VR} are related by $L_{VR} = 2r$. Moreover, in the VR it is possible the presence of obstacles, reducing the number of antennas that

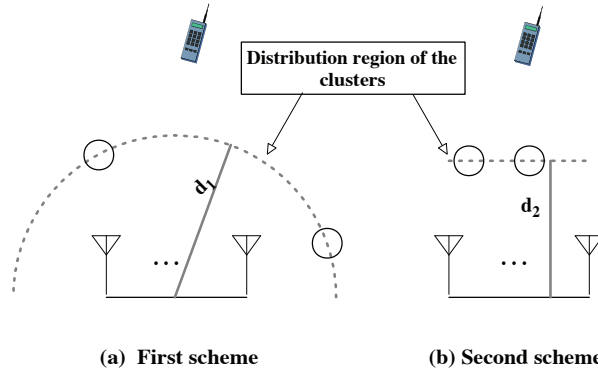


Figure 2.4 – Adopted channel clustering distribution following two representative scenarios.

receive the signal from the corresponding channel cluster. Hence, considering the number of antennas that the cluster can observe, a simple way to simulate the obstacles consists in generate the VR in XL-MIMO scenarios as presented in Algorithm 1, where λ is the carrier wavelength, p_0 is the probability of the antenna not being visible, p_1 is the probability of the antenna being visible, c is a factor which defines how fast the regions changes to visible and not visible (amount of obstacles), and r_{\min} and r_{\max} are the minimum and maximum cluster radius, respectively.

Algorithm 1 Generation of the VR

Input $M, \lambda, r_{\min}, r_{\max}, p_0, p_1, c$

Pick a radius r with uniform probability distribution between r_{\min} and r_{\max}

$$L_{\text{VR}} = 2r$$

$$d_H = 5\lambda$$

$$L_{\text{BS}} = (M - 1)d_H$$

$$M_{\text{VR}} = \left\lceil \frac{ML_{\text{VR}}}{L_{\text{BS}}} \right\rceil$$

$$v_{\text{prob}} = [p_0 \ p_1]$$

Pick a initial number v_{ant} (0 or 1) with equal probability

$$i = 0$$

for $n = 1 : M_{\text{VR}}$ **do**

$$M_{\text{set}}(n) = v_{\text{ant}}$$

if $v_{\text{ant}} = 1$ **then**

$$v_{\text{prob}} = [p_0 \ p_1]$$

$$i = 0$$

else if $v_{\text{ant}} = 0$ and $(p_1 - i) \geq 0$ **then**

$$v_{\text{prob}} = [p_1 - i \ p_0 + i]$$

$$i = i + c$$

else if $v_{\text{ant}} = 0$ and $(p_1 - i) < 0$ **then**

$$v_{\text{prob}} = [0 \ 1]$$

end if

Pick another number v_{ant} (0 or 1) with probability function of v_{prob}

end for

M_{set} : antenna set within VR; antennas may be obstructed [$M_{\text{set}}(n) = 0$] or not obstructed [$M_{\text{set}}(n) = 1$]

Output M_{set}

In step 3, Fig. 2.3, the path loss in dB from the user to each antenna element n is calculated as:

$$\mathcal{L}(n) = \mathcal{L}_0 - 10 \cdot \alpha \cdot \log_{10} \left[\frac{d(n)}{d_0} \right] \quad (2.23)$$

where \mathcal{L}_0 is the channel average gain at the reference distance of $d_0 = 1\text{m}$, α is the path loss exponent, which determines how fast the signal power decays with the distance, $d(n)$, in meters, is the sum of the distance between the c th cluster to the n th antenna element and the distance between the k th UE to the c th cluster.

Finally, in the step 4 the channel from each cluster c corresponding to each user k is generated as:

$$\mathbf{h}_{k,c} = \boldsymbol{\beta}_{k,c} \circ (\mathbf{R}_{k,c}^{\frac{1}{2}} \mathbf{z}_{k,c}) \quad (2.24)$$

where \circ denotes the Hadarmard product, $\boldsymbol{\beta}_{k,c}$ is the vector of path loss amplitude gain, related to user k and cluster c , while $\mathbf{R}_{k,c}$ is the correlation matrix for the cluster c and user k , described like the stationary case, and the short term fading is given by $\mathbf{z}_{k,c} \sim \mathcal{CN}(\mathbf{0}, \mathbf{I}_M)$. Thus, the channel from the UE k is obtained:

$$\mathbf{h}_k = \sum_{c=1}^{C_T} \mathbf{h}_{k,c} \quad (2.25)$$

where C_T is the total number of clusters for the k th mobile user. Hence, the entire channel matrix $\mathbf{H} \in \mathbb{C}^{M \times K}$ is defined simply as $\mathbf{H} = [\mathbf{h}_1 \ \mathbf{h}_2 \ \dots \ \mathbf{h}_k \ \dots \ \mathbf{h}_K]$.

2.1.5 Downlink Transmission in XL-MIMO with Linear Precoding

For the downlink transmission, the BS transmits payload data to its UEs, using a linear precoding. Let s_k be the symbol to be transmitted to the k th user, where $\mathbb{E}\{|s_k|^2\} = 1$. Each user is associated with the precoding vector $\mathbf{w} \in \mathbb{C}^{M \times 1}$, that determines the spatial directivity of the transmission. Thus, the transmitted signal is described by:

$$\mathbf{x} = \mathbf{W}\mathbf{s} \quad (2.26)$$

where $\mathbf{W} = [\mathbf{w}_1 \ \dots \ \mathbf{w}_K]$ and \mathbf{s} is the transmitted signal vector. Aiming at satisfying the power constraints, the precoding must be chosen obeying $\mathbb{E}\{|\mathbf{x}|^2\} = P$. The received signal at the K users is given by:

$$\mathbf{y} = \mathbf{H}^H \mathbf{x} + \mathbf{n} \quad (2.27)$$

where $(\cdot)^H$ is the the Hermitian operator, \mathbf{n} is a vector whose k th element, n_k , is the additive noise at the k th user and $\mathbf{H} \in \mathbb{C}^{M \times K}$ contains the channel vectors of each user. Two selected low-complexity linear precoding techniques are the Conjugate Beamforming (CB) and Zero-forcing (ZF), defined respectively by:

$$\mathbf{W}^{\text{CB}} = \mathbf{H} \quad (2.28)$$

$$\mathbf{W}^{\text{ZF}} = \mathbf{H}(\mathbf{H}^H \mathbf{H})^{-1} \quad (2.29)$$

To satisfy the power constraint of the transmitted signal, the precoding in (2.28) and (2.29) are normalized as:

$$\mathbf{W}^{\text{CB}} = \begin{bmatrix} p_1 \frac{\mathbf{w}_1^{\text{CB}}}{\|\mathbf{w}_1^{\text{CB}}\|} & \dots & p_K \frac{\mathbf{w}_K^{\text{CB}}}{\|\mathbf{w}_K^{\text{CB}}\|} \end{bmatrix} \quad (2.30)$$

$$\mathbf{W}^{\text{ZF}} = \begin{bmatrix} p_1 \frac{\mathbf{w}_1^{\text{ZF}}}{\|\mathbf{w}_1^{\text{ZF}}\|} & \dots & p_K \frac{\mathbf{w}_K^{\text{ZF}}}{\|\mathbf{w}_K^{\text{ZF}}\|} \end{bmatrix} \quad (2.31)$$

where p_1, \dots, p_K are the transmit powers for each user in which the average transmit power at the BS is $P = p_1 + p_2 + \dots + p_K$, $\mathbf{w}_1^{\text{CB}}, \dots, \mathbf{w}_K^{\text{CB}}$ and $\mathbf{w}_1^{\text{ZF}}, \dots, \mathbf{w}_K^{\text{ZF}}$ are the precoding vectors for each user according to the CB and ZF principle, respectively.

2.2 Numerical Results

In this section the validation of the analyzed M-MIMO and XL-MIMO channel models is corroborated numerically. The adopted channel and system parameter values are described in Table 2.1.

2.2.1 CBSM

For CBSMs, the Table 2.2 describes the parameters evaluated in each simulation. Thus, we individually present the values used to generate each figure.

2.2.1.1 Exponential

The first model is the exponential presented in eq. (2.1). The C_{ub} for this model was analyzed by the number of antennas and by the increase of the correlation factor as showed in Fig. 2.5.a and Fig. 2.5.b, respectively. The capacity presents an exponential gain with the logarithmic increase in the number of antennas. For this model, the number of BS antennas M can increase the capacity up to 7 times, if we compare a system with 20 antennas against 400 antennas. However, the correlation factor has an undesirable effect on the capacity, mainly, when $\rho > 0.6$, the capacity decreases drastically. Therefore, it is possible to see that the correlation factor has a strong impact on the system capacity even under a large number of antennas.

2.2.1.2 Uncorrelated Fading

The second model is the uncorrelated fading defined in eq. (2.2). The analysis of capacity versus number of antennas is depicted in Fig. 2.6.a. Besides the same increasing

Table 2.1 – Parameter values adopted in the numerical simulations for M-MIMO and XL-MIMO channels.

Parameters	Values
M-MIMO Channel	
Average signal-to-noise ratio	$\eta = 60$ dB
Figure of merit: Ergodic capacity	C_{ub}
Path loss term	$\beta = 1$
XL-MIMO Channel	
Average signal-to-noise ratio	$\eta = 10$ dB
Figure of merit: SINR	γ_k
Number of antennas M at the BS	100
Number of clusters by UE	2
Distance d_1 for the 1st scheme of clusters distribution	35 m
Distance d_2 for the 2nd scheme of clusters distribution	20 m
Distance between the UE and the BS \tilde{d}	40 m
Path loss exponent for the VR	$\alpha_{\text{VR}} = 3$ dB
Path loss exponent out of the VR	$\alpha_{\text{nVR}} = 6$ dB
Normalization factor	$A = \tilde{d}^{\alpha_{\text{VR}}} = 40^3$
Cluster radius $r \in [r_{\text{min}}; r_{\text{max}}]$	$r \sim \mathcal{U}(5, 10)$ m
Probability of the antenna not visible	$p_0 = 0.05$
Probability of the antenna is visible	$p_1 = 1 - p_0 = 0.95$
Factor c related to the VR	$c = 0.05$
Channel average path loss gain \mathcal{L}_0	-34.53 dB
Pathloss reference distance	$d_0 = 1$ m
MIMO System	
Linear Precoding	CB; ZF
Carrier frequency	$f = 2.4$ [GHz]
Carrier wavelength	$\lambda = 12.5$ [cm]
Total transmit power P	1 W
Transmit power for each user p_k	P/K
Number of Monte Carlo realizations	300

Table 2.2 – Parameter values adopted for CBSMs.

CBSM - Parameters adopted in each simulation						
	Fig. 5a	Fig. 5b	Fig. 6a	Fig. 6b	Fig. 7a	Fig. 7b
Path loss term β	1	1	1	-	1	1
Number of antennas M	[20:400]	100	[20:400]	-	[20:400]	100
Correlation factor ρ	[0:0.2:1]	[0:1]	-	-	[0:0.2:1]	[0:1]
Shadowing - standard deviation σ_φ	-	-	[0:2:6]	[0:10]	4	[0:2:6]
Angle of arrival θ	-	-	-	-	$\pi/2$	$\pi/2$

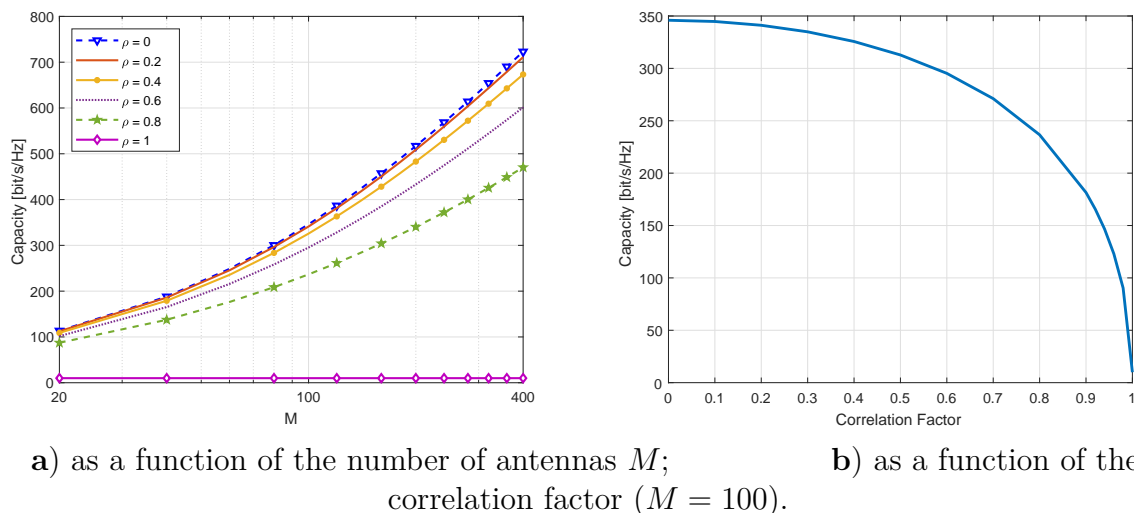


Figure 2.5 – CBSM exponential model. Capacity as a function of a) number of antennas; (b) correlation factor assuming $M = 100$.

capacity behavior with the logarithmic increment on the number of antennas, one can observe the effect of the shadowing. Indeed, when the standard deviation of the shadowing increases, the channel capacity also increases.

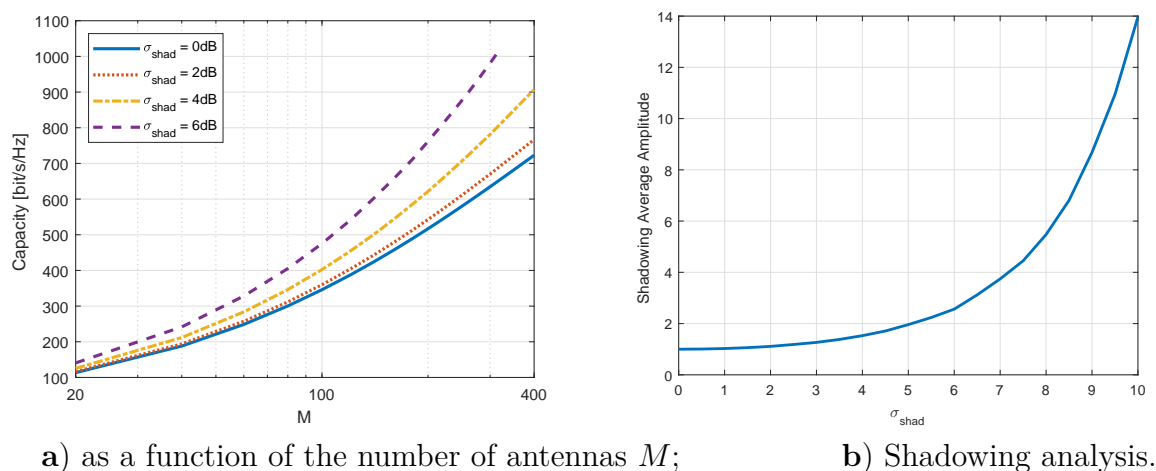


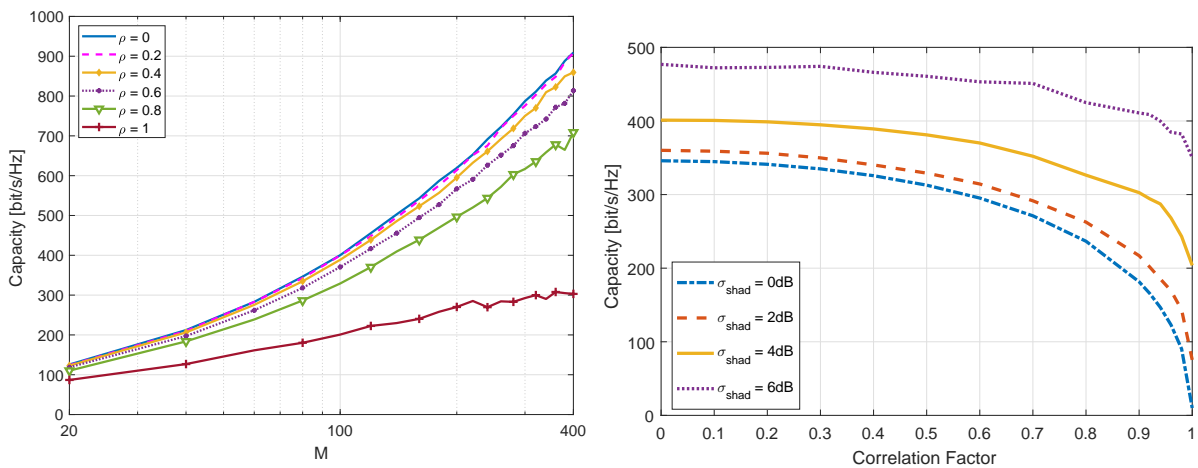
Figure 2.6 – Uncorrelated fading: a) Upper bound of capacity \times number of antennas for different values of standard deviation of shadowing (σ_{shad}); b) Shadowing amplitude when the standard deviation is increased.

In order to measure the gain that the shadowing can offer, in Fig. 2.6.b, the shadowing average amplitude is depicted as a function of its standard deviation. One can see that the shadowing channel term is able to provide an exponential gain in the channel capacity explaining the behavior in the Fig. 2.6. From the shadowing term described in eq. (2.2), one can verify that the term is always positive even when f_m (f_1, \dots, f_M) is negative. If f_m has small variance, on the average, the shadowing term will be small. However, for high variances, f_m may assume more likely larger values and, on average, the shadowing

term will be large. Besides, the shadowing term provides a decorrelation effect between the antenna signals, increasing the channel capacity. The difference in capacity is high if we compare the channel with shadowing variance σ_{shad} of 1 dB against 10 dB, resulting in average amplitude of shadowing of 1 versus 14, respectively.

2.2.1.3 Exponential Model with Large Scale Fading

The last CBSM considered herein is the exponential model combined with shadowing effects, as defined in eq. (2.3). The channel capacity for an increasing number of antennas and a growing correlation factor is depicted in Fig. 2.7.a and 2.7.b, respectively, where the increase rate of capacity with the number of antennas depends on the channel correlation index ρ . However, differently from the simple exponential model, the values of capacity are higher due to presence of the shadowing. Moreover, one can observe that even under a correlation factor near or equal to $\rho = 1$, the channel capacity increases steadily with M , but of course with reduced rate when $\rho \rightarrow 1$. Furthermore, Fig. 2.7.b, shows channel capacity values for correlation values in the range $\rho \in [0; 1]$ and different standard deviation shadowing values. As expected, when the std shadowing values increases, the UB capacity increases too. Besides, notice that the capacity is close to uncorrelated channel capacity values without shadowing when the standard deviation value is 6 dB for a fully correlated channel condition, $\rho = 1$.



a) as a function of the number of antennas M ($\sigma_{\text{shad}} = 4\text{dB}$) **b)** as a function of the correlation degree ($M = 100$).

Figure 2.7 – Correlated-based stochastic channel fading: a) UB capacity when the number of antennas increases; b) UB capacity for different values of std shadowing for $M = 100$ antennas.

2.2.2 GBSM

For GBSMs, the Table 2.3 describes the parameter values adopted in each numerical simulation. Thus, we individually present the values used to generate each figure.

Table 2.3 – Adopted values for GBSMs channel parameters.

Figure	# antennas M	Antenna spacing d_H	AoA (azimuth) φ	AoA Range Δ_φ	AoA Std σ_φ	Shad. Std σ_{shad}	AoA (elevation) θ	AoA Range Δ_θ	AoA Std σ_θ
8b	100	0.5λ	[0;360]	[0;45]	-	-	-	-	-
9a	100	0.5λ	$\pi/6$	[1;50]	-	-	-	-	-
9b	100	0.5λ	$\pi/6$	$\sqrt{3}[10; 20; 30]$	-	-	-	-	-
10a	100	0.5λ	[0;90]	[0;45]	-	-	-	-	-
10b	100	0.5λ	[0;360]	[10;30]	-	-	-	-	-
10c	[20:400]	0.5λ	[0;90]	[10;30]	-	-	-	-	-
10d	100	[0:10] λ	0	[10;30]	-	-	-	-	-
11a	100	0.5λ	$\pi/6$	-	[0:5:15]	0	-	-	-
11b	100	0.5λ	$\pi/6$	-	[0:5:15]	2	-	-	-
12a	100	0.5λ	[0;90]	-	[0:15]	[0:2:4]	-	-	-
12b	100	0.5λ	[0;360]	-	15	[0:2:4]	-	-	-
12c	[20:400]	0.5λ	[0;90]	-	15	[0:2:4]	-	-	-
12d	100	[0:10] λ	0	-	[5;15]	0	-	-	-
13a	100	0.5λ	[0;360]	10	-	-	[-90:90]	2	-
13b	[16:400]	0.5λ	[0;90]	30	-	-	[0;90]	[15;30]	-
13c	100	0.5λ	[0;360]	[10;30]	-	-	0	[2;10;30]	-
13d	100	[0:10] λ	0	[10;40]	-	-	0	[5;20]	-
14a	[16:400]	0.5λ	[0;90]	-	30	-	[0;90]	-	[15;30]
14b	100	0.5λ	[0;360]	-	[10;30]	-	0	-	[2;10]
14c	100	[0:10] λ	0	-	[5;20]	-	0	-	[5;20]

2.2.2.1 One-ring Model with ULA

Next, we analyze the channel models for M-MIMO and XL-MIMO systems based on the geometry, starting with the 2D models for scenarios where the user is around the scatterers uniformly distributed *i.e.* the one-ring geometry, as defined in eq. (2.10). First, the capacity was analyzed when the nominal AoA φ and the angular spread Δ are varying, as illustrated in Fig. 2.8. Indeed, if we imagine a horizontal ULA, we can suppose that perpendicular angle of arrival will present higher capacity than parallel ones, because parallel angles result in antennas strongly correlated, hence, smaller capacity.

This behaviour is observed in Fig. 2.8.b, in which the angles 0° and 180° represent the perpendicular angles to the antennas array and the angles 90° and 270° represent the parallel angles to the antennas. We also observed that the angular spread Δ can result in an increase in the capacity. The Δ is related to how close the angle of the signals received from each multipath component are, indicating that the arrived signals may be correlated according to the value of Δ .

Aiming to verify if the behavior of capacity according to Δ is due to the spatial

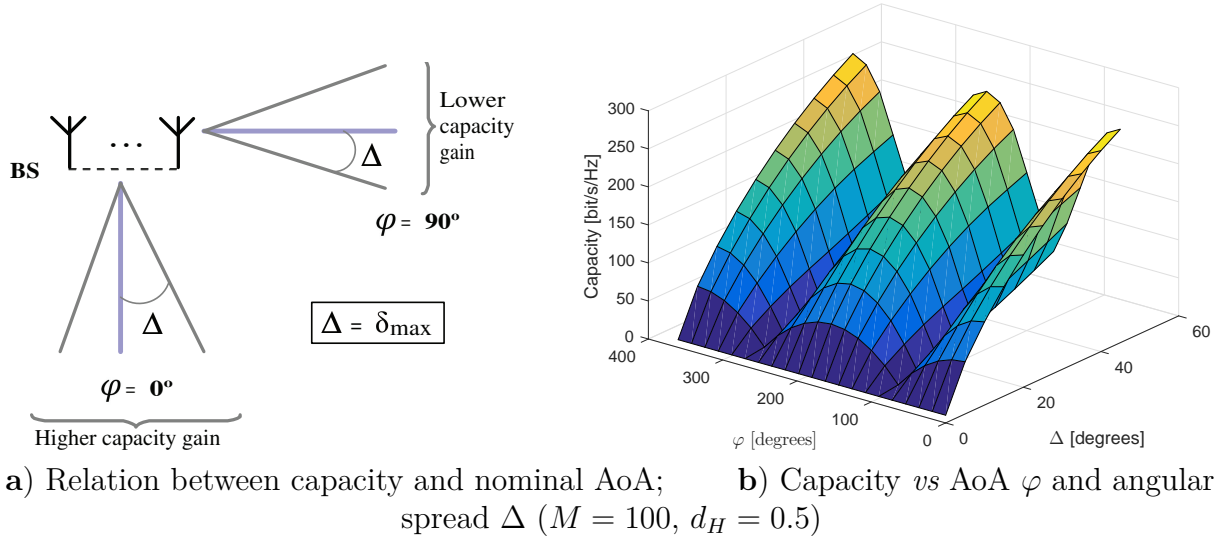


Figure 2.8 – Capacity analysis in geometric-based stochastic models (GBSM) according to the AoA considering ULA arrangements. a) Illustration of the relation between capacity and nominal AoA. b) Capacity analysis vs AoA and Δ .

correlation, we analyzed the *condition number* (CN), *i.e.* the ratio between the maximum (σ_{\max}) and the minimum (σ_{\min}) singular value related to the channel matrix \mathbf{A} (BELSLEY et al., 1980):

$$\kappa(\mathbf{A}) = \frac{\sigma_{\max}}{\sigma_{\min}} \quad (2.32)$$

In our massive MIMO channel analysis, the CN is used as an environmental characterization metric and it can express the spatial correlation degree of a correlation channel matrix (COSTA; HAYKIN, 2011). As well known, if a matrix is correlated, only the first singular value is representative, while the others result in "small" singular values, indicating that the matrix is near to the singularity. Hence, in Fig. 2.9, one can see that the CN has decreased with the increasing of Δ ; however, such values remain high due to the high correlation associated with the One-ring channel model. Therefore, the behavior seen in Fig. 2.8.b with respect to Δ is due to the degree of correlation in the One-ring model, in which the higher the degree of correlation, the lower capacity.

In order to compare the capacity values of the GBSM and CBSM models, Fig. 2.10 depicts the variation of capacity with Δ , AoA, number of antennas M and normalized distance between antennas $\frac{d_H}{\lambda}$. Fig. 2.10.a analyzes the capacity as a function of Δ assuming fixed the nominal angles of arrival in $\varphi = 0^\circ$ and 90° , representing the best and worst case in terms of capacity for a wide range of Δ values. Hence, from the two AoA values, one can see that to Δ near zero, the capacity is small and approximately constant, *i.e.* independent of the nominal angle of arrival φ . However, one can see a huge difference of almost 190 bit/s/Hz with $\Delta = 45^\circ$. Moreover, even with the increase of Δ , nominal angles of 90° and 270° do not increase significantly the capacity when compares to 0° and 180° . Such behavior is justified if we imagine two arrival angles $\varphi = 0^\circ$ and $\varphi = 90^\circ$; in the first case, the ULA would receive the signals with the best AoA and the in the

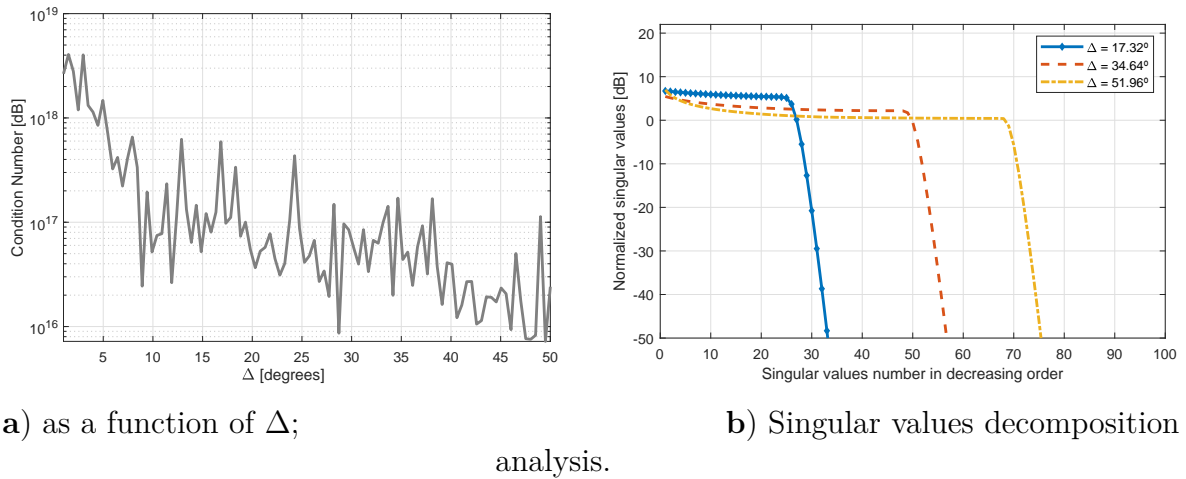


Figure 2.9 – a) Condition number when the angular spread is increased; b) Singular values for different angular spread.

second case the ULA would receive the signals with the worst AoA, thus, even as the Δ increases, the capacity will increase much fast for the first case than for the second case. Moreover, comparing GBSM with CBSM model (section 2.2.1), one can observe a similarity in GBSM behavior with respect to Δ and the correlation factor presented in 2.5.b), where the correlation factor and Δ are inversely proportional. Capacity behavior according to the number of antennas was analyzed in Fig. 2.10.c). For any angle of arrival and with a nonzero Δ , the capacity increases with the number of antennas. However, the observed capacity values are very low if compared with the Exponential model of Fig. 2.5.a). According to the geometric model, the obtained capacity does not exceed 500 bit/s/Hz, being this value compared to the CBSM with a correlation factor between 0.8 and 1. Moreover, we see that the difference in the capacity is more pronounced between the angles φ when the number of antennas increases. The last analysis was developed according to the distance between the antennas presented in Fig. 2.10 d). As the distance increased, we observed that capacity increased, and capacity remained constant over a certain distance. This behavior is related to the degree of correlation between the antennas, where with increasing spacing, the degree of correlation decreases. The fact that capacity reaches a limit indicates that the antennas are completely uncorrelated. The difference between $\Delta = 10^\circ$ and $\Delta = 30^\circ$ is that under the latter angular spread the signals are more uncorrelated, thus, the capacity increases with a distance smaller than $\Delta = 10^\circ$.

2.2.2.2 Gaussian Model with ULA

The second GBSM is the Gaussian Local Scattering Model defined in eq. (2.14). Unlike the One-ring model, in the Gaussian model the spreaders are around to the user with Gaussian distribution, suggesting that in a propagation environment some spreaders are more likely to influence signals arriving at the BS. The first analysis was performed

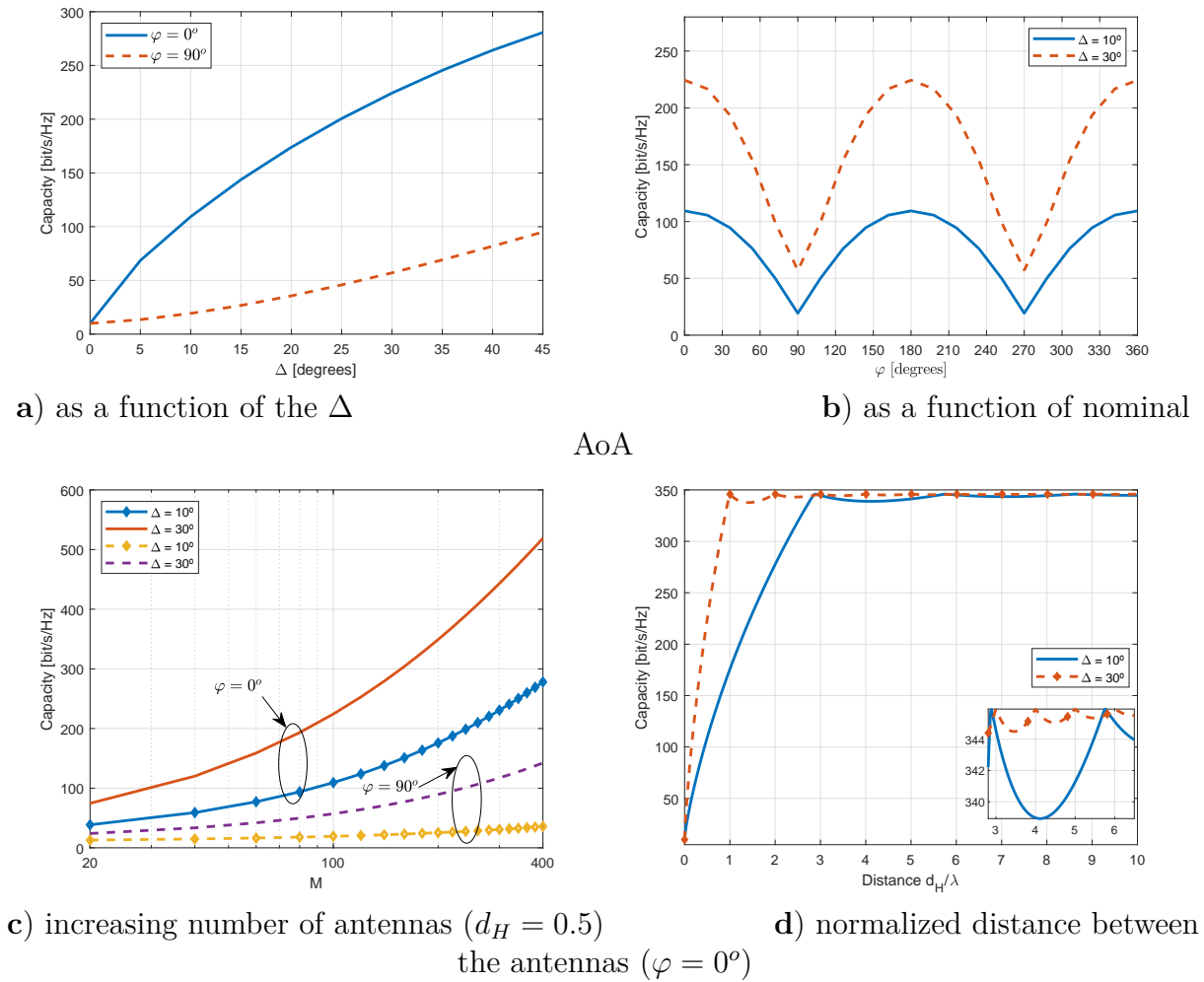
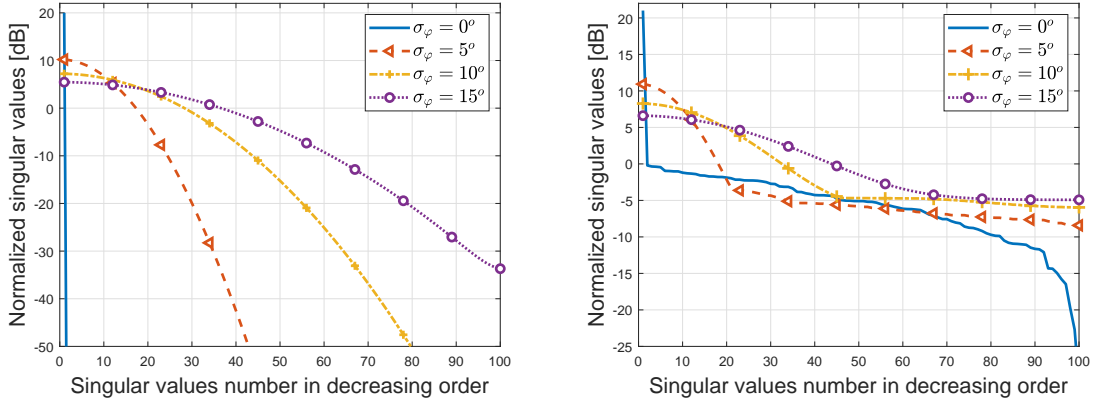


Figure 2.10 – One-ring model with $M = 100$ antennas. Capacity analysis according to a) Δ ; b) AoA; c) number of antennas; d) distance between antennas.

by analyzing the capacity when the σ_φ increases. Such behavior is similar to Δ and it was explained for the One-ring model using CN metrics. Even knowing that σ_φ affects the degree of correlation between signals, we analyze the singular values, but in order to verify the influence of shadowing on signal correlation. In Fig. 2.11, there are two cases, the first without the shadowing effect, Fig. 2.11.a, and the second with shadowing of 2 dB, Fig. 2.11.b. Clearly one can see that increasing shadowing standard deviation implies in decreasing the difference between the largest singular value and the smallest singular value, resulting in a better (smaller) condition number. Such result is understandable if we realize that each antenna receives a signal with a shadowing amplitude distinct from the shadowing amplitude of another antenna, such amplitude being given by a random variable and uncorrelated to the other one¹.

In Fig. 2.12 one can check the capacity value for $M = 100$ antennas under the Gaussian local scattering model with ULA when varying the angular standard deviation

¹See the definition of correlation elements in the Gaussian Local Scattering Model, eq. (2.14), as well as the random fluctuation of the large-scale fading f_m description in eq. (2.2)

a) Singular values for shadowing $\sigma_{\text{shad}} = 0$ dB;

b) Singular values for shadowing

 $\sigma_{\text{shad}} = 2$ dB.

Figure 2.11 – Singular values decomposition analysis for the GBSM Gaussian local scattering model

(ASD, σ_φ) and AoA. One can infer the gain that ASD provides; however, at angles close to $\varphi = 90^\circ$ and $\varphi = 270^\circ$ the models suggest that there is no gain (eq. (2.14)). Thus, the capacity remains constant regardless of the presence of shadowing. We also see that shadowing has a greater influence on capacity than the increase in ASD itself; so, we can see that for ASD equal to zero we have a capacity gain of 500 bit/s/Hz with a shadowing standard deviation of 4 dB, *i.e.*, even though both variables result in a reduction in the degree of correlation, shadowing has a greater impact than angular scattering. Also, we have observed that due to the signals from each antenna are more uncorrelated when the shadowing value is higher, the impact of the arrival angle on the degree of signal correlation is smaller, resulting in less impact on capacity.

Another analysis for the Gaussian model is related to the increase of the number of antennas presented in Fig. 2.12.c. For this case, we also check the dependence with three shadowing values. The capacity gain was exponential for this model as well as the previous models. If we compare the capacity gain provided by this model without shadowing against the One-ring model, one can see that both models are similar, despite the Gaussian model resulting in a greater gain that presented by the One-ring. channel model. Finally, Fig. 2.12.d demonstrates that the channel capacity under the Gaussian model in ULA antenna arrangement increases when distance between antenna array elements increases as well, but unlike the One-ring model, at a certain distance the capacity remains constant without slight oscillations. Anyway, in both channel models when the capacity is stabilized with antenna distance increasing, such capacity values become very close.

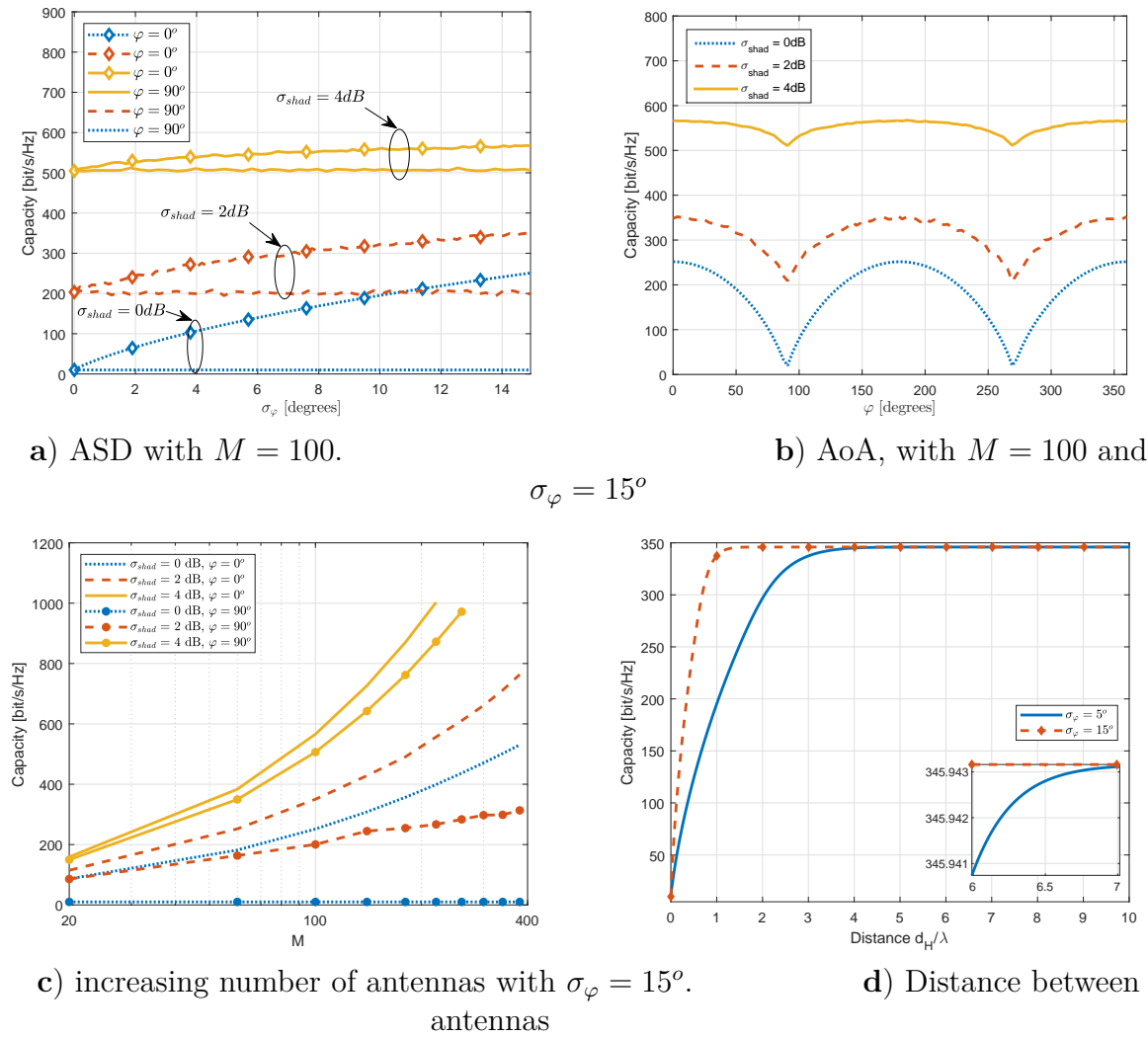


Figure 2.12 – Gaussian Local Scattering Model (approximate expression). Capacity analysis according to: a) ASD; b) AoA; c) increasing M ; d) normalized distance between antennas.

2.2.3 3D Models

2.2.3.1 One-ring Model with UPA

The next analysis is related to GBSM with UPA. In a model where the antennas array configuration is planar, we have to analyze not only the azimuth angle, φ , but also the elevation angle, θ . First, the capacity behavior is presented according to the nominal angles in Fig. 2.13.a. For the azimuth angles, the better arrival angles are the same demonstrated to ULA. Indeed, using ULA, one can identify that the elevation angles is not a determinant factor on the system performance, while in UPA the elevation angle affects greatly the channel capacity. As one can suppose or infer, the better angle is perpendicular to the azimuth and the elevation *i.e.* when both is equal to 0° , the capacity is maximum, as depicted in Fig. 2.13.a. Capacity behavior according to the number of antennas is also analyzed and presented in Fig. 2.13.b, when the nominal angles are equal to 0° (best case)

and equal to 90° (worst case). Previously, we saw that the UPA is limited by elevation and azimuth angles while ULA is only limited by azimuth angle. In fact, the UPA presents the advantage to perform the beamforming and a more versatile and compact spatial arrangement of antennas, but the capacity is smaller than ULA; for instance, one can see that the capacity value is $C \approx 100$ bit/s/Hz when the BS is equipped with an UPA arranged as $M_h \times M_v \equiv 20 \times 20$ antennas. Moreover, from previous analysis to the ULA, we know that the Δ defines the range of the arrival angles. Thus, we can conclude that for the UPA the same behavior will be verified, in which when Δ_φ and Δ_θ increase, the arrival signals become less correlated, and therefore increasing the capacity. We analyze the capacity for some fixed values of Δ , being the elevation nominal angle defined as 0° . According to Fig. 2.13.c, one can notice that the higher the value of Δ , greater the capacity; however, the capacity only increases significantly if both Δ_φ and Δ_θ increase simultaneously. As we know, when the BS is equipped with ULA, the elevation angle does not interfere on the capacity, unlike the UPA. Thus, the channel capacity using UPA arrangements is reduced compared to the ULA models. Lastly, the capacity is investigated according to the vertical and horizontal antenna spacing for different values of Δ_φ and Δ_θ . From this analysis, one can see that when both Δ_φ and Δ_θ are simultaneously larger, the capacity is increased faster considering small vertical/horizontal antenna separation distances. The same oscillation characteristic observed in the One-ring channel model when the BS is equipped with ULA is also confirmed with UPA arrangements, where the capacity is also limited in $C \approx 350$ bit/s/Hz, due to the number of antennas is the same in both situations.

2.2.3.2 Gaussian Model with UPA

The second 3D channel model for massive MIMO systems is the Gaussian model with UPA arrangements. As a numerical result, the channel capacity with increasing number of antennas is presented in Fig. 2.14 a. One can observe that when BS is equipped with both ULA and UPA, the Gaussian model results in a higher capacity than that provided by One-ring model, considering the same nominal values of Δ and σ , *i.e.*, the spread range is not equivalent in both models. Hence, with a uniform distribution, the spread is limited differently when compared with a Gaussian distribution, thus the angular range for the arrival signals in Gaussian model is larger, resulting in greater capacity gain. Moreover, the arrival angles are analyzed in Fig. 2.14 b. When compared with the One-ring UPA model, Fig. 2.13.c, considering the same AoA and number of antennas, the Gaussian model presents higher channel capacity, since we know that this behavior is related to the antenna array geometry. For instance, the channel capacity predicted by the Gaussian UPA model when the nominal angles equal to zero and the respective standard deviations $\sigma_\varphi = 30^\circ$ and $\sigma_\theta = 10^\circ$, the capacity is almost 200 bit/s/Hz while the One-ring UPA model predicts a capacity of $C \approx 105$ bit/s/Hz. The fact that the Gaussian model provides a

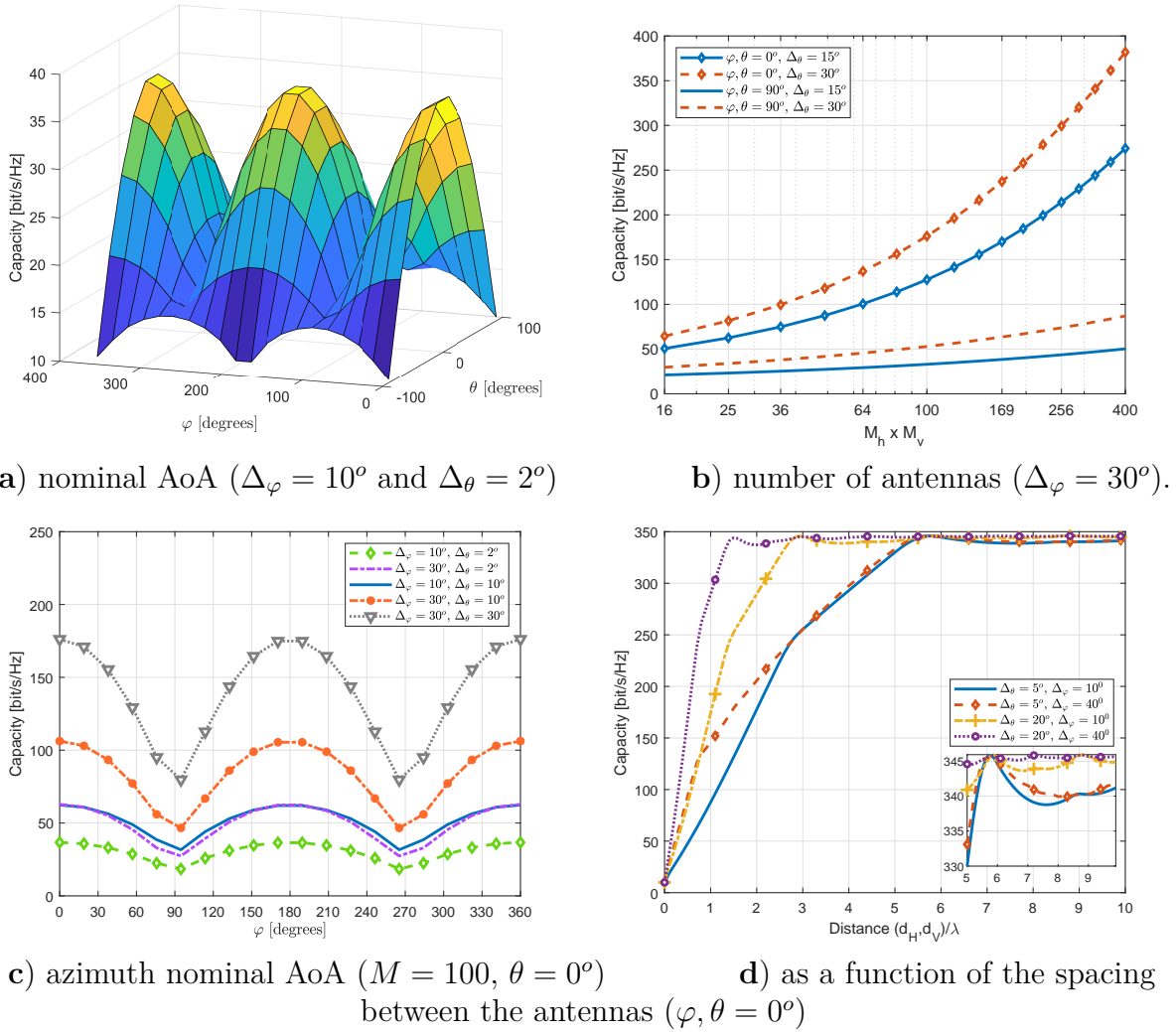
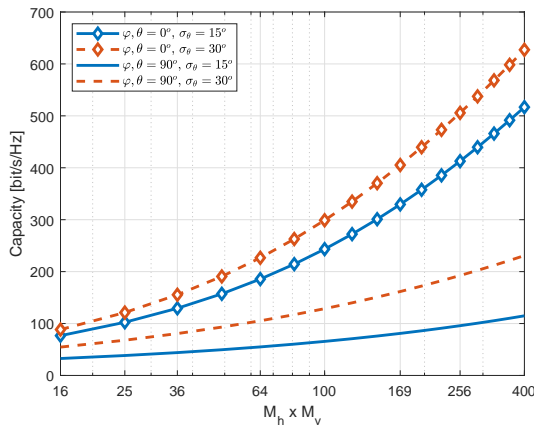


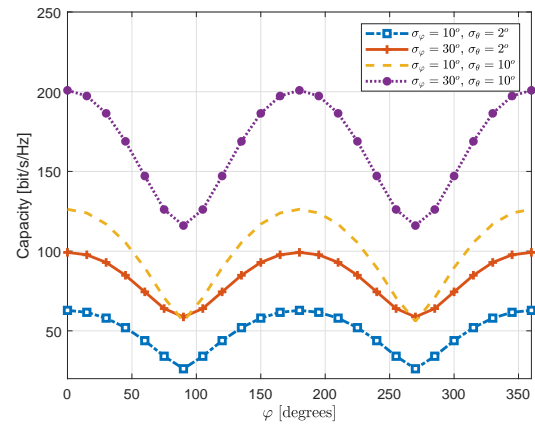
Figure 2.13 – One-ring Model with UPA. Capacity analysis according to: a) the nominal angles of azimuth and elevation; b) increasing M_h and M_v simultaneously; c) the azimuth nominal angle; d) increasing the horizontal and vertical spacing between the antennas.

larger angular arrival range than the One-ring model can be confirmed when we increase the $\Delta_\theta = 30^\circ$ as depicted in the same Fig. 2.13.c. The capacity in this case is $C \approx 175$ bit/s/Hz, even smaller compared to that predicted by the Gaussian UPA model.

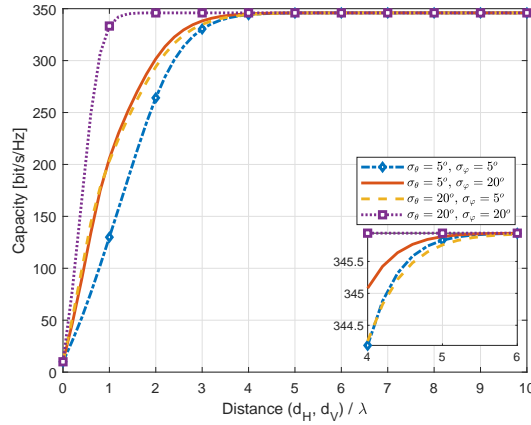
Finally, the behavior of the channel capacity based on Gaussian UPA model according to the spacing between the vertical/horizontal antennas is shown in Fig. 2.14.c. As explained previously, the spacing between antennas is related to the degree of signal correlation and therefore the capacity increases with increasing antenna separation until saturate in $C \approx 350$ bits/s/Hz. In this analysis we simulate at first $\sigma_\theta = 5^\circ$ and $\sigma_\varphi = 20^\circ$ and in a second moment we analyze the capacity when $\sigma_\theta = 20^\circ$ and $\sigma_\varphi = 5^\circ$. Hence, the capacity results quite similar, evidencing the fact that the increasing in the spread range, measured by the standard deviation in the elevation σ_θ and the azimuth σ_φ angles, implies in a consistent increment in thr channel capacity.



a) as a function of the number of antennas M ($\sigma_\varphi = 30^\circ$)
($M = 100$, $\theta = 0^\circ$)



b) azimuth nominal AoA



c) as a function of the spacing between the antennas ($\varphi, \theta = 0^\circ$ and $M = 100$).

Figure 2.14 – Gaussian Model where BS is equipped with UPA. Capacity according to: a) increasing the number of antennas; b) azimuth nominal angle.

2.2.4 CBSM and GBSM Compared to Channel Measurements

To corroborate the validity of the proposed stochastic channel models, in this section a performance analysis of the CBSM and GBSM models are compared to the massive MIMO channel campaign measurement conducted in (HOYDIS et al., 2012). The channel measurements were performed outdoors with a scalable virtual antenna array consisting of up to 112 ULA elements, representing a residential urban area. The deployed CBSM and GBSM channel parameter values are depicted in Table 2.4.

Table 2.4 – Parameter values adopted in the numerical simulations for channel correlation analysis.

Parameters	Values
Exponential Model	
Path loss term	$\beta = 1$
Correlation index	$\rho = [0.8; 0.85]$
Exponential Model with Large Scale Fading	
Path loss term	$\beta = 1$
Correlation index	$\rho = 0.8$
Shadowing – standard deviation	$\sigma_{\text{shad}} = 0$ dB
Angle of arrival	$\theta \sim \mathcal{U}(0, \theta_{\text{max}})$ degrees
Maximum angle of arrival	$\theta_{\text{max}} = [60; 90; 180]$ degrees
One-ring ULA	
Path loss term	$\beta = 1$
Angular interval of the angles of arrival	$\Delta = 10$ degrees
Angle of arrival	$\varphi \sim \mathcal{U}(0, 180)$ degrees
Antenna spacing	$d_H = 0.5$
Gaussian ULA	
Path loss term	$\beta = 1$
Shadowing – standard deviation	$\sigma_{\text{shad}} = 0$ dB
Angular standard deviation	$\sigma_{\varphi} = 10$ degrees
Angle of arrival	$\varphi \sim \mathcal{U}(0, 180)$ degrees
Antenna spacing	$d_H = 0.5$

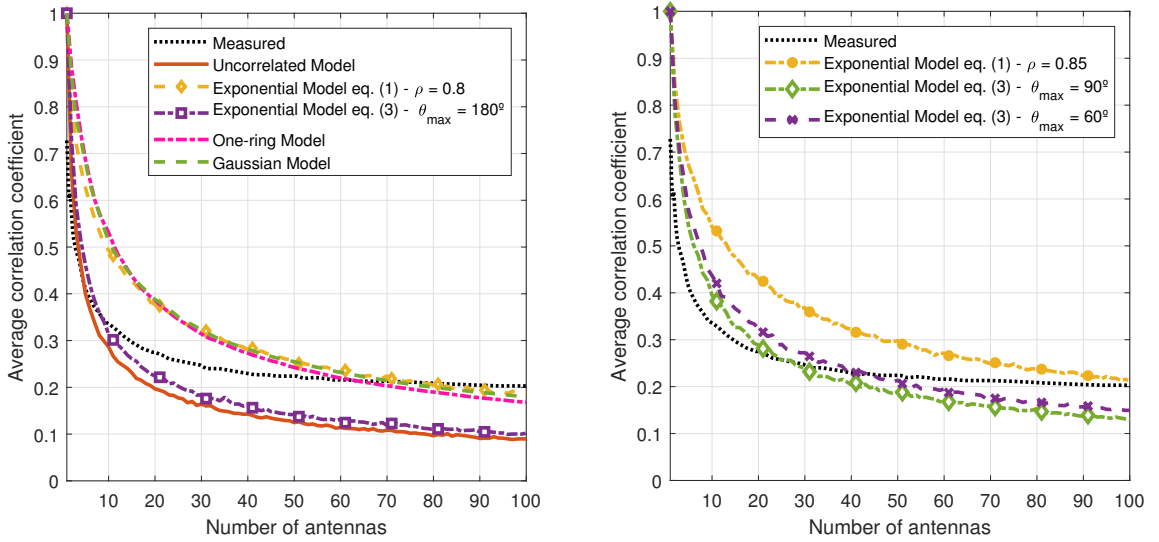
For this analysis, we used the correlation coefficient between two channel vectors defined with:

$$\nu(M) = \frac{|\mathbf{h}_{i,M}^H \mathbf{h}_{j,M}|}{\|\mathbf{h}_{i,M}\| \|\mathbf{h}_{j,M}\|} \quad (2.33)$$

where $\mathbf{h}_{i,M}$ and $\mathbf{h}_{j,M}$ are the channel vectors from the user i and user j , respectively. The correlation coefficients were evaluated according to the number of antennas M for the models in which the BS is equipped with ULA. The results obtained for this simulation are depicted in Fig. 2.15.

First, we can observe that both the measurement and the channel models show a decreasing correlation behavior with the increase in the number of antennas. This result is due to the favorable propagation massive MIMO property, in which the orthogonality of the channels between users is attained when the number of antennas increases. According to the data of the measured values, it is possible to observe that the correlation has a rapid decay when the number of antennas increases in the range $[1; 10]$. However, the correlation decays very slow, remains with few variations, when the number of antennas exceeds 50, *i.e.*, characteristic values of a massive MIMO system. In Fig. 2.15a, if we divide the analysis according to the number of antennas, we see that the uncorrelated model and the exponential model with large-scale fading better capture the channel conditions for

this outdoor channel measurement scenario. However, for a larger number of antennas, the GBSM models and the exponential model behave similarly to the measured values. Moreover, in Fig. 2.15b, some channel model parameter values have been modified aiming at better fitting the measured channel. Hence, for the exponential model, we increased slightly the value of the correlation factor while for the exponential model with large-scale fading, the arrival angle was reduced from $\theta_{\max} = 180^\circ$ to $\theta_{\max} = 90^\circ$ and 60° . We observed that the angle of arrival θ affects the correlation, in which for smaller values, the correlation coefficient increases. Such behavior is related to the confinement of the arrival signals, that is, if the θ assumes smaller values, the signals will be confined to a smaller angular interval. Therefore, given the results of each model, one can notice that this specific outdoor measurement environment presented a high degree of correlation, in which the parameters of each model could be adjusted in order to more accurately represent each environment.



a) comparison between CBSM and GBSM;

values for CBSM.

b) evaluation of other parameter

Figure 2.15 – Average correlation coefficient according to the ULA number of antennas : channel measurement vs CBSM and GBSM channel models with adjusted parameters.

2.2.5 XL-MIMO channel model

In this section the validation of the analyzed XL-MIMO channel models is corroborated numerically. The adopted channel and system parameters values were described in Table 2.1. To evaluate the XL-MIMO scenario, it was used the SINR as a figure of merit for the k th user as:

$$\gamma_k = \frac{|\mathbf{h}_k^H \mathbf{g}_k|^2}{\sum_{\substack{j=1 \\ j \neq k}}^K |\mathbf{h}_k^H \mathbf{g}_j|^2 + \sigma^2} \quad (2.34)$$

where σ^2 is the noise power, \mathbf{g}_k and \mathbf{h}_k are the precoding and channel vectors from user k , respectively

It is worth to note that across the numerical results section, the path loss of each XL-MIMO channel $\mathbf{h}_{k,c}$ has been normalized by the inverse of path loss gain, i.e., $A = \tilde{d}^\alpha$, defining the adopted power allocation policy.

First, we present an analysis of the algorithm to create the visibility region (VR). The algorithm was constructed so that obstructions usually involve more than one antenna, *i.e.* the obstacle impacts on the received signal strength along the array antennas. Also, as distances between mobile terminal and BS antenna array are close, the likelihood of no obstacles is high. Fig. 2.16 depicts an example of VR with obstructions generated randomly and the correspondent histogram indicating the number of visible (active) antennas. From the histogram, one can infer that it is highly probable that the $\approx 75\%$ of antennas (*i.e.*, 24 to 27 of 33 antennas) become visible or even 100% of the antennas lie in the visibility region.

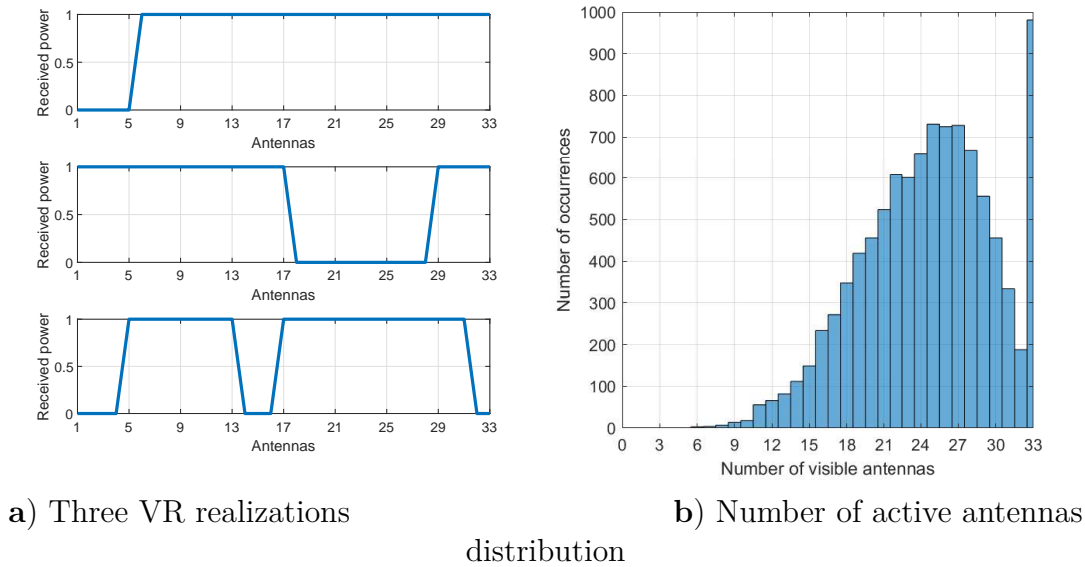


Figure 2.16 – VR generation algorithm considering ULA with $M = 33$ antennas: a) Example of three VR, where the obstacles result in a received power equal to zero; b) histogram of the number of active antennas.

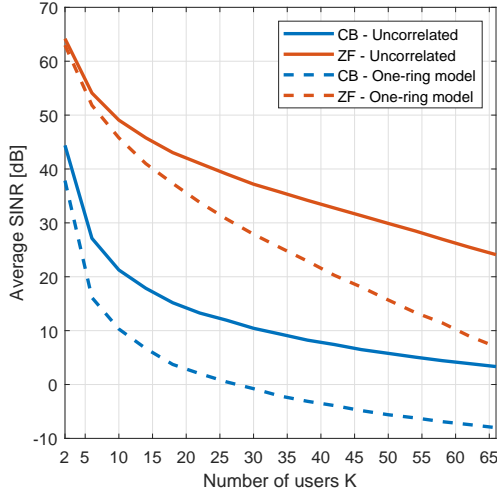
Besides, the SINR analysis considering both schemes of *cluster distribution* sketched in Fig. 2.4, as well as both linear precoding conjugate beamforming (CB) and zero-forcing (ZF) and three correlated channel models, namely Uncorrelated fading, Exponential and One-ring have been carried out. Firstly, we compare the average SINR by user attainable with CB and ZF precoding for the first cluster distribution scheme from Fig. 2.4.a, considering the correlation matrix as i.i.d. Rayleigh and the One-ring channel model, as depicted in Fig. 2.17.a and 2.17.b. The uncorrelated fading model implies that there is not correlation between antennas, unlike the One-ring model in which the channel correlation is implicit in the received signal via spread Δ parameter and between the

antennas, according to the azimuth angle φ . Hence, the achievable SINR considering both CB and ZF precoding under uncorrelated channel model is higher than that attainable under One-ring channel model and the respective linear precoding for any number of users. However, when the number of users increases, the SINR is reduced, considering both linear precoders, while the SINR values difference provided by the uncorrelated *vs* One-ring channel models increases. Indeed, the behaviour of the SINR is similar considering both linear precoders, but CB and ZF linear precoders implement different rules. The CB precoding focus is on increasing the power of the desired user, while, the ZF focus on decreasing or virtually reduce to zero the power interference. Thus, one can observe that the ZF precoding presents higher SINR's than the CB; however, it is known that there is a maximum number of users in which the ZF can eliminate completely the interference, and when that value is exceeded, the performance of the ZF precoding is reduced.

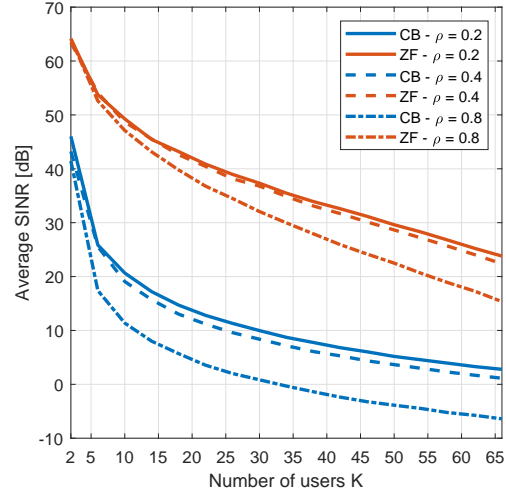
Furthermore, as the Exponential channel model depends of the correlation factor, the analysis was developed separately and presented in Fig. 2.17.b. One can observe that the reduction in the SINR is impacted by the system loading $\frac{K}{M}$, as well as by the increase of the correlation factor ρ . As discussed previously, in the Fig. 2.5.b), the channel capacity is reduced substantially when the channel correlation factor approach to 1, being this impact more pronounced when the correlation factor is $\rho > 0.6$. Hence, the same characteristic is corroborated for the SINR analysis in Fig. 2.17 when the $\rho = 0.8$.

Considering the second cluster distribution scheme where all users are aligned and parallel to the ULA arrangement, as sketched in Fig. 2.4.b, we calculate the average SINR performance when the One-ring and uncorrelated fading channel models are considered; the results are depicted in Fig. 2.17.c and 2.17.d. The behavior of the SINR is same for the uncorrelated if compared to the first scheme. However, for the One-ring model the attainable SINR is higher than that achieved under the first cluster distribution scheme. The reason of the first scheme presented worst performance is due to distribution region of the clusters are in locations where the received signal is perpendicular to the antenna array, increasing the correlation between the antennas (see Fig. 2.8). Finally, in the Fig. 2.17.d, the Exponential channel model under second cluster distribution scheme is analyzed. The same SINR gain can be observed comparing Fig. 2.17.b and 2.17.d for the Exponential channel model. The results demonstrate that the attainable average SINR provided by each linear precoding depends strongly on the signal propagation environment. Nevertheless, only the One-ring model properly describes the propagation characteristics because it is a geometric-based channel model. Thus, the Uncorrelated and Exponential channel models do not show SINR performance differences because they are correlation-based models, where for the Exponential model, the impact of environmental propagation on the degree of correlation is indirectly considered by a correlation factor. From our numerical simulated results, one can infer that for the second cluster distribution scheme using the One-ring model, an Exponential model with a correlation factor of $\rho = 0.8$ have resulted

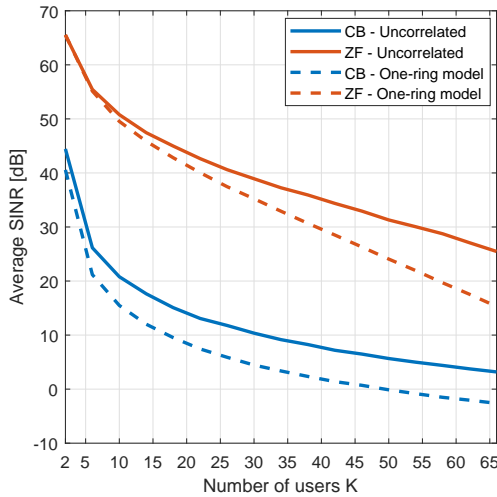
in a similar SINR behavior, indicating a high degree of correlation for this distribution on the One-ring model.



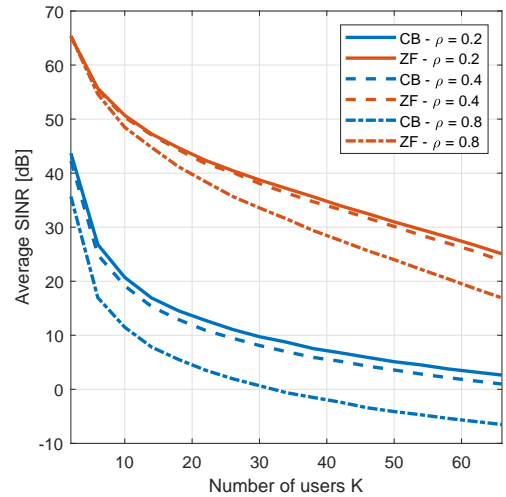
a) First scheme of clusters distribution



b) First scheme of clusters



c) Second scheme of clusters distribution



d) Second scheme of clusters

Figure 2.17 – Attainable SINR as a function of number of users (K) for two schemes of clusters distribution: a) Correlation matrix \mathbf{R} is modelled by Uncorrelated and One-ring models; b) \mathbf{R} is modelled by Exponential channel model. c) Second scheme of clusters distribution: \mathbf{R} is modelled by Uncorrelated and One-ring model; d) \mathbf{R} is modeled by Exponential channel model.

2.3 Conclusions

Channel models for massive MIMO and extreme large (XL) MIMO systems addressing relevant features implicit in such rich and innovative communication system scenarios are not completely available in the literature. Recent works have investigated stochastic

channel models, such as correlated-based (CBSM) and geometric-based (GBSM) stochastic models due to the possibility of implementing massive MIMO channel models with low-computational complexity and considering physical characteristics of signal propagation. This paper focused on an extensive analysis and comparison of these channel models in both stationary and non-stationary scenarios aiming at M-MIMO and XL-MIMO applications. We have discussed how the characteristics such as shadowing, angle of arrival, and angular spread can emulate the channel correlation degree implicitly. Among 2D and 3D GBSMs, the 2D channel model presents higher capacity gain due to the possibility of the received signals between the antennas result uncorrelated at any elevation angle. However, the model with the highest capacity gain is the CBSM. Although the CBSM model presented higher capacity gain, for the XL-MIMO applications, both channel models when compared considering two representative cluster distribution schemes, only the GBSM model has resulted SINR performance variations. Thus, the GBSM model proved to be more suitable for XL-MIMO channel modelling, since the propagation parameters are considered in the model.

3 Linear Combiners for Massive and Extra Large Scale MIMO

In this chapter, we present the M-MIMO and XL-MIMO system, analyzing the combination schemes from an imperfect channel knowledge.

3.1 Massive MIMO systems

For M-MIMO systems, we describe the process of channel estimation and signal detection from a group of cells. Thus, in each cell, communication is carried out between BS and users located within its own cell. The performance of combiners with respect to spectral efficiency is discussed, in which we evaluate the impact of channel correlation and pilot contamination. The combining schemes evaluated are the MRC, ZF, and the M-MMSE.

3.1.1 Uplink mode for M-MIMO systems

The uplink (UL) and downlink (DL) mode can be performed using a time-division duplex (TDD) protocol. Thus, the channel response is the same in UL and DL due to the principle of reciprocity, where the UL and DL times are small compared to the channel coherence time. To process the UL and DL, BS needs to know the channel response. A method for acquisition of the channel response is through pilot signaling. For this, it is transmitted a pilot signal, where each signal is orthogonal to the other and known at the receiver. Thus, when the pilot signal is received, the receiver can estimate and separate the signals from the transmitting antenna.

The received pilot signal at the BS j is describes by:

$$\mathbf{Y}_j^p = \sum_{i=1}^K \sqrt{\rho_{ul}} \mathbf{h}_{ji}^j \phi_{ji}^T + \sum_{l=1, l \neq j}^L \sum_{i=1}^K \sqrt{\rho_{ul}} \mathbf{h}_{li}^j \phi_{li}^T + \mathbf{N}_j^p \quad (3.1)$$

where ρ_{ul} is the pilot signal power, \mathbf{h}_{li}^j is the channel between UE i in the cell l and the BS j , $\phi_{li}^T \in \mathbb{C}^{\tau_p}$ is the pilot sequence used by UE i in cell l , $\mathbf{N}_j^p \in \mathbb{C}^{M \times \tau_p}$ is the receiver noise with i.i.d. elements distributed as $\mathcal{N}_{\mathbb{C}}(0, \sigma_{ul}^2)$ and τ_p is the number of samples for UL pilots.

For the channel estimation, it is used the MMSE estimator, being the estimated channel given by:

$$\hat{\mathbf{h}}_{li}^j = \sqrt{\rho_{ul}} \mathbf{R}_{li}^j (\mathbf{Q}_{li}^j)^{-1} \mathbf{Y}_j^p \phi_{li}^* \quad (3.2)$$

and

$$\mathbf{Q}_{li}^j = \sum_{(l',i') \in \mathcal{P}_{l,i}} \rho_{ul} \tau_p \mathbf{R}_{l'i'}^j + \sigma_{ul}^2 \mathbf{I}_M \quad (3.3)$$

where \mathbf{R}_{li}^j is the correlation matrix between UE i in the cell l and the BS j , $\mathbf{R}_{l'i'}^j$ is the correlation matrix of the UE i in the cell l that shares the same pilot sequence as the user i in the cell j , so that the set is defined as $\mathcal{P}_{jk} = \{l = 1, \dots, L, i = 1, \dots, K_l\}$. Thus, K_l is the number of users in each cell and, by definition, $(j, k) \in \mathcal{P}_{jk}$.

After the receiver estimates the channel response, we can detect the payload data transmission, using combining schemes. The received data signal at the BS j is given by:

$$\mathbf{y}_j = \sum_{i=1}^K \mathbf{h}_{ji}^j s_{ji} + \sum_{l=1, l \neq j}^L \sum_{i=1}^K \mathbf{h}_{li}^j s_{li} + \mathbf{n}_j \quad (3.4)$$

where $s_{ji} \sim \mathcal{N}_{\mathbb{C}}(0, \rho_{ul})$ is the signal from UE i in the cell j and \mathbf{n}_j is a vector whose m th element, n_m , is the additive noise at the m th antenna.

Thus, the BS selects a combining scheme $\mathbf{v}_{jk} \in \mathbb{C}^{M \times 1}$ that uses the channel estimation obtained from the pilot signaling, and correlates the combining scheme with the received signal \mathbf{y} as:

$$\mathbf{v}_{jk}^H \mathbf{y}_j = \underbrace{\mathbf{v}_{jk}^H \mathbf{h}_{jk}^j s_{jk}}_{\text{Desired signal}} + \underbrace{\sum_{i=1, i \neq k}^K \mathbf{v}_{jk}^H \mathbf{h}_{ji}^j s_{ji}}_{\text{Intra-cell interference}} + \underbrace{\sum_{l=1, l \neq j}^L \sum_{i=1}^K \mathbf{v}_{jk}^H \mathbf{h}_{lk}^j s_{li}}_{\text{Inter-cell interference}} + \underbrace{\mathbf{v}_{jk}^H \mathbf{n}_j}_{\text{Noise}} \quad (3.5)$$

where $(\cdot)^H$ is the Hermitian operator. The intra-cell interference is the interference generated by other users in the same cell j while the inter-cell interference is the interference created by other users from other cells l .

3.1.2 Linear Combiners

3.1.2.1 MRC Scheme

MRC is the simplest and lowest computational cost detector, where the focus of this detector is to maximize the power of the desired signal. The MRC combiner is defined as:

$$\mathbf{v}^{(j) \text{ MRC}} = \hat{\mathbf{H}} \quad (3.6)$$

where $\hat{\mathbf{H}}$ matrix channel estimative.

3.1.2.2 ZF Combining Scheme

Compared to MRC, the complexity is greater due to the presence of the matrix inverse, where the focus of ZF is to mitigate interference from other users. The ZF combiner is defined as:

$$\mathbf{V}^{(j)\text{ZF}} = \hat{\mathbf{H}}(\hat{\mathbf{H}}^H \hat{\mathbf{H}})^{-1} \quad (3.7)$$

3.1.2.3 M-MMSE Combining Scheme

The classical combining schemes consider that the BS estimates only the channel of its own users. However, when considering the reuse of the pilot sequence, it is possible the presence of a strong intercell interference, because some users can be localized near to the cell edge. A method to mitigate the interference is considering the signal estimation of users from other cells. In (BJÖRNSON et al., 2018), it was presented the M-MMSE scheme that considers the channel estimate from the other cells. The M-MMSE combining maximizes the SINR by amplifying the desired signal and suppressing interference both intracellular and intercellular interference. The analysis indicate that the spectral efficiency grows unlimitedly even with the presence of pilot contamination; however, is showed that for mitigating the pilot contamination, the covariance matrices of the users that share the same pilot sequence have to be asymptotically linearly independent, *i.e.*, the channel model affects performance of SE. The M-MMSE combining is defined as:

$$\mathbf{V}^{(j)\text{M-MMSE}} = \left(\sum_{l=1}^L \hat{\mathbf{H}}_l^j (\hat{\mathbf{H}}_l^j)^H + \mathbf{Z}_j \right)^{-1} \hat{\mathbf{H}}_j^j \quad (3.8)$$

and

$$\mathbf{Z}_j = \sum_{l=1}^L \sum_{i=1}^K (\mathbf{R}_{li}^j - \Phi_{li}^j) + \frac{\sigma_{\text{ul}}^2}{\rho_{\text{ul}}} \mathbf{I}_M \quad (3.9)$$

where L is the number of cells, Φ_{li}^j is the correlation matrix of the estimated channel, σ_{ul}^2 is the noise power.

3.1.3 Asymptotic Analysis

In this section, we present a perception of the behavior of the SE when the number of antennas in the BS is very large. For asymptotic analysis, the following conditions are necessary (BJÖRNSON et al., 2017):

Assumption 1 - The correlation matrix \mathbf{R}_{li} satisfies

1. $\liminf_{M_l \rightarrow \infty} \frac{1}{M_j} \text{tr}(\mathbf{R}_{li}) > 0$
 2. $\limsup_{M_l \rightarrow \infty} \|\mathbf{R}_{li}\|_2 < \infty$
- for $l = 1, \dots, L$ and $i = 1, \dots, K_l$.

The first condition implies that $\text{tr}(\mathbf{R}_{l_i})$ grows proportionally with the number of antennas and the second condition implies that the signal energy is not concentrated in just a few spatial directions. The asymptotic results depend on how different the spatial correlation matrices of the UEs are, where this difference is measured by linear independence.

Assumption 2 - The correlation matrix \mathbf{R}_{jk} is asymptotically linearly independent of the correlation matrices from UEs that share the same pilot sequence. For this assumption, we present an example. Consider the correlation matrix $\mathbf{R} \in \mathbb{C}^{M \times M}$. This matrix is linearly independent of the correlation matrices $\mathbf{R}_1, \dots, \mathbf{R}_N \in \mathbb{C}^{M \times M}$ if

$$\|\mathbf{R} - \sum_{i=1}^N c_i \mathbf{R}_i\|_F^2 > 0 \quad (3.10)$$

for all $c_1, \dots, c_N \in \mathbb{R}$.

Example:

$$\mathbf{R} = \begin{bmatrix} \epsilon_1 & 0 & \dots & 0 \\ 0 & \epsilon_2 & \dots & 0 \\ \vdots & \vdots & \ddots & \vdots \\ 0 & 0 & \dots & \epsilon_M \end{bmatrix} \quad (3.11)$$

$$\mathbf{R}_1 = \begin{bmatrix} 1 & 0 & \dots & 0 \\ 0 & 1 & \dots & 0 \\ \vdots & \vdots & \ddots & \vdots \\ 0 & 0 & \dots & 1 \end{bmatrix} \quad (3.12)$$

if $\epsilon_1 \neq \epsilon_2 \neq \dots \neq \epsilon_M$, the two matrices are linearly independent. The asymptotically linear independence condition is similar, but it requires that the norm grows with M as showed:

$$\liminf_M \frac{1}{M} \|\mathbf{R} - \sum_{i=1}^N c_i \mathbf{R}_i\|_F^2 > 0 \quad (3.13)$$

In (BJÖRNSON et al., 2017), is presented a theorem that proves that if BS j uses M-MMSE combining with MMSE channel estimation, then the UL SE of the UE k in the cell j grows without bound as $M \rightarrow \infty$, if Assumption 1 holds and the correlation matrix \mathbf{R}_{jk} is asymptotically linearly independent of the set of correlation matrices \mathbf{R}_{li} with $(l, i) \in \mathcal{P}_{jk} \setminus (j, k)$. The reason for such behavior is due to the channel vectors estimated by the MMSE being linearly independent when the correlation matrices are independent. Thus, the performance of the M-MMSE combining/precoding depends of the users correlation matrices that shares the same pilot sequence, *i.e.*, if the M-MMSE combining is used, it is possible to create a combining vector to the user k , where this combining vector vanishes the pilot contamination due to the vector be orthogonal to the other users as presented in Figure 3.2.

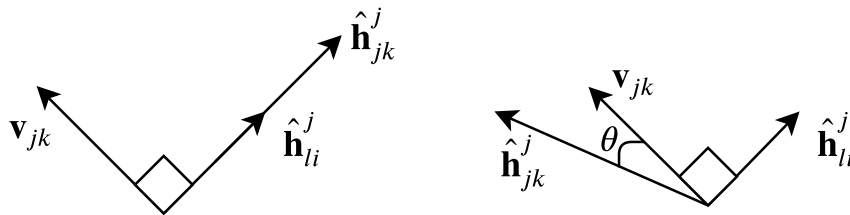


Figure 3.1 – Geometric illustration of how the combining vector \mathbf{v}_{jk} can reject the channel from the interfering user $\hat{\mathbf{h}}_{li}^j$.

3.1.4 Illustrative Numerical Results

In this section, we evaluated the SE according to the number of antennas and the SNR for M-MIMO system, considering three combining schemes: MRC, ZF, and M-MMSE. In the Table 3.1, we present the parameters used in the numerical Monte Carlo simulations.

Table 3.1 – Parameter values adopted in the numerical simulations.

Parameters	Values
Number of cells	5
Number of antennas at the BS M (fig. 3.3 a)	[16 32 64 128 256 512 1024 2048]
Number of antennas at the BS M (fig. 3.3 b)	128
Number of UEs K by cell	1
Distance between the BS and UEs from each cell	$d=[50 \ 150 \ 150 \ 150 \ 150]$ m
Path loss term \mathcal{L}	$-34.53 - 37.6 \log_{10}(d)$ dB
SNR _{dB} (fig. 3.3 a)	10 dB
SNR _{dB} (fig. 3.3 b)	[-5:5:25] dB
SNR	$\eta = 10^{\text{SNR}_{dB}/10}$
Noise power σ_{ul}	0.05 W
Signal power p_{ul} (fig. 3.3 a)	0.5 W
Signal power p_{ul} (fig. 3.3 b)	$\sigma_{ul}\eta$ W
Pilot reuse factor f	1
Coherence interval τ_c	200 symbols
Pilot length τ_p	1
Channel estimation method	MMSE
Correlation factor ρ	0.5
Azimuth angle θ_k	[0 0 90 180 270] degrees
Number of Monte Carlo realization	1000

In this analysis, we correlated channels modeled by the exponential given in eq. (2.3) without the shadowing effect. The analysis is simulated for a case with strong inter-cell interference, because all cells use the same pilot sequence, *i.e.*, pilot reuse factor equal to 1. The simulation scenario is shown in fig. 3.2, where user 1 of cell 1 shares the same pilot sequence with the other users who are located at the edge of their respective cells. According to the Figure 3.3(a), we observe an unlimited behavior of the M-MMSE and

the ZF combining, in which the M-MMSE presents a better performance. In addition, we observed very low values for the ZF with a small number of antennas. This behavior is caused by the poor conditioning of the inverted matrix of the combiner when the number of antennas is close to the number of UEs. For Figure 3.3(b), SE is assessed with respect to SNR. With a low SNR, the ZF had the worst performance while the MRC and the M-MMSE showed similar behaviors. With the increase in the SNR we observed a significant increase in the performance of the M-MMSE, approaching 9 bit/s/Hz. Finally, it is clear that with an SNR above 15 dB, the ZF has a higher SE compared to the MRC.

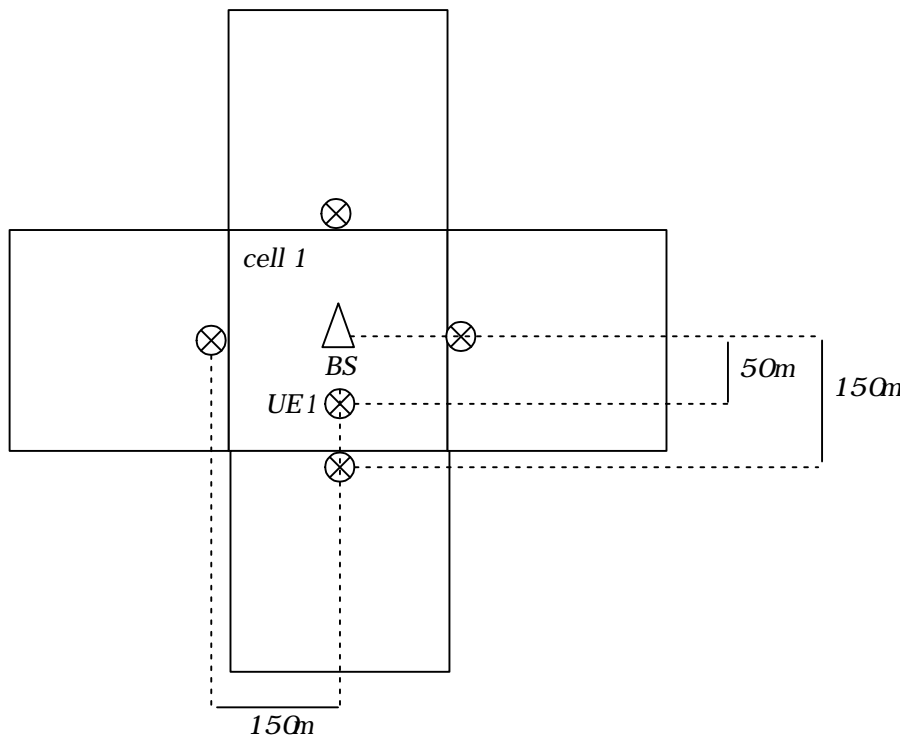


Figure 3.2 – Simulation scenario.

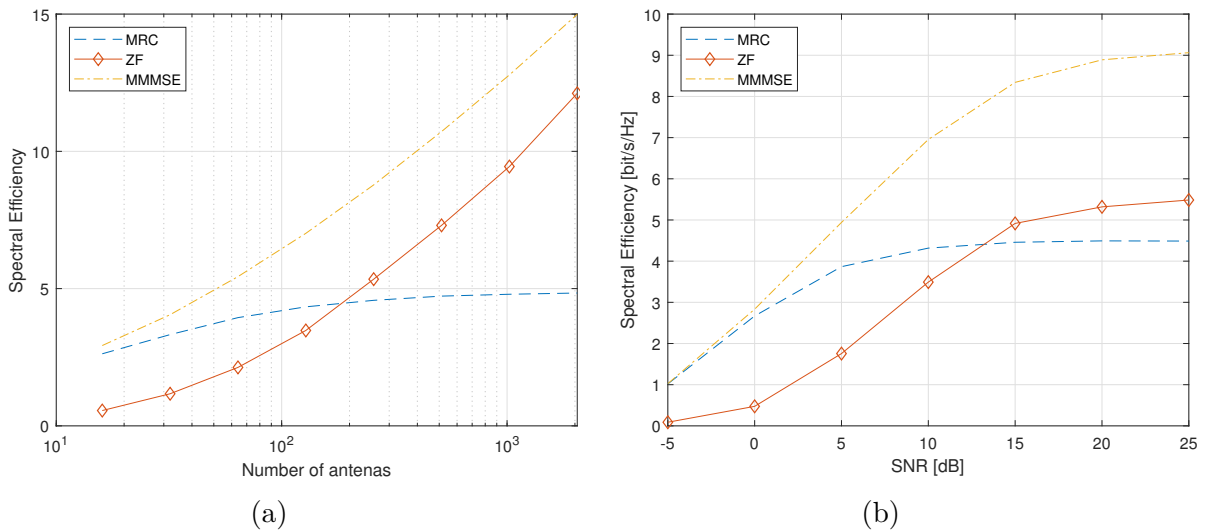


Figure 3.3 – SE analysis according to the number of antennas (a) and SNR (b).

3.2 Extra Large MIMO systems

For XL-MIMO systems, we describe the process of channel estimation and signal detection in a single cell. In this system, we consider that users use the same pilot sequence. Thus, we present the channel estimation equations and the modeled metrics for the proposed scenario, in which we evaluate the combination schemes: ZF, the RZF calculated by Kaczmarz randomized and the MMSE.

3.2.1 System Model

In this section, we describe the channel model for XL-MIMO as well as the combining schemes. In this system, there are M antennas at BS to serve K single-antenna users, where the channel estimation was performed by MMSE estimator. For the channel modelling, we consider two models: single and double scattering XL-MIMO channel models. In the single-scattering, there is just one linear cluster of scatterers between the BS and the user, while in the double-scattering model, there are two linear clusters in both sides of the communication, *i.e.*, a linear cluster of scatterers in BS and UE sides, respectively. Also, we present the ZF, RZF emulated by rKA, namely rKZF, and the MMSE combiner.

3.2.1.1 Uplink XL-MIMO

The uplink (UL) and downlink (DL) mode can be performed using a time-division duplex (TDD) protocol. Thus, the channel response is the same in UL and DL due to the principle of reciprocity, where the UL and DL times are small compared to the channel coherence time. To process the UL and DL, BS needs to know the channel response. A method for acquisition of the channel response is through pilot signalling. For this,

it is transmitted a pilot signal, where each signal is orthogonal (in a time period) to the other and known at the receiver side. Thus, when the pilot signal is received, the receiver can estimate and separate the signals from each transmitting antenna. Based on (SANGUINETTI et al., 2020), for the proposed system, we describe the pilot signal received and processed in the subarray b as:

$$\mathbf{Y}_{(b)} = \sum_{l \in \mathcal{K}_b} \sum_{i \in \mathcal{C}_{kb}} \sqrt{p_{ul}} \mathbf{h}_{li(b)} \boldsymbol{\phi}_l^T + \mathbf{N} \quad (3.14)$$

where $\mathcal{K}_b = \{l = 1, \dots, L_s\}$ and $\mathcal{C}_{kb} = \{i = 1, \dots, C_s\}$, with L_s users and C_s clusters active in the b th subarray (SA). p_{ul} is the transmit power, $\mathbf{h}_{li(b)} \in \mathbb{C}^{M_{\text{VR}} \times 1}$ is the channel between the cluster i of the l th UE and the b th subarray in the BS, $\mathbf{N} \in \mathbb{C}^{M_{\text{VR}} \times \tau_p}$ is the receiver noise with i.i.d. elements distributed as $\mathcal{CN}(0, \sigma^2)$, $\boldsymbol{\phi}_l \in \mathbb{C}^{\tau_p \times 1}$ is the pilot assigned to UE i , in which $\|\boldsymbol{\phi}_l\|^2 = \tau_p$.

To estimate the channel from the i th cluster of the l th UE, considering that in the proposed system every user shares the same pilot sequence, the BS first correlates the received signal with the associated pilot signal to obtain:

$$\mathbf{z}_{l(b)} = \mathbf{Y}_{(b)} \boldsymbol{\phi}_l^* = \sum_{l \in \mathcal{K}_b} \sum_{i \in \mathcal{C}_{kb}} \sqrt{p_{ul}} \tau_p \mathbf{h}_{li(b)} + \mathbf{N} \boldsymbol{\phi}_l^* \quad (3.15)$$

Adopting the MMSE channel estimator, the estimated channel is obtained by calculating:

$$\hat{\mathbf{h}}_{li(b)} = \boldsymbol{\Phi}_{li(b)} \mathbf{Q}_{(b)}^{-1} \left(\frac{1}{\tau_p \sqrt{p_{ul}}} \mathbf{z}_{l(b)} \right) \quad (3.16)$$

where $\boldsymbol{\Phi}_{li(b)}$ is the channel correlation matrix related to the b th subarray and channel response $\mathbf{h}_{li(b)}$; moreover, matrix $\mathbf{Q}_{(b)}$ is defined as

$$\mathbf{Q}_{(b)} = \mathbb{E}\{\mathbf{z}_{l(b)} \mathbf{z}_{l(b)}^H\} = \sum_{l \in \mathcal{K}_b} \sum_{i \in \mathcal{C}_{kb}} \boldsymbol{\Phi}_{li(b)} + \frac{\sigma^2}{\tau_p p_{ul}} \mathbf{I}_{M_{\text{VR}}} \quad (3.17)$$

where $(\cdot)^H$ is the Hermitian operator.

Combiner: for detecting the *payload data transmission*, different low-complexity linear combining schemes can be deployed at the massive BS antennas. Starting with the received data signal at the subarray b in the BS:

$$\mathbf{Y}_{(b)}^u = \sum_{l \in \mathcal{K}_b} \sum_{i \in \mathcal{C}_{kb}} \sqrt{p_{ul}} \mathbf{h}_{li(b)} \mathbf{s}_l^T + \mathbf{N}^u \quad (3.18)$$

where $\mathbf{s}_l \in \mathbb{C}^{\tau_u \times 1}$ with τ_u i.i.d. elements distributed as $\mathcal{CN}(0, 1)$ are the data symbols from the l th UE, and $\mathbf{N}^u \in \mathbb{C}^{M_{\text{VR}} \times \tau_u}$ is the receiver noise with i.i.d. elements distributed as $\mathcal{CN}(0, \sigma^2)$.

Thus, the BS selects a combining scheme for each user's active cluster at each subarray, *i.e.*, the combiner vector $\mathbf{v}_{li(b)} \in \mathbb{C}^{M_{\text{VR}} \times 1}$ that uses the channel estimation obtained from the pilot signaling is correlated with the received signal

$\mathbf{Y}_{(b)}^u$ as:

$$\mathbf{v}_{li(b)}^H \mathbf{Y}_{(b)}^u = \underbrace{\mathbf{v}_{li(b)}^H \mathbf{h}_{li(b)} \mathbf{s}_l}_{\text{Desired signal}} + \underbrace{\sum_{l' \in \mathcal{K}_b \setminus l} \sum_{i' \in \mathcal{C}_{l'b}} \mathbf{v}_{l'i'(b)}^H \mathbf{h}_{l'i'(b)} \mathbf{s}_{l'}}_{\text{Interference}} + \underbrace{\mathbf{v}_{li(b)}^H \mathbf{N}^u}_{\text{Noise}} \quad (3.19)$$

generating three terms: desired signal, interference and noise.

3.2.2 Channel Model

In XL-MIMO the number of antennas and the array dimension can be considered extremely large, typically thousands of antennas, while the users distance to the array is very short compared to the array size, *i.e.*, the far-field assumption does not hold. Thus, due to such configuration, spatial non-stationarities arise; as a result, the signal from the user can be observed by different, small disjunct subsets of antennas, called *visibility region* (VR), where these regions generally does not include the *visibility* of the total array of antennas (CHEN et al., 2017). As reported by measurements in (CARVALHO et al., 2020), it is necessary consider the non-stationary from a spatial perspective (OESTGES; CLERCKX, 2007).

Two extreme-large MIMO channel models have been considered in this work: double-scattering XL channel and single-scattering XL channel.

3.2.2.1 Double-scattering Model

In this XL-MIMO channel model, the channel between the k th user and the BS is composed by clusters located at user and BS sides, respectively, as depicted in Fig. 3.4. In such scenario, the user presents a single cluster composed by S linear scatterers, while near to the BS there are C BS-clusters; besides, each BS-cluster contains S_i scatterers.

For the formulation of the XL channel model, in the sequel, the user's communication with the i th XL BS-cluster is modelled such that results in a specific subset of visible antennas at BS:

$$\tilde{\mathbf{h}}_{i,k} = \mathbf{\Upsilon}_i \boldsymbol{\rho}_i^{\frac{1}{2}} \mathbf{R}_i^{\frac{1}{2}} \mathbf{G}_i \tilde{\mathbf{R}}_{i,k}^{\frac{1}{2}} \mathbf{D}_{i,k} \mathbf{g}_k \quad (3.20)$$

where $\mathbf{\Upsilon}_i \in \{0, 1\}^{M \times r_i}$ represents the indices of the visible antennas, $\boldsymbol{\rho}_i \in \mathbb{C}^{r_i}$ is the visibility gain matrix, \mathbf{G}_i is the complex scattering amplitudes, r_i is the number of visible antenna elements in the i th BS-cluster, while $\mathbf{D}_{i,k} = \mathbf{1}^{S_i \times S_k}$ is a matrix of ones with $S_i \times S_k$ dimensions representing the visibility of the k th user regarding the i th BS-cluster, and $\mathbf{g}_k \sim \mathcal{CN}(0, 1) \in \mathbb{C}^{S_k \times 1}$ is the small-scale fading. The matrices $\mathbf{R}_i \in \mathbb{C}^{r_i \times r_i}$ and $\tilde{\mathbf{R}}_{i,k} \in \mathbb{C}^{S_i \times S_i}$ are the correlation matrices on the BS side and the user side, respectively. The \mathbf{R}_i defines the correlation matrix between the signals that arrive at BS, according to physical

parameters, as location of each BS-cluster and the antenna spacing, being modelled as:

$$[\mathbf{R}_i]_{m,l} = \frac{1}{S_i} \sum_{n=\frac{1-S_i}{2}}^{\frac{S_i-1}{2}} e^{-2\pi j(m-l)d_r \cos\left(\frac{\pi}{2} + \varphi_i + \frac{n\vartheta_i}{S_i-1}\right)} \quad (3.21)$$

where (m, l) corresponds to the elements of the correlation matrix, d_r is the λ -normalized antenna spacing at BS, with λ being the carrier wavelength, φ_i is the azimuth angle between the BS and the i th BS-cluster and ϑ_i is the angular spread around to the azimuth angle. For the user side, the correlation matrix is defined as:

$$[\tilde{\mathbf{R}}_{i,k}]_{m,l} = \frac{1}{S_i} \sum_{n=\frac{1-S_i}{2}}^{\frac{S_i-1}{2}} e^{-2\pi j(m-l)d_s \cos\left(\frac{\pi}{2} + \tilde{\varphi}_{i,k} + \frac{n\tilde{\vartheta}_{i,k}}{S_i-1}\right)} \quad (3.22)$$

where d_s is the λ -normalized spacing between the elements of the i th scatterer S_i , while $\tilde{\varphi}_i$ is the azimuth angle between the UE-cluster and the i th BS-cluster correspond to the user k and $\tilde{\vartheta}_i$ is the angular spread around to $\tilde{\varphi}_i$.

The energy distribution ρ inside each cluster is defined as:

$$\rho_i = 10^{-\psi|c_i - d_r(n-1)|} \quad (3.23)$$

where n is the index of the antenna elements inside the cluster VR and ψ is a constant slop that attenuates the channel gain with the distance.

Thus, the k th user channel can be described combining all C clusters for the user k , such as:

$$\mathbf{h}_k = \sum_{i \in \mathcal{C}_k} \tilde{\mathbf{h}}_{i,k}, \quad (3.24)$$

where \mathcal{C}_k is the subset of active clusters visible to each user k .

3.2.2.2 Single-scattering Model

Unlike the double-scattering model, the single-scattering is composed by a single cluster between the BS and the UE. Thus the C clusters receive the signal from the UE and each cluster creates a VR at BS. The single-scattering description is a simplified but relatively generic XL model capable of describing and modeling the VRs due to the spatial non-stationarities. In our single-scattering model, the cluster is composed by S_i linear scatterers, being the formulation between the k th UE and the i th cluster given by:

$$\mathbf{h}_{i,k} = \mathbf{Y}_i \rho_i^{\frac{1}{2}} \mathbf{R}_i^{\frac{1}{2}} \bar{\mathbf{g}}_k \quad (3.25)$$

where $\bar{\mathbf{g}}_k \in \mathbb{C}^{r_i \times 1}$ is the small-scale fading, while \mathbf{Y}_i , ρ_i , and \mathbf{R}_i are calculated in the same way as in eq. (3.20).

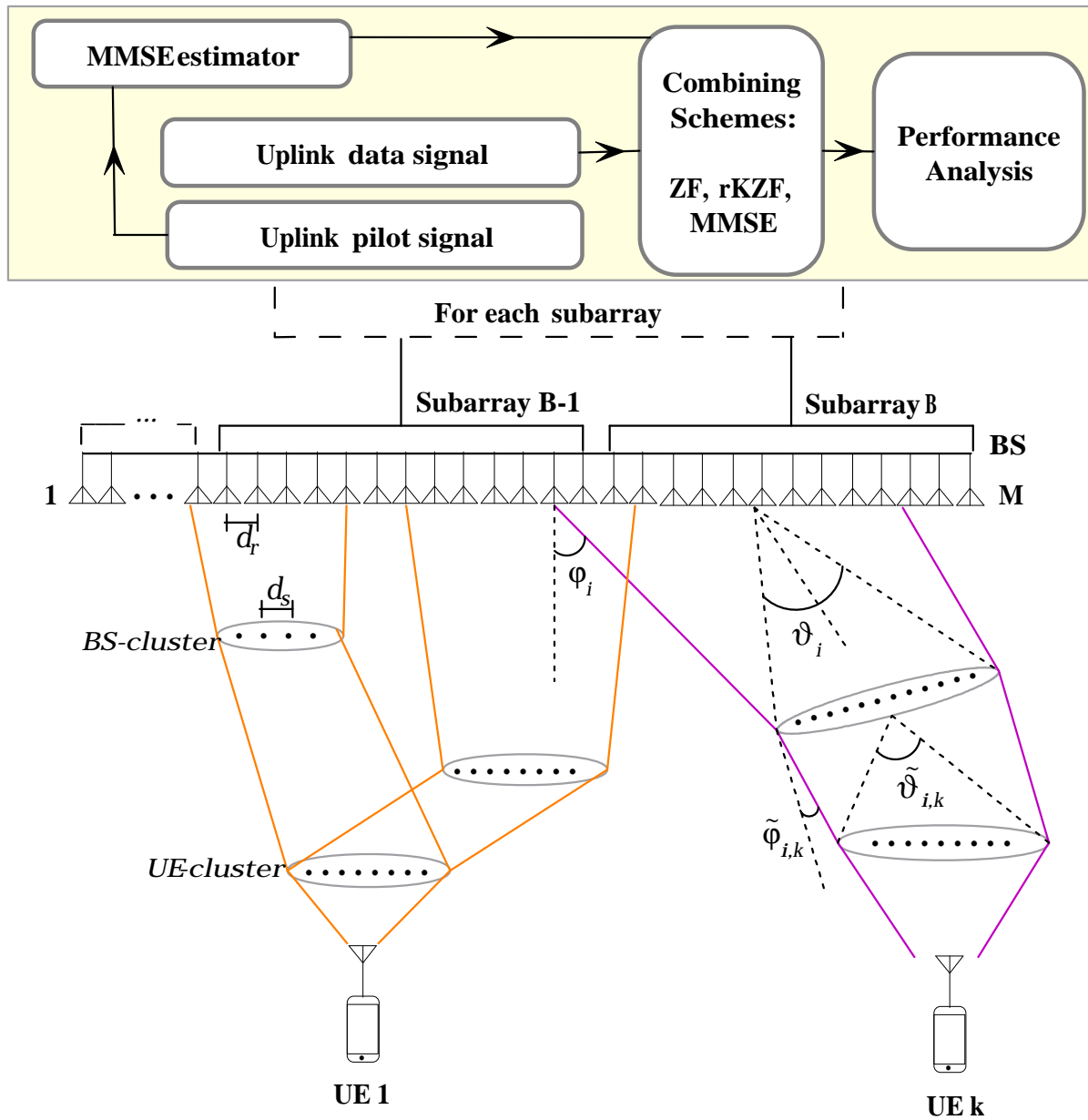


Figure 3.4 – Sketch of the uplink XL-MIMO system: (top) Combiner and channel estimation blocks; (bottom) the double-scattering channel model; (in between) M -antennas linear array with B subarrays. The distance between linear scattering-elements is d_s , while d_r holds for distance between antenna elements at BS.

3.2.3 Processing Each Subarray

As well-known, in typical XL-MIMO scenarios, only some spatial regions of the XL array are visible to the user; hence, we split the large array of antennas into B subarrays with equal number M_b of antennas in each subarray. Hence, each subarray evaluates the received signal, and only the subset of subarrays that accumulate the most part of signal energy (say at least 90%) is selected. Such methodology for subarrays selection was presented in (AMIRI et al., 2018), where the algorithm, called Bipartite graph, determines which part of the matrix the user power is dominant. By using smaller subarrays for the signal processing, including the combiner, one is able to reduce the computational complexity, since a smaller number of antennas equal to M_b is deployed.

Thus, based on the choice of which subarray processes each user's signal, in the sequel we analyze the processing of each subarray separately. We build the combination schemes, using the massive channel estimate in the selected subarray and calculate the performance of each combiner in terms of spectral and energy efficiency of the XL-MIMO system.

Starting from the choice of the subarray for signal processing, the elements of the channel vector and the correlation matrix are defined. For example, if the chosen subarray represents the first 10 antenna elements of the BS, we select the first 10 elements of the channel vector for processing. However, for the correlation matrix, such selection is not straightforward, as its dimension depends on the length of the VR. Thus, we define two situations: *i*) the VR includes the first 10 antenna elements; *ii*) the VR does not includes the first 10 antenna elements. If the VR covers the first 10 elements, such elements are selected from the correlation matrix. However, if the VR partially covers the first 10 antenna elements, then the correlation matrix is completed with zeros to obtain the dimension of the subarray and can perform the signal processing.

3.2.4 Linear Combiners

When a user transmits the signal to the BS, this signal suffers some effects of the channel, resulting in a received signal different from the transmitted signal. Thus, in order to identify the transmitted signal, it is fundamental a combining scheme, where, in this section, we define four combining schemes.

3.2.4.1 Zero-forcing Combiner (ZF) for XL-MIMO

A suboptimal combining is the ZF combiner, defined by the b th SA as:

$$\mathbf{V}_{(b)}^{\text{ZF}} = \widehat{\mathbf{H}}_{(b)}(\widehat{\mathbf{H}}_{(b)}^H \widehat{\mathbf{H}}_{(b)})^{-1} \quad (3.26)$$

where $\widehat{\mathbf{H}}_{(b)}$ is the estimated channel matrix of all clusters of each user of the b th subarray. The focus of the ZF is mitigate the interference of other users, however, the inverse of the

matrix increases the computer complexity. The ZF is more recommended when the SNR is high.

3.2.4.2 Randomized Kaczmarz Regularized Zero-Forcing (rKZF)

The combining presented above are normally evaluated from the exact channel state information (CSI). However, it is a great challenge to estimate perfectly the channel due to the pilot contamination. Therefore, the authors in (BOROUJERDI et al., 2018) propose a novel technique for computing the precoder/detector in a massive MIMO system, considering an imperfect channel estimation. The technique is based on the iterative Kaczmarz algorithm, where it was proposed initially for solving consistent over-determined (OD) set of linear equations (SLE). However, in (BOROUJERDI et al., 2018) was extended this algorithm to the under-determined (UD) SLE, allowing the application of the algorithm to M-MIMO. Initially, we present the regularized KA represented to the RZF combining and then we described the randomized iterative KA algorithm.

rKZF Combiner for XL-MIMO: Considering the UL mode, the received signal is estimated as:

$$\hat{\mathbf{s}} = \mathbf{V}^H \mathbf{y} \quad (3.27)$$

where \mathbf{V} is the combining scheme and $\hat{\mathbf{s}} \in \mathbb{C}^K$ is the estimate vector of the transmitted symbols from each UE.

Defining the combining scheme as the regularized ZF (RZF), given by:

$$\mathbf{V}_{(b)}^{\text{RZF}} = (\widehat{\mathbf{H}}_{(b)}^H \widehat{\mathbf{H}}_{(b)} + \xi \mathbf{I}_K)^{-1} \widehat{\mathbf{H}}_{(b)}^H \quad (3.28)$$

the estimate signal is:

$$\hat{\mathbf{s}} = (\widehat{\mathbf{H}}_{(b)}^H \widehat{\mathbf{H}}_{(b)} + \xi \mathbf{I}_K)^{-1} \widehat{\mathbf{H}}_{(b)}^H \mathbf{y} \quad (3.29)$$

The signal estimation $\hat{\mathbf{s}}$ can be deduced as the optimum solution to the problem (BOROUJERDI et al., 2018; RODRIGUES et al., 2019):

$$\arg \min_{\mathbf{w} \in \mathbb{C}^K} \|\widehat{\mathbf{H}}_{(b)} \mathbf{w} - \mathbf{y}\|^2 + \xi \|\mathbf{w}\|^2 \quad (3.30)$$

where we can rewritten compactly the cost function above as $\|\mathbf{B}\mathbf{w} - \mathbf{y}_0\|_2^2$, in which $\mathbf{B} = [\widehat{\mathbf{H}}_{(b)}; \sqrt{\xi} \mathbf{I}_K]$ is a $(M + K) \times K$ matrix and $\mathbf{y}_0 = [\mathbf{y}; \mathbf{0}]$ is a $(M + K) \times 1$ vector. An alternative to solve the compact optimization problem is $\mathbf{B}\mathbf{w} = \mathbf{y}_0$. The SLE is an overdetermined (OD) systems of equations, i.e., there are more equations than unknown variables; however, there is a inconsistency in the set equations due to the presence of the noise on the received signal \mathbf{y} . In (BOROUJERDI et al., 2018), the inconsistency was removed by split the SLE in two steps.

Initially, we define a variable $\hat{\mathbf{y}}_0 \in \mathbb{C}^{(M+K)}$ as:

$$\hat{\mathbf{y}}_0 = \mathbf{B}\hat{\mathbf{s}} = \mathbf{B}(\mathbf{B}^H \mathbf{B})^{-1} \widehat{\mathbf{H}}_{(b)}^H \mathbf{y} \quad (3.31)$$

where we can manipulate the equation by:

$$\mathbf{B}^H \widehat{\mathbf{y}}_0 = (\mathbf{B}^H \mathbf{B})(\mathbf{B}^H \mathbf{B})^{-1} \widehat{\mathbf{H}}_{(b)}^H \mathbf{y} = \widehat{\mathbf{H}}_{(b)}^H \mathbf{y} \quad (3.32)$$

Let \mathbf{z}^t the estimation of $\widehat{\mathbf{y}}_0$ at iteration t , the UD SLE above is consistent if \mathbf{z}^0 starts from the zero initialization $\mathbf{z}^0 = 0$ (BOROUJERDI et al., 2018). Thus, the UD SLE is consistent, because the estimate \mathbf{z}^t lies in the subspace generated by the columns of \mathbf{B} . Lastly, the estimate signal $\widehat{\mathbf{s}}$ can be found by solve the consistent OD SLE:

$$\mathbf{B} \widehat{\mathbf{s}} = \widehat{\mathbf{y}}_0 \quad (3.33)$$

However, a direct way to estimate $\widehat{\mathbf{s}}$ is through of the K last rows of $\widehat{\mathbf{y}}_0$, dividing by $\sqrt{\xi}$. Thus, only the eq. (3.32) need to be solved by the rKA algorithm.

rKA: the Kaczmarz algorithm was described to solve equations in the form $\mathbf{A}\mathbf{w} = \mathbf{b}$. From an iterative way, the KA algorithm updates the \mathbf{w} in order to make equality close to the true value. At each iteration t , KA finds the closest vector \mathbf{w}^t and also approximates to $\langle \mathbf{a}_{r(t)}, \mathbf{w} \rangle = b_{r(t)}$, using the follow equation:

$$\mathbf{w}^{t+1} = \mathbf{w}^t + \frac{b_{r(t)} - \langle \mathbf{a}_{r(t)}, \mathbf{w}^t \rangle}{\|\mathbf{a}_{r(t)}\|^2} \mathbf{a}_{r(t)} \quad (3.34)$$

where $\mathbf{a}_{r(t)}$ is the r th row of \mathbf{A} , $b_{r(t)}$ is the r th element of \mathbf{b} and each row $r(t)$ is selected randomly with the probability $\frac{\|\mathbf{a}_{r(t)}\|_2^2}{\|\mathbf{A}\|_F^2}$.

As viewed before, to estimate the signal $\widehat{\mathbf{s}}$, we need to solve the eq. (3.32). Thus, we assume $\mathbf{b} = \widehat{\mathbf{H}}_{(b)}^H \mathbf{y}$ and we rewrote the eq. (3.34) as:

$$\mathbf{z}^{t+1} = \mathbf{z}^t + \underbrace{\frac{b_{r(t)} - \langle \mathbf{B}_{r(t)}, \mathbf{z}^t \rangle}{\|\mathbf{B}_{r(t)}\|^2}}_{\eta^t} \mathbf{B}_{r(t)} \quad (3.35)$$

where η is called as the residual term and the $r(t)$ row is selected randomly with the probability of:

$$\frac{\|\mathbf{B}_{r(t)}\|_2^2}{\|\mathbf{B}\|_F^2} = \frac{\|\widehat{\mathbf{H}}_{(b),r(t)}\|_2^2 + \xi}{\|\widehat{\mathbf{H}}_{(b)}\|_F^2 + K\xi} \quad (3.36)$$

As the K last rows contains the estimate signal, we can separate the \mathbf{z}^t as two vectors $\mathbf{u} \in \mathbb{C}^{M \times 1}$ and $\sqrt{\xi} \mathbf{v} \in \mathbb{C}^{K \times 1}$, where \mathbf{v} contains the estimate signal in each iteration t . Thus, by separate the vector \mathbf{z} , the residual term η can be rewritten as:

$$\eta^t = \frac{b_{r(t)} - \langle \widehat{\mathbf{H}}_{(b),r(t)}, \mathbf{u}^t \rangle - \xi \mathbf{v}_{r(t)}^t}{\|\widehat{\mathbf{H}}_{(b),r(t)}\|^2 + \xi} \quad (3.37)$$

where the vector \mathbf{u} and the r th element of \mathbf{v} are update by iteration, respectively, as:

$$\mathbf{u}^{t+1} = \mathbf{u}^t + \eta^t \widehat{\mathbf{H}}_{(b),r(t)} \quad (3.38)$$

$$\mathbf{v}_{r(t)}^{t+1} = \mathbf{v}_{r(t)}^t + \eta^t, \text{ and } \mathbf{v}_j^{t+1} = \mathbf{v}_j^t \text{ for } j \neq r(t) \quad (3.39)$$

Algorithm 2 presents the rKA for estimate signal using the RZF combining.

Algorithm 2 rKA Signal Estimation

- 1: **Input** $\widehat{\mathbf{H}}_{(b)}, \xi, T_{\text{rKA}}$
 - 2: Define $\mathbf{u}^0 = \mathbf{0}$ and $\mathbf{v}^0 = \mathbf{0}$
 - 3: **for** $t = 0 : T_{\text{rKA}} - 1$ **do**
 - 4: Pick a row $r(t)$ of $\widehat{\mathbf{H}}_{(b)}$ with probability described in (3.36)
 - 5: Compute the residual term η as in (3.37)
 - 6: Update \mathbf{u} as in (3.38)
 - 7: Update \mathbf{v} as in (3.39)
 - 8: **end for**
 - 9: **Output** $\widehat{\mathbf{s}} = \mathbf{v}^{T-1}$
-

Unlike Algorithm 2, in (RODRIGUES et al., 2019) it was studied a rKA version, in which the combining matrix is estimated instead of the data signal. Hence, in such rKA version, it were introduced a canonical basis vector $\mathbf{e}_k \in \mathbb{C}^K$, a vector $\mathbf{c}^t \in \mathbb{C}^{(M+K)} = [\mathbf{u}^t \mathbf{z}^t]$ and a matrix $\mathbf{D}^{\text{rKA}} \in \mathbb{C}^{K \times K}$. The elements of the canonical basis vector \mathbf{e}_k can assume two values: 1 or 0, where the k th element is 1 and otherwise is 0. Basically, the combining vector is obtained as $\mathbf{v}_k = \widehat{\mathbf{H}}_{(b)} \mathbf{d}_k$, where \mathbf{d}_k is the k th row of \mathbf{D}^{rKA} . The Algorithm 3 describes the rKA to estimate the RZF receive combining matrix.

Algorithm 3 rKZF Combiner for M-MIMO (RODRIGUES et al., 2019)

- 1: **Input** $\widehat{\mathbf{H}}_{(b)}, \xi, T_{\text{rKA}}$
 - 2: Define $\mathbf{D}^{\text{rKA}} = \mathbf{0}_{K \times K}$
 - 3: **for** $k = 1 : K$ **do**
 - 4: Define $\mathbf{u}^0 = \mathbf{0}_M$ and $\mathbf{z}^0 = \mathbf{0}_K$
 - 5: Compute the \mathbf{e}_k
 - 6: **for** $t = 0 : T_{\text{rKA}} - 1$ **do**
 - 7: **if** $t=0$ **then**
 - 8: Pick a k th row of $\widehat{\mathbf{H}}_{(b)}$
 - 9: **else**
 - 10: Pick a row $r(t)$ of $\widehat{\mathbf{H}}_{(b)}$ with probability (3.36)
 - 11: **end if**
 - 12: Compute residue $\eta^t = \frac{[\mathbf{e}_k]_{r(t)} - \langle \widehat{\mathbf{H}}_{r(t)}, \mathbf{u}^t \rangle - \xi z_{r(t)}^t}{\|\widehat{\mathbf{H}}_{r(t)}\|^2 + \xi}$
 - 13: Update $\mathbf{u}^{t+1} = \mathbf{u}^t + \eta^t \widehat{\mathbf{H}}_{(b), r(t)}$
 - 14: Update $z_{r(t)}^{t+1} = z_{r(t)}^t + \eta^t$
 - 15: **end for**
 - 16: Update $[\mathbf{D}^{\text{rKA}}]_{:,k} = \mathbf{z}^{T_{\text{rKA}}-1}$
 - 17: **end for**
 - 18: **Output** $\mathbf{V}^{\text{rKA}} = \widehat{\mathbf{H}}_{(b)} \mathbf{D}^{\text{rKA}}$
-

3.2.4.3 MMSE Combiner for XL-MIMO

A linear MMSE-based combining scheme for massive MIMO systems is presented in (BJÖRNSON et al., 2018). The M-MMSE combining maximizes the SINR by amplifying the desired signal and, in the case of M-MIMO systems, suppressing both intracellular and intercellular interference. The analysis indicate an unlimited spectral efficiency even with the presence of pilot contamination; however, it is showed that to mitigate the pilot contamination, the *covariance matrices of the users that share the same pilot sequence have to be asymptotically linearly independent, i.e.*, from the theoretical analysis, the channel model hypotheses and implications affect the M-MIMO system performance in terms of SE.

Elaborating further, and adapting to the extra-large scale MIMO systems scenarios, indeed, in a XL-MIMO system, the theory behind the multicell channels is not suitable, because the context requires the large-antennas arrays deployment in environments where there are a lot of users clustered, i.e., single-cell crowd scenarios, as in stadium and huge open space environments. As well-known, the number of pilot sequences simultaneously available is limited, while the number of active UEs is large; as a result, in some practical XL-MIMO scenarios, pilot contamination effect is unavoidable.

Based on (BJÖRNSON et al., 2018; BJÖRNSON; SANGUINETTI, 2020), a MMSE combining scheme for XL-MIMO system can be conceived, in which the spatial region with K active users communicating with a BS equipped with an extreme-large antenna array, while the number of available pilot sequences is insufficient, resulting in the reuse of the pilot sequences.

In the XL-MIMO context, the MMSE combiner scheme can be performed as (3.40), in which the MMSE combiner is defined by (SANGUINETTI et al., 2020).

$$\mathbf{V}_{(b)}^{\text{MMSE}} = \left(\widehat{\mathbf{H}}_{(b)} (\widehat{\mathbf{H}}_{(b)})^H + \mathbf{Z}_{li} \right)^{-1} \widehat{\mathbf{H}}_{(b)} \quad (3.40)$$

where $\mathbf{Z}_{l,i}$ in each subarray is defined as:

$$\mathbf{Z}_{(b)} = \sum_{l \in \mathcal{K}_b} \sum_{i \in \mathcal{C}_{kb}} (\Phi_{li} - \Phi_{li} \mathbf{Q}_{li}^{-1} \Phi_{li}) + \frac{\sigma^2}{p_{ul}} \mathbf{I}_{M_{\text{VR}}} \quad (3.41)$$

where $\Phi_{li} \in \mathbb{C}^{M_{\text{VR}} \times M_{\text{VR}}}$ is the correlation matrix of the i th user channel.

3.2.5 Numerical Results

In this section, extensive numerical results for the MSE, variance of XL-channel interference, SE, and EE are provided based on the performance metrics explored in Section ???. The main adopted XL-MIMO system and channel parameters are listed in Table 3.2 for MSE analysis, Table 3.3 for the SE evaluation, and Table 3.4 for $\text{EE} \times \text{SE}$ analysis.

Table 3.2 – Parameters values adopted for MSE evaluation.

Parameters	Values
System	
# antennas at the BS	$M = 256$
# UEs	$K = [16, 32, 64]$
Loading system	$\mathcal{L} = \frac{K}{M} \in [6.2; 12.5; 25.0] [\%]$
SNR	5 dB
Estimation quality	Perfect CSI
# Monte Carlo realizations	1000
Randomized Kaczmarz Algorithm	
# iteration	$T_{\text{rKZF}} = [20 : 300]$
RZF regularization factor	$\xi = 1/\text{SNR}$
Single scattering model	
# clusters	$C = 5$
Antenna spacing	$d_r = 0.0578$ m
Angular spread	$\vartheta = 3\pi/4$ rad
Azimuth angle	$\alpha_i \in \mathcal{U}(-\pi/2, \pi/2)$ rad
# scatterers	$S_i = 10$
Array length	$L = (M - 1)d_r$
VR center	$c_i \sim \mathcal{U}(0, L)$
VR size	$l_i \sim \mathcal{LN}(0.7, 0.2)$
Double scattering model	
# clusters	$C = 5$
Scatterer spacing	$d_s = 5$ m
Antenna spacing	$d_r = 0.0578$ m
Angular spread BS / UE	$\vartheta_i = 3\pi/4$ and $\tilde{\vartheta}_{i,k} = 7\pi/8$ rad
Azimuth angle BS / UE	$\alpha_i, \tilde{\alpha}_{i,k} \in \mathcal{U}(-\pi/2, \pi/2)$
# scatterers (BS-cluster)	$S_i = 10$
# scatterers (UE-cluster)	$S_k = 5$
Array length	$L = (M - 1)d_r$
VR center	$c_i \sim \mathcal{U}(0, L)$
VR size	$l_i \sim \mathcal{LN}(0.7, 0.2)$

3.2.5.1 Mean Squared Error of XL-MIMO Channel Estimates

We evaluate the MSE performance for the RKZF combiner when compared to the traditional RZF. From the parameters described in Table 3.2, the MSE according to the number of iterations is presented in Fig. 3.5. In this analysis, we consider three channel models: uncorrelated, single-scattering and double-scattering. In all cases, the reduction in the number of users is beneficial for the convergence of the algorithm. Notice that the loading system $\mathcal{L} = \frac{K}{M}$ influences the convergence of the algorithm, presenting an exponential convergence time with increasing loading (ROSA et al., 2019). Moreover, Fig. 3.5 also reveals that the channel correlation influences the approximation given by the rKA algorithm. For a uncorrelated channels (unc), the obtained MSE is lower in all cases when compared to the correlated channel estimates. Among the correlated channel

models, the single-scattering model presents a higher error estimates when the number of iterations is small; however, it tends to smaller errors than the double-scattering model when the number of iterations increases. Thus, it is seen that the rKA algorithm presents a slow-convergence in terms of MSE of channel estimates when the double model is used, even if considering different loading systems $\mathcal{L} \in [6.2; 12.5; 25.0]\%$.

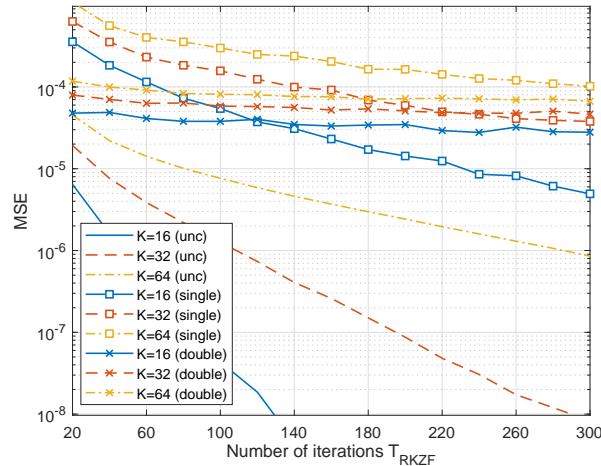
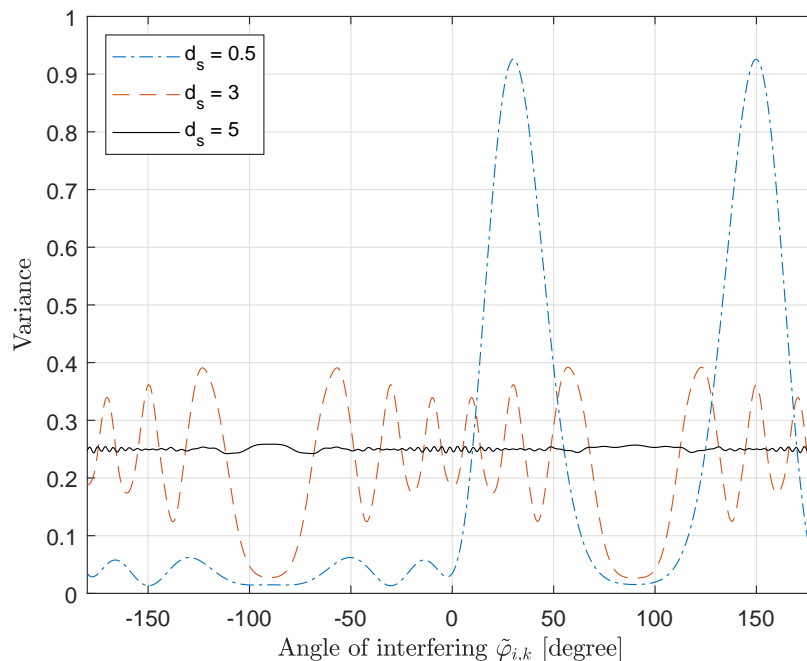


Figure 3.5 – MSE \times Iterations for the rKA-emulating the RZF combiner, $K \in [16, 32, 64]$ users.

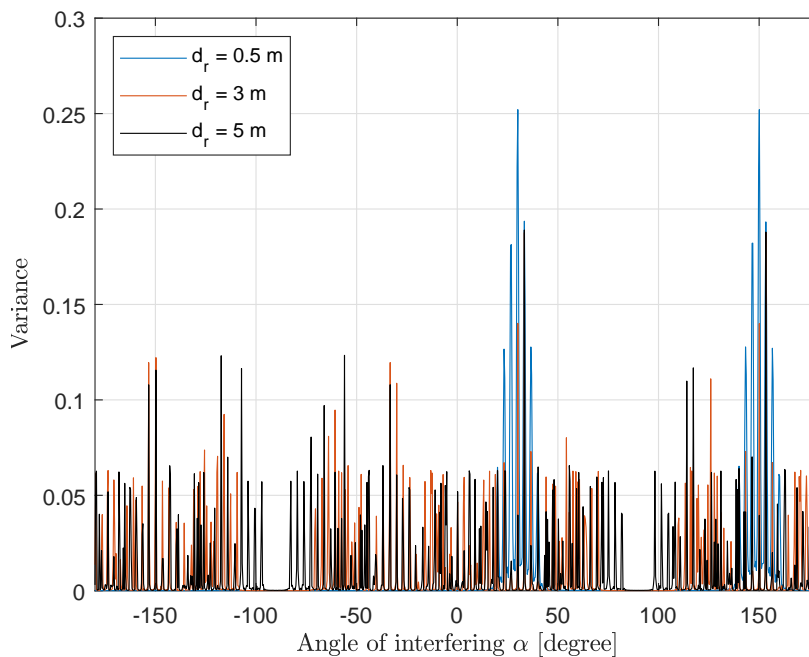
3.2.5.2 Favourable Propagation in XL-MIMO

We evaluate the interference between users at the BS massive antenna array using eq. (3.15). We consider two users, where the first one has a fixed location while the location of the second user varies angularly. Also, we consider that there is only one BS-cluster, being shared among users. Using eq. (3.15), the interference obtained are presented in Fig. 3.6.a) for double-scattering model, and Fig. 3.6.b) for single-scattering channel model, both evaluations with 2 users. For the analysis of model a), we fixed the user with the angle $\tilde{\varphi}_{i,k}$ of 30° and we varied the second user by $[-180^\circ, 180^\circ]$. In Fig. 3.6.a), we evaluate how the spacing between the scatterers influences the variance, using three cases: $d_s = [0.5, 3, 5]$ m. We observe higher and lower values of variance when the spacing decreases, where $d_s = 5m$ the variance is $\varsigma_{\ell,k} \approx 0.25$ across the angular range. In addition, we observed that at $d_s = 0.5m$ the highest interference values occur when the interfering angle is equal to 30° or 150° . With higher values of d_s , the correlation between scatterers decreases, and with $d_s = 5m$, the massive channels are approximately uncorrelated from the interfering angle (full favourable propagation condition). However, when the linear scatterers spacing decreases and both users have the near or same angular location, or even if the interfering user is close to the mirror reflection angle $180^\circ - 30^\circ = 150^\circ$, one can observe a very high variance of $\varsigma_{\ell,k} > 0.9$, due to the similarity between the users' correlation matrices. However, when the distance between linear scatterers is reduced, *i.e.*, $d_s < 0.5$, and users are well-separated angularly (spatially localization), one can observe that the channels

present near orthogonality, resulting in much less interference $\varsigma_{\ell,k}$ than in other cases. Similar conclusions can be obtained for the single-scattering model in Fig. 3.6.b).



a) Double-scattering model; 2-users.



b) Single-scattering model; 2-users.

Figure 3.6 – Interference analysis between two users, considering the a) double-scattering b) single-scattering model.

3.2.5.3 Spectral Efficiency in XL-MIMO Single-scattering Model

In this section, we evaluate the SE according to the SNR and the VR length. For the first simulation, we considered the behavior of SE vs SNR for different numbers of

clusters, in which the adopted parameter values are described in Table 3.3.

Table 3.3 – Parameters values adopted for SE \times SNR evaluation.

Parameters	Values
System	
BS antennas	$M = 256$
UEs	$K = 2$
Number of subarrays	$B = 4$
Number of antennas per subarray	$M_b = 64$
SNR _{dB}	$[-10 : 10 : 60]$ dB
SNR	$10^{\text{SNR}_{dB}/10}$
Power noise	$\sigma^2 = 0.05$ W
Power signal	$p_{ul} = \sigma^2 \text{SNR}$
Channel Estimator	MMSE
Length pilot sequence	$\tau_p = 1$ symbol
Length coherence block	$\tau_c = 200$ symbols
Monte Carlo realizations	2000
Single scattering model	
Number of clusters	$C = [1, 8, 12, 16]$
Wavelength	$\lambda = 0.125$ m
Antenna spacing	$d_r = 0.5\lambda$
Angular spread	$\vartheta = [3\pi/4]$ rad
Azimuth angle	$\varphi_i \in \mathcal{U}(-\pi/2, \pi/2)$ rad
Number of scatterers	$S_i = 5$
Array length	$L = (M - 1)d_r$
VR center	$c_i = a_1(L/M) + (l_i/2)$
VR size	$l_i = 0.9$ m (16 antennas)
Constant slop	$\psi = 0.21$ dB/m

Let's consider two users sharing the same pilot sequence and with the same cluster number. Thus, it was defined that each cluster generates the same length of VR and each VR is positioned as depicted in Fig. 3.7. Thus, the signal from the first user is observed by the first (left) antennas and the increase in the number of clusters implies a VR adjacent to the previous cluster. Similarly, we have that the last (right) antennas get visible the signal of the second user and the increase in the number of clusters represents a visualization of the array from the last to the first antennas. Note that the VRs of the same user do not result in overlapping; however, VRs of different users may overlap with the increase in the number of clusters.

The three combiners are evaluated, considering different numbers of clusters per user. To generate each VR as sketched in Fig. 3.7, we define the center and length of the VR given by c_i and l_i , respectively. The VR center is calculated as $c_i = a_1(L/M) + (l_i/2)$, where a_1 is the first antenna element inside the i th cluster VR. Thus, the interference between users occurs only with $C = 12$ and $C = 16$, and with $C = 8$, the signal of UE 1 is observed by the first half of the array while the signal of UE 2 is observed by the last half

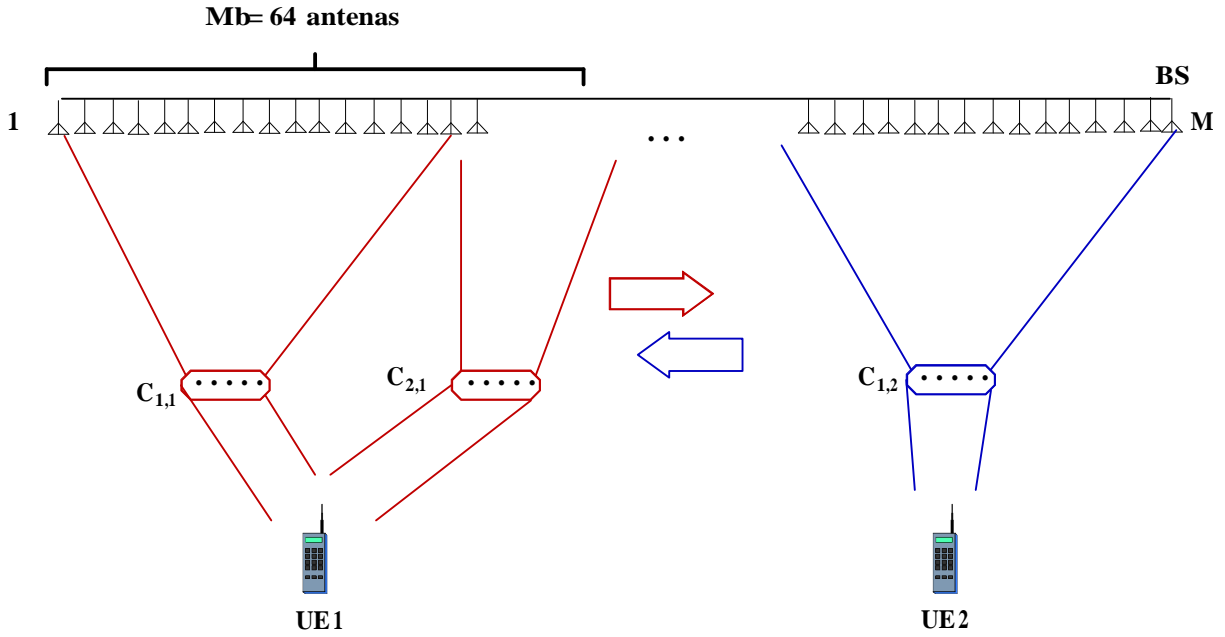


Figure 3.7 – Sketch of the scenario for the SE versus SNR analysis.

of the array. In all configurations, the MMSE performed better than the ZF, as revealed in fig. 3.8. Indeed, it is observed that the increase from 1 to 8 clusters increased the SE performance substantially, attaining a huge SE gap of ≈ 37 bit/s/Hz at SNR=60dB with the MMSE w.r.t. the ZF combiner. In these two initial configurations ($C = 1$ and 8), one can observe that increasing the number of clusters without interference between the UEs, it can improve the SE, since a greater number of antennas improve the diversity gain. However, when interference appears (when $C > 8$), in Fig. 3.8.c) and 3.8.d), SE performance decreases, because the increase in overlapping VRs results in an increase in the level of interference. Thus, considering the all clusters configurations of Fig. 3.8, for the worst case of interference, $C = 16$ (all signals from all clusters receive interference), the SE performance is reduced below than for $C = 1$, where fewer antennas receive the UE signal, but without interference.

SE \times VR size: The SE is analyzed according to the number of visible antennas, using the VR length as metric. In this scenario, the *VR length effect* is evaluated, for two users with the second user with different θ . Fig. 3.9 depicts the SE against VR length, for the RKZF, ZF and MMSE combiners operating under two VR profiles, ρ uniform and triangular, and $\theta = 5^\circ$ or 135° . The case of full VR size, i.e. $M_{\text{VR}} = M$ (massive MIMO configuration) is plotted for reference. In both cases, i.e., $M_{\text{VR}} < M$ and $M_{\text{VR}} = M$, the MMSE combiner resulted in higher SE performance, $\forall M$, compared to the ZF and rKZF combiners. In fact, such behavior is observed due to the possibility of MMSE to better mitigate the inter-user interference, specially increasing when $\theta \rightarrow 0$. We also observed that the increase in the number of clusters results in a reduction in SE. As the system performance was performed individually for each cluster, it was considered that the signal from the same

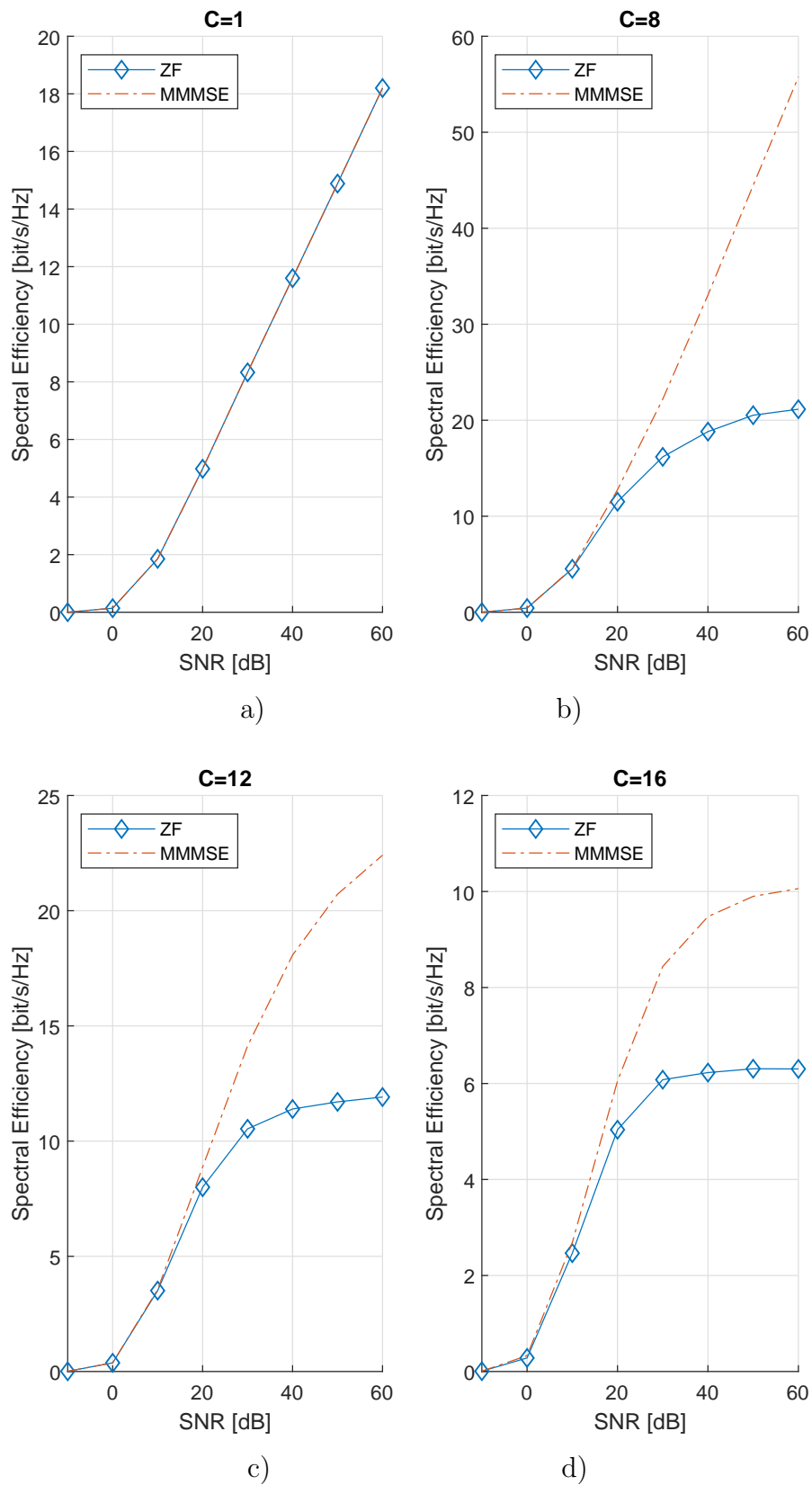


Figure 3.8 – SE vs SNR, considering the ZF and MMSE combiner, where $C = [1; 8; 12; 16]$ clusters, $M = 256$ antennas.

user, but propagated by different clusters, is seen as interference between them. Thus, the reduction in SE is due to the increase in interference associated with the number of clusters. Despite of that, the SE with MMSE tendency increases unlimitedly with M , while the SE obtained with the ZF and rKZF combiners saturates with M , specially under higher levels of interference (when $\theta \rightarrow 0$, in the analysed 2-user scenario), corroborating the fact that under certain system and channel conditions the MMSE combiner is able to completely mitigate the pilot contamination in asymptotic regime ($M \rightarrow \infty$).

3.2.5.4 Energy Efficiency in XL-MIMO with Linear Combiners

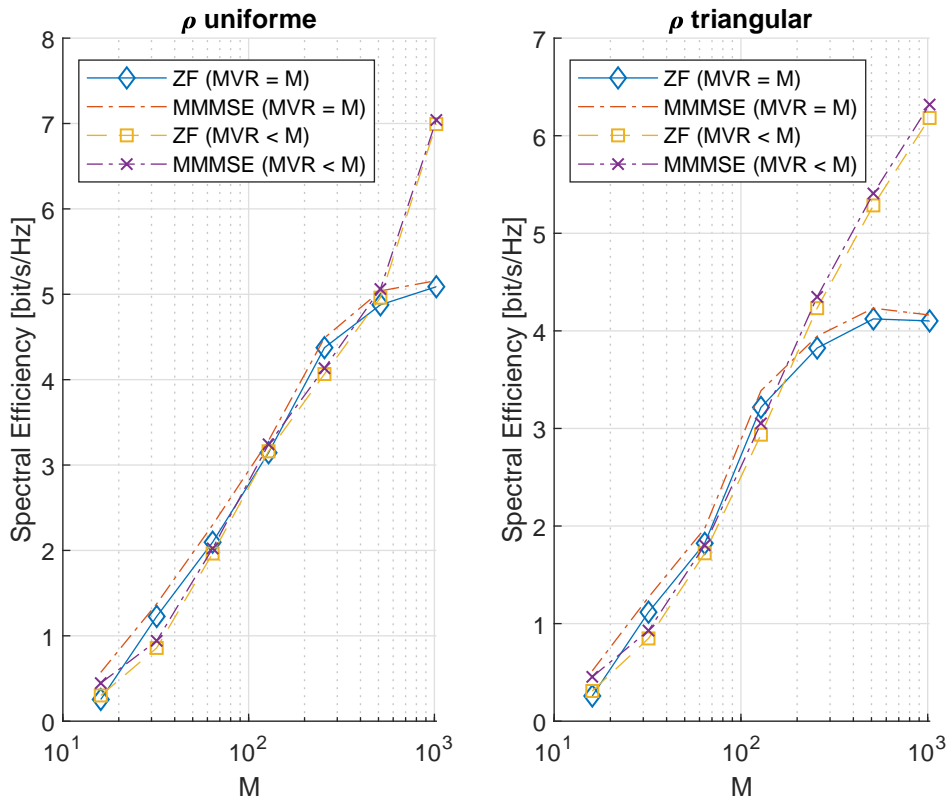
For single-scattering channel model, we evaluate the EE against the number of BS antennas, according to the VR length. Table 3.4 summarizes the parameters values adopted for the EE analysis carried out in this subsection. Fig. 3.10 confirms the best EE value attained with the MMSE combiner for both scenarios: a) massive MIMO condition, when all BS antennas are visible ($M_{\text{VR}} = M$), and b) XL-MIMO with spatial non-stationarities, *i.e.*, when $M_{\text{VR}} < M$. Besides, the MMSE attains higher EE values with less M antenna, *i.e.*, for the power consumption model and values of Table 3.4, the maximum EE achieved with MMSE occurs for $M = 128$ (M-MIMO scenario), and $M = 64$ (XL-MIMO). With the ZF and rKZF combiners, the EE values results reduced and requires more massive antennas M to achieve the maximum EE condition.

3.3 Conclusions

In this section, we present the main conclusion on estimation and detection process for the M-MIMO and XL-MIMO systems. From the MMSE estimation, we analyzed the MRC, ZF, M-MMSE and RZF (emulated by rKA) combiners. For the M-MIMO system, we use the exponential channel model, in which we evaluate the SE according to the number of antennas and the SNR. In this analysis, we observed that the M-MMSE combiner can present a significant SE gain in both analysis, even with the presence of pilot contamination. However, in addition to the use of the MMSE estimator and the M-MMSE combiner, the channel of users who share the same pilot sequence must be asymptotically linearly independent for this behavior to be observed. Thus, the correlation, usually present between the channels, becomes an advantageous condition for signal detection. From this investigation, we developed the analysis for XL-MIMO systems. In this system, there are some differences regarding the channel model and signal processing, where the corresponded modeling is presented. Thus, we analyze the SE according to the number of clusters, resulting in different interference levels. We observed that the increase in the level of interference is harmful to SE, where the power profile adopted influences the level of interference. For EE, we observed that the MMSE performs poorly with the increase in the number of antennas. Comparing ZF and RKZF, the RKZF combiner showed better

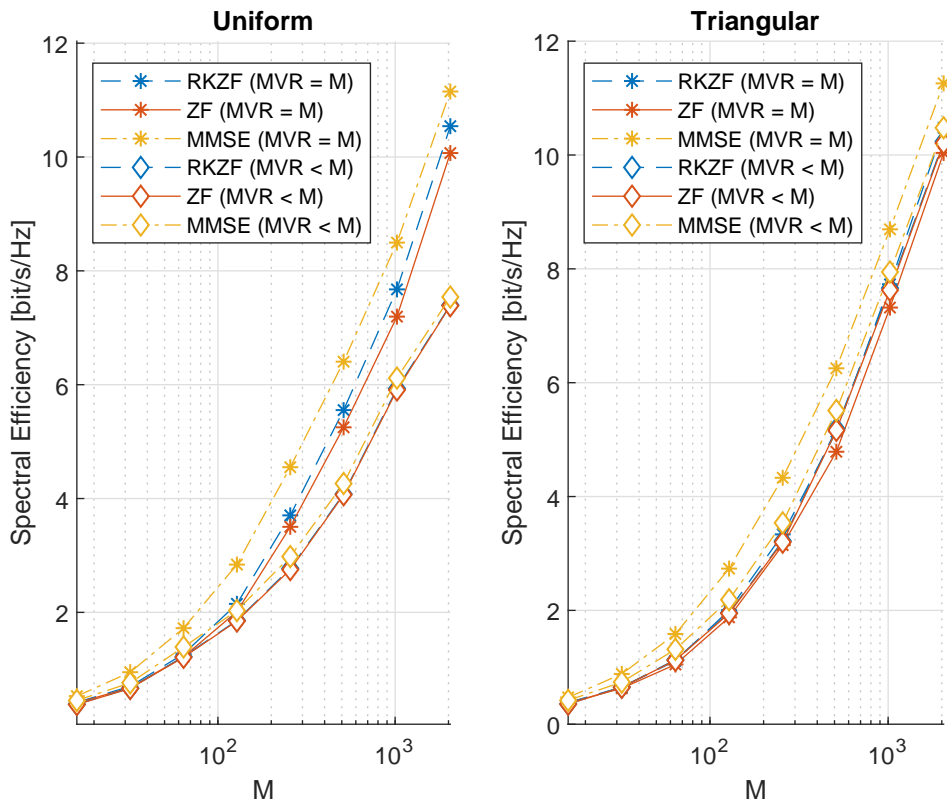
Table 3.4 – Parameters values adopted for EE, SE $\times M$ analysis.

Parameters	Values
System	
BS antennas	$M = [16 \ 32 \ 64 \ 128 \dots \dots 256 \ 512 \ 1024]$
UEs	$K = 2$
subarrays	$B = 4$
antennas per subarray	$M_b = 64$
SNR	10dB
Power noise	$\sigma^2 = 0.05 \text{ W}$
Power signal	$p_{ul} = 0.5 \text{ W}$
Channel Estimator	MMSE
Length pilot sequence	$\tau_p = 1 \text{ symbol}$
Length coherence block	$\tau_c = 200 \text{ symbols}$
Transmission bandwidth	$B_T = 20 \text{ MHz}$
Power amplifier efficiency at the BS	$\kappa^{UL} = 0.5$
Computational efficiency at the BS	$\mathcal{L}_{BS} = 75 \left[\frac{\text{Gflop/s}}{\text{W}} \right]$
Fixed power consumption	$P_{\text{FIX}} = 10 \text{ W}$
Power by local oscillators at BS	$P_{\text{LO}} = 1 \text{ W}$
Power by circuit components at BS	$P_{\text{BS}} = 0.5 \text{ W}$
Power by circuit components at UE	$P_{\text{UE}} = 0.2 \text{ W}$
Power density coding of data signals	$\mathcal{P}_{\text{COD}} = 0.1 \left[\frac{\text{W}}{\text{Gb/s}} \right]$
Power density decoding data signals	$\mathcal{P}_{\text{DEC}} = 0.8 \left[\frac{\text{W}}{\text{Gb/s}} \right]$
Power density for backhaul traffic	$\mathcal{P}_{\text{BT}} = 0.25 \left[\frac{\text{W}}{\text{G/s}} \right]$
Monte Carlo realizations	2000
Randomized Kaczmarz Algorithm	
Number of iteration	$T_{\text{RKZF}} = 20 \text{ iterations}$
RZF regularization factor	$\xi = 1/\text{SNR}$
Single scattering model	
Number of clusters	$C = [1, 4]$
Antenna spacing	$d_r = 0.5\lambda$
Angular spread	$\vartheta = 3\pi/4 \text{ rad}$
Azimuth angle	$\varphi_i \in \mathcal{U}(-\pi/2, \pi/2) \text{ rad}$
Number of scatterers	$S_i = 5$
Array length	$L = (M - 1)d_r$
VR center	$c_i = a_1(L/M) + (l_i/2)$
VR size	$l_i = (MVR - 1)d_r$
Constant slop	$\psi = 0.21 \text{ dB/m}$



a) ρ : Uniform; $\theta = 5^\circ$

b) ρ : Triangular; $\theta = 5^\circ$.



c) ρ : Uniform; $\theta = 135^\circ$

d) ρ : Triangular; $\theta = 135^\circ$.

Figure 3.9 – SE \times VR length, for the RKZF, ZF and MMSE combiners and different VR profiles and θ .

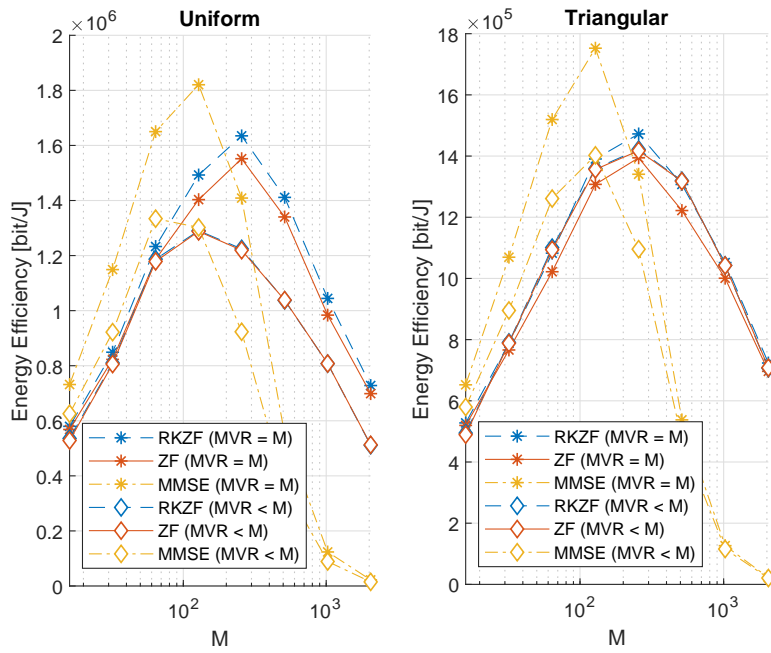


Figure 3.10 – EE vs VR length, considering the RKZF, ZF and MMSE combiner ($\theta = 5^\circ$).

performances, mainly, at its maximum point. In addition, the performance in the rKA algorithm was analyzed when emulating the RZF combiner in different channel models. We observed that the algorithm can achieve small errors according to the number of iterations. Thus, the algorithm makes it possible to weigh the performance and complexity of the combiner.

4 Conclusions and Future Directions

In this Dissertation, we initially carried out a study on channel models for massive and extra-large MIMO systems, analyzing and comparing two stochastic channel models: the GBSM and CBSM. The GBSM model for characterizing the environment from information such as the distribution of clusters, AoA, and Δ , was considered as a more realistic channel model when compared to CBSM. In the numerical results, the analysis of the channel models was performed and corroborated for M-MIMO and XL-MIMO systems.

In the second study carried out along this Dissertation work, linear combining schemes for or XL-MIMO systems, including MMSE and rKA emulating ZF and RZF, were evaluated in terms of spectral efficiency (SE) and energy efficiency (EE) metrics. Hence, using a realistic scenario defined by two correlated channel models called single and double-scattering, as well as including pilot contamination effect, the combiners for XL-MIMO are evaluated. With analysis of SE according to the number of antennas and SNR, we observe that the MMSE present the better SE performance. However, regarding energy efficiency, with the increase in the number of active antennas, the ZF and RZF performed better.

For the next steps, it is intended to develop studies for the XL-MIMO system. As it is a new study, the system is not fully defined. Thus, it is possible to work with new channel models and proceed with analyzes of the combiners. Regarding the combiners, due to the better performance of the MMSE, it is possible to develop techniques that reduce its complexity.

Bibliography

ALBDRAN, S.; ALSHAMMARI, A.; AHAD, M. A. R.; MATIN, M. Effect of exponential correlation model on channel estimation for massive mimo. *2016 19th International Conference on Computer and Information Technology (ICCIT)*, IEEE, Dhaka, Bangladesh, 2016. Cited on page 35.

ALI, A.; CARVALHO, E. D.; HEATH, R. W. Linear receivers in non-stationary massive mimo channels with visibility regions. *IEEE Wireless Communications Letters*, v. 8, n. 3, p. 885–888, June 2019. ISSN 2162-2345. Cited on page 27.

AMIRI, A.; ANGJELICHINOSKI, M.; CARVALHO, E. de; HEATH, R. W. Extremely large aperture massive MIMO: Low complexity receiver architectures. In: *2018 IEEE Globecom Workshops (GC Wkshps)*. Abu Dhabi, United Arab Emirates: IEEE, 2018. p. 1–6. ISSN null. Cited on page 84.

AMIRI, A.; REZAIE, S.; MANCHON, C. N.; CARVALHO, E. de. *Distributed Receivers for Extra-Large Scale MIMO Arrays: A Message Passing Approach*. 2020. Cited on page 27.

ARIAS, M. R.; MANDERSSON, B. An approach of the geometrical-based single bounce elliptical channel model for mobile environments. In: *The 8th International Conference on Communication Systems, 2002. ICCS 2002*. Singapore: IEEE, 2002. v. 1, p. 11–16 vol.1. Cited on page 43.

BAKHSHI, G.; SAADAT, R.; SHAHTALEBI, K. A modified two-ring reference model for mimo mobile-to-mobile communication channels. In: *2008 International Symposium on Telecommunications*. Tehran, Iran: IEEE, 2008. p. 409–413. Cited on page 43.

BELSLEY, D. A.; KUH, E.; WELSCH, R. Regression diagnostics: identifying influential data and sources of collinearity. Wiley, 1980. Cited on page 58.

BJÖRNSON, E.; HOYDIS, J.; SANGUINETTI, L. Massive MIMO networks: Spectral, energy, and hardware efficiency. *Foundations and Trends® in Signal Processing*, v. 11, n. 3-4, p. 154–655, 2017. ISSN 1932-8346. Available on: <http://dx.doi.org/10.1561/20000000093>. Cited 5 times on page(s) 45, 47, 48, 75, and 76.

BJÖRNSON, E.; HOYDIS, J.; SANGUINETTI, L. Massive mimo has unlimited capacity. *IEEE Transactions on Wireless Communications*, v. 17, n. 1, p. 574–590, Jan 2018. ISSN 1536-1276. Cited 4 times on page(s) 28, 44, 75, and 88.

BJÖRNSON, E.; LARSSON, E. G.; MARZETTA, T. L. Massive mimo: ten myths and one critical question. *IEEE Communications Magazine*, v. 54, n. 2, p. 114–123, February 2016. ISSN 0163-6804. Cited on page 27.

BJÖRNSON, E.; SANGUINETTI, L. Making cell-free massive MIMO competitive with MMSE processing and centralized implementation. *IEEE Transactions on Wireless Communications*, v. 19, n. 1, p. 77–90, Jan. 2020. ISSN 1558-2248. Cited on page 88.

- BJÖRNSON, E.; SANGUINETTI, L.; HOYDIS, J.; DEBBAH, M. Optimal design of energy-efficient multi-user MIMO systems: Is massive MIMO the answer? *IEEE Transactions on Wireless Communications*, v. 14, n. 6, p. 3059–3075, Jun. 2015. ISSN 1558-2248. Cited on page 39.
- BJÖRNSON, E.; SANGUINETTI, L.; WYMEERSCH, H.; HOYDIS, J.; MARZETTA, T. L. Massive MIMO is a Reality – What is Next? Five Promising Research Directions for Antenna Arrays. *arXiv e-prints*, p. arXiv:1902.07678, Feb 2019. Cited on page 43.
- BOROUJERDI, M. N.; HAGHIGHATSHOAR, S.; CAIRE, G. Low-complexity statistically robust precoder/detector computation for massive mimo systems. *IEEE Transactions on Wireless Communications*, v. 17, n. 10, p. 6516–6530, Oct 2018. ISSN 1558-2248. Cited 3 times on page(s) 28, 85, and 86.
- CARVALHO, E. D.; ALI, A.; AMIRI, A.; ANGJELICHINOSKI, M.; HEATH, R. W. Non-stationarities in extra-large-scale massive MIMO. *IEEE Wireless Communications*, v. 27, n. 4, p. 74–80, Aug. 2020. Cited 2 times on page(s) 50 and 81.
- CARVALHO, E. de; ALI, A.; AMIRI, A.; ANGJELICHINOSKI, M.; JR., R. W. H. Non-stationarities in extra-large scale massive MIMO. *CoRR*, abs/1903.03085, 2019. Available on: (<http://arxiv.org/abs/1903.03085>). Cited 2 times on page(s) 27 and 37.
- CHEN, J.-q.; ZHANG, Z.; TANG, T.; HUANG, Y.-z. A non-stationary channel model for 5g massive mimo systems. *Frontiers of Information Technology & Electronic Engineering*, v. 18, n. 12, p. 2101–2110, Dec 2017. ISSN 2095-9230. Available on: (<https://doi.org/10.1631/FITEE.1700028>). Cited 4 times on page(s) 27, 37, 50, and 81.
- CHIUEH, T.-D.; TSAI, P.-Y.; I-WEI, L.; CHIUEH, T.-D. Baseband receiver design for wireless mimo-ofdm communications. Wiley Online Library, 2012. Cited on page 29.
- COSTA, N.; HAYKIN, S. Multiple-Input, Multiple-Output Channel Models. 2011. Cited on page 58.
- DESIMONE, R.; BRITO, B. M.; BASTON, J. Model of indoor signal propagation using log-normal shadowing. p. 1–4, 2015. Cited on page 30.
- FILHO, J. C. M.; PANAZIO, C.; ABRÃO, T.; TOMASIN, S. Total energy efficiency of tr-mrc and fd-mrc receivers for massive mimo uplink. *IEEE Systems Journal*, v. 13, n. 3, p. 2285–2296, Sep. 2019. ISSN 2373-7816. Cited on page 39.
- FONTAN, F. P.; ESPIEIRA, P. M. Modelling the wireless propagation channel: A simulation approach with matlab. Wiley Publishing, 2008. Cited on page 29.
- GAO, X.; EDFORS, O.; TUFVESSON, F.; LARSSON, E. G. Massive mimo in real propagation environments: Do all antennas contribute equally? *IEEE Transactions on Communications*, v. 63, n. 11, p. 3917–3928, Nov 2015. ISSN 0090-6778. Cited on page 47.
- HOYDIS, J.; HOEK, C.; WILD, T.; BRINK, S. ten. Channel measurements for large antenna arrays. In: *2012 International Symposium on Wireless Communication Systems (ISWCS)*. Paris, France: IEEE, 2012. p. 811–815. Cited on page 65.
- IMOIZE, A. E.; ATAYERO, A. A.; KAVITHA, K. V. N. Standard propagation channel models for mimo communication systems. *Hindawi*, v. 2021, 2021. Available on: (<https://doi.org/10.1155/2021/8838792>). Cited on page 28.

- KIM, H. Wireless communications systems design. John Wiley & Sons, 2015. Cited on page 29.
- KYÖSTI, P.; MEINILÄ, J.; HENTILA, L.; ZHAO, X.; JÄMSÄ, T.; SCHNEIDER, C.; NARANDZIC, M.; MILOJEVIĆ, M.; HONG, A.; YLITALO, J.; HOLAPPA, V.; ALATOSSAVA, M.; BULTITUDE, R.; JONG, Y.; RAUTIAINEN, T. Winner ii channel models. *IST-4-027756 WINNER II D1.1.2 V1.2*, 02 2008. Cited on page 30.
- LARSSON, E. G.; EDFORS, O.; TUFVESSON, F.; MARZETTA, T. L. Massive mimo for next generation wireless systems. *IEEE Communications Magazine*, v. 52, n. 2, p. 186–195, February 2014. ISSN 0163-6804. Cited on page 27.
- LIM, H.; JANG, Y.; YOON, D. Bounds for eigenvalues of spatial correlation matrices with the exponential model in mimo systems. *IEEE Transactions on Wireless Communications*, v. 16, n. 2, p. 1196–1204, Feb 2017. ISSN 1536-1276. Cited on page 35.
- LOYKA, S. L. Channel capacity of mimo architecture using the exponential correlation matrix. *IEEE Communications Letters*, v. 5, n. 9, p. 369–371, Sep. 2001. ISSN 1089-7798. Cited 2 times on page(s) 37 and 44.
- LU, L.; LI, G. Y.; SWINDLEHURST, A. L.; ASHIKHMIN, A.; ZHANG, R. An overview of massive mimo: Benefits and challenges. *IEEE Journal of Selected Topics in Signal Processing*, v. 8, n. 5, p. 742–758, Oct 2014. ISSN 1932-4553. Cited on page 27.
- MARZETTA, T. L. Noncooperative cellular wireless with unlimited numbers of base station antennas. *IEEE Transactions on Wireless Communications*, v. 9, n. 11, p. 3590–3600, November 2010. ISSN 1558-2248. Cited on page 28.
- MARZETTA, T. L.; LARSSON, E. G.; YANG, H.; NGO, H. Q. Fundamentals of massive mimo. Cambridge University Press, 2016. Cited 2 times on page(s) 27 and 38.
- MIAH, M. S.; RAHMAN, M. M.; GODDER, T.; SINGH, B. C.; PARVIN, M. T. Performance comparison of awgn, flat fading and frequency selective fading channel for wireless communication system using 4qpsk. *International Journal of Computer and Information Technology*, 2011. Cited on page 30.
- MIAO, Y.; TAKADA, J.; SAITO, K.; HANEDA, K.; A.GLAZUNOV, A.; GONG, Y. Comparison of plane wave and spherical vector wave channel modeling for characterizing non-specular rough-surface wave scattering. *IEEE Antennas and Wireless Propagation Letters*, v. 17, n. 10, p. 1847–1851, Oct 2018. ISSN 1536-1225. Cited on page 27.
- NADEEM, Q.-U.-A.; KAMMOUN, A.; DEBBAH, M.; ALOUINI, M.-S. Asymptotic analysis of rzf over double scattering channels with mmse estimation. *IEEE Transactions on Wireless Communications*, v. 18, n. 5, p. 2509–2526, 2019. Cited on page 38.
- OESTGES, C.; CLERCKX, B. *MIMO Wireless Communications: From Real-World Propagation to Space-Time Code Design*. Elsevier Science, 2007. ISBN 9780080549989. Available on: <https://books.google.com.br/books?id=M3Yr9u3vrZ8C>. Cited 3 times on page(s) 37, 50, and 81.
- PTZOLD, M. Mobile radio channels. Wiley Publishing, 2012. Cited 2 times on page(s) 35 and 45.

RODRIGUES, V. C.; FILHO, J. C. M.; ABRÃO, T. Randomized kaczmarz algorithm for massive mimo systems with channel estimation and spatial correlation. *International Journal of Communication Systems*, v. 32, n. 18, p. e4158, 2019. E4158 dac.4158. Available on: <https://onlinelibrary.wiley.com/doi/abs/10.1002/dac.4158>. Cited 4 times on page(s) 28, 40, 85, and 87.

ROSA, K. B.; MARINELLO, J. C.; ABRAO, T. Low-complexity kaczmarz precoding in dl massive mimo with partial csi and correlation. *Physical Communication*, v. 37, p. 100902, 2019. ISSN 1874-4907. Available on: <http://www.sciencedirect.com/science/article/pii/S1874490719304045>. Cited 2 times on page(s) 28 and 89.

SANGUINETTI, L.; BJÖRNSON, E.; HOYDIS, J. Toward massive MIMO 2.0: Understanding spatial correlation, interference suppression, and pilot contamination. *IEEE Transactions on Communications*, v. 68, n. 1, p. 232–257, Jan. 2020. ISSN 1558-0857. Cited 3 times on page(s) 47, 80, and 88.

TAMADDONDAR, M. M.; NOORI, N. Plane wave against spherical wave assumption for non-uniform linear massive mimo array structures in los condition. In: *2017 Iranian Conference on Electrical Engineering (ICEE)*. Tehran, Iran: IEEE, 2017. p. 1802–1805. Cited on page 27.

VESA, A.; ALEXA, F.; BALTA, H. Comparisons between 2d and 3d uniform array antennas. In: *2015 Federated Conference on Computer Science and Information Systems (FedCSIS)*. Poland, Lodz: Annals of Computer Science and Information Systems, 2015. p. 1285–1290. Cited on page 27.

WANG, C.; HONG, X.; GE, X.; CHENG, X.; ZHANG, G.; THOMPSON, J. Cooperative mimo channel models: A survey. *IEEE Communications Magazine*, v. 48, n. 2, p. 80–87, February 2010. ISSN 0163-6804. Cited on page 34.

WANG, C.-X.; HONG, X.; WU, H.; XU, W. Spatial-temporal correlation properties of the 3gpp spatial channel model and the kronecker mimo channel model. *EURASIP Journal on Wireless Communications and Networking*, v. 2007, n. 1, p. 039871, Feb 2007. ISSN 1687-1499. Available on: <https://doi.org/10.1155/2007/39871>. Cited on page 34.

WANG, C.-X.; WU, S.; BAI, L.; YOU, X.; WANG, J.; I, C.-L. Recent advances and future challenges for massive mimo channel measurements and models. *Science China Information Sciences*, v. 59, n. 2, p. 1–16, Feb 2016. ISSN 1869-1919. Available on: <https://doi.org/10.1007/s11432-015-5517-1>. Cited 2 times on page(s) 35 and 43.

WU, S. et al. *Massive MIMO channel modelling for 5G wireless communication systems*. Tese (Doutorado) — Heriot-Watt University, 2015. Cited on page 34.

XIE, Y.; LI, B.; ZUO, X.; YANG, M.; YAN, Z. A 3d geometry-based stochastic model for 5g massive mimo channels. In: *2015 11th International Conference on Heterogeneous Networking for Quality, Reliability, Security and Robustness (QSHINE)*. Taipei, Taiwan: IEEE, 2015. p. 216–222. Cited 2 times on page(s) 36 and 48.

YIN, X.; CHENG, X. *Propagation Channel Characterization, Parameter Estimation, and Modeling for Wireless Communications*. Wiley-Blackwell, 2016. Cited on page 45.

YU, K.; OTTERSTEN, B. Models for mimo propagation channels: a review. *Wireless Communications and Mobile Computing*, v. 2, n. 7, p. 653–666, 2002. Available on: <https://onlinelibrary.wiley.com/doi/abs/10.1002/wcm.78>. Cited on page 43.

ZHENG, K.; OU, S.; YIN, X. Massive mimo channel models: A survey. *International Journal of Antennas and Propagation*, v. 2014, p. 1–10, 06 2014. Cited 5 times on page(s) 27, 34, 36, 45, and 48.

Appendix

APPENDIX A – Full paper
published in the journal
*”Transactions on Emerging
Telecommunications Technologies”*

Title: Stochastic Channel Models for Massive and XL-MIMO Systems.

Authors: Lígia May Taniguchi and Taufik Abrão.

DOI: <https://doi.org/10.1002/ett.4099>

Journal: Transactions on Emerging Telecommunications Technologies (ISSN 2161-3915).

Classification (Qualis-CAPES): A2 / IF=1.594 (Engenharias IV).

Volume: 31.

Issue: 9

Pp.: e4099

Publication Date: September 2020.

Summary

In this paper, stochastic channel models for massive MIMO (M-MIMO) and extreme large MIMO (XL-MIMO) system applications are described, evaluated and systematically compared. This work aims to cover new aspects of massive MIMO stochastic channel models in a comprehensive and systematic way. For that, we compare different models, presenting graphically and intuitively the behavior of each model. Each massive MIMO channel model emulates the environment using different methodologies and properties. Using metrics such as capacity, SINR, singular values decomposition (SVD), and condition number, one can understand the influence of each characteristic on the modelling and how it differentiates from other models. Moreover, in new XL-MIMO scenarios, where the near-field and visible region (VR) effects arise, our findings demonstrate that for the two assumed schemes of clusters distribution, the clusters location influences the performance of the conjugate beamforming and zero-forcing (ZF) precoding due to the correlation effect, which have been analysed from the geometric massive MIMO channel models.

Keywords: Stochastic channel models, Geometric models, Correlation models, Extreme large massive MIMO (XL-MIMO), Non-stationarity, Visibility region (VR).

APPENDIX B – Full paper
submitted in the journal
*”Transactions on Emerging
Telecommunications Technologies”*

Title: Resource Efficiency and Pilot Decontamination in XL-MIMO Double-Scattering Correlated Channels.

Authors: Lígia May Taniguchi, João de Souza, David William Guerra and Taufik Abrão.

Journal: Transactions on Emerging Telecommunications Technologies (ISSN 2161-3915).

Classification (Qualis-CAPES): A2 / IF=1.594 (Engenharias IV).

Submission Date: Revised R1 version on May, 2021.

Resource Efficiency and Pilot Decontamination in XL-MIMO Double-Scattering Correlated Channels

Lígia May Taniguchi, João Henrique Inacio de Souza, David William Marques Guerra, Taufik Abrão

Abstract

In Extra Large Scale MIMO system (XL-MIMO) due to the large antenna-array dimensions, the signal received at BS results in spatial non-stationarities, where only some regions are visible in the array. The double-scattering channel modelling considering local clusters on both the BS and the user side is a feasible and reliable model deployed to predict the XL-MIMO channel behaviour. The minimum mean-squared error (MMSE) channel estimator is deployed as a component of the XL-MIMO analysis, considering the zero-forcing (ZF), randomized Kaczmarz regularized zero-forcing (rKZF) and the MMSE combining schemes. The XL antennas regime is evaluated according to the interference between the users signals, using the variance metric. Because the XL-MIMO system could be applied to crowded single-cell environments, pilot contamination (PC) effect could arise due to visibility regions (VRs) from different users overleaping the same subset of antennas. Thus, despite the MMSE combiner presenting high-complexity cost, its capability in mitigating the pilot contamination effect, and even in eliminating such effect in asymptotic XL-MIMO antenna regime justify its high-performance in terms of spectral efficiency (SE). To demonstrate the effectiveness of the proposed combining methods against pilot contamination in uplink (UL) XL-MIMO systems, the linear MMSE, ZF and rKZF are compared, where the ZF combiner has been emulated by randomized Kaczmarz algorithm (rKA), by improving performance-complexity trade-off of ZF combiner in representative crowded XL-MIMO scenarios.

Index Terms

MMSE combining; Extra-large MIMO (XL-MIMO); randomized Kaczmarz algorithm (rKA); Visibility regions (VRs); Near-field; Subarray.

I. INTRODUCTION

The Extra Large Scale MIMO (XL-MIMO) system has been proposed to offer a potential increase in data rate transmission, where hundreds or thousands of antennas elements are disposed at BS to performed the communication to the user. However, this recent system presents some challenges for implementation since the large number of antennas results in some characteristics not seen in systems with a small number of antennas. The first characteristic is called non-stationarity, in which it demonstrates that in a large set of antennas, the antenna elements do not receive the same signal, *i.e.*, only some regions of the array can be activated by an user. The second characteristic can be interpreted by the size of the antenna array or by the user's proximity to the array, called the spherical wave-front, where it represents a difference in the signal between the antennas elements. The non-stationarity represents a difference of received signal between visibility regions while the spherical wave-front considers a difference signal between the antennas elements even inside of the visibility region. Thus,

L. M. Taniguchi and T. Abrão are with the Electrical Engineering Department, State University of Londrina, PR, Brazil. E-mail: ligia.lmt@gmail.com; taufik@uel.br

in works as [1]–[5], were addresses the channel modeling and estimation, the receivers design, and the precoding schemes, considering the characteristics cited; however these research topics are considered as open problems.

The XL-MIMO arrays are intended to deploy architectural structures in the environment, such as large walls and ceilings of buildings. Examples of applications include stadiums, shopping malls, as well as musical and other cultural festivals. In crowded scenarios, the pilot reuse is unavoidable to provide full connectivity, since the number of pilot sequences simultaneously available is limited, while the number of active user equipment (UE) is large. As well-known, the reuse of pilot sequences in massive MIMO results in pilot contamination, affecting the channel estimation process due to intra-cell interference. A scheme to mitigate the inter-cell pilot contamination is proposed in [6], providing under certain conditions unlimited spectral efficiency (SE) in massive MIMO systems. We demonstrate that the XL-MIMO array can be governed by the same principle, dealing with the intra-cell interference owed to the pilot reuse even under the channel spatial non-stationarities effect.

Recent works on the XL-MIMO systems includes [7], [8], [5] [2], [4]. In [7] we provide an extensive review of channel models for massive MIMO and XL-MIMO. Therein, we discuss the main characteristics of the stationary and non-stationary channels modeled by stochastic correlation-based and geometric-based models. Using different metrics, we demonstrate the impact of the clusters distribution on the XL-MIMO channel performance due to the correlation effect. Still commenting on the channel model, the authors in [8] update the double-scattering model aiming to capture the non-stationarities of the XL-MIMO channel. Moreover, the channel estimation problem in XL-MIMO is addressed in [5].

The XL-MIMO transceiver design can be found in [1], [8] and [2], [4]. The performance of linear receivers in a non-stationary XL-MIMO channels is analyzed in [1]. The results demonstrate that the spatial non-stationarities combined with the right signal processing techniques can provide substantial improvements on the performance, or otherwise deterioration. The authors in [8] contribute with scalable distributed receiver designs based on the variational message passing (VMP) and successive interference cancellation (SIC). The proposed designs cover a wide range of complexity-performance trade-off, being suitable to adapt to different requirements. More on XL-MIMO receivers can be found in [2], [4].

The works [3], [9], [10] deal with resource allocation in XL-MIMO, specifically the antenna selection problem. Particularly, in [10] the authors propose a per-subarray decentralized scheme to select the active antennas aiming to maximize the spectral efficiency (SE) in systems with limited number of radio-frequency transceivers.

In this way, the focus of this paper is to analyze three combining schemes as the Zero-Forcing (ZF), regularized ZF (RZF) and MMSE combining, in which we present the regularized ZF (RZF) combining using the randomized Kaczmarz (rKA) algorithm proposed by [11]. The RZF-rKA combiner was proposed to present a competitive performance even without the exact knowledge of the channel and a low computational cost due to the combiner not performs the inverse of the matrix. Among the combiners, only the RZF-rKA proposes a robust performance for a imperfect channel estimation due to the pilot contamination, where in [4], the combiner was analyzed in a XL-MIMO system considering subarrays for the performance of the precoder instead of the total set of antennas.

Although pilot contamination is a limiting factor to the performance of the system [12], in [6] was presented that in a massive MIMO system is possible to performs unlimited spectral efficiency by mitigate the pilot contamination. The analysis consists of employing a MMSE combining scheme to a multicell scenario, considering a MMSE estimator. This combiner estimates the channel from users of the own cell and the neighboring cells such that is generated a combining vector for each user, where the combiner can eliminate the channel of users that shares the same pilot sequence. Thus, from this perspective, this paper aims to describe the MMSE combining for a XL-MIMO system in order to mitigate the

pilot contamination. However, this scenario presents some conceptual differences as the environment of implementation, without a multicellular scenario, and the channel modeling, which are considered for analysis of the system.

Contribution: the contribution of this work is twofold. We have analysed the effectiveness of the massive MMSE combiner in crowded XL-MIMO applications in terms of both spectral efficiency (SE) and the capability of eliminating the pilot contamination problem. Second, we have characterized such effectiveness by comparing the performance and complexity of the M-MIMO combiner with the classical linear ZF, and RZF combiners, emulated by deploying the rKA approach. Such approach allows balancing performance vs complexity of the classical MIMO combiners.

The paper was organized as follows. Section II we describe the system model, considering a double-scattering channel model and a simplified version with a single-scattering for the XL-MIMO systems, as well as the MMSE, zF and rKA combining schemes. Section III defines the spectral efficiency and the energy efficiency as performance metrics. Section IV analyses the performance of the combining schemes, and in Section V are offered the conclusions.

II. SYSTEM MODEL

In this section, we describe the channel model for XL-MIMO as well as the combining schemes. In this system, there are M antennas at BS to serve K single-antenna users, where the channel estimation was performed by MMSE estimator. For the channel modelling, we consider two models: single and double scattering XL-MIMO channel models. In the single-scattering, there is just one linear cluster of scatterers between the BS and the user, while in the double-scattering model, there are two linear clusters in both sides of the communication, *i.e.*, a linear cluster of scatterers in BS and UE sides, respectively. Also, we present the ZF, RZF emulated by rKA, namely rKZF, and the MMSE combiner.

A. Uplink XL-MIMO

The uplink (UL) and downlink (DL) mode can be performed using a time-division duplex (TDD) protocol. Thus, the channel response is the same in UL and DL due to the principle of reciprocity, where the UL and DL times are small compared to the channel coherence time. To process the UL and DL, BS needs to know the channel response. A method for acquisition of the channel response is through pilot signalling. For this, it is transmitted a pilot signal, where each signal is orthogonal (in a time period) to the other and known at the receiver side. Thus, when the pilot signal is received, the receiver can estimate and separate the signals from each transmitting antenna. Based on [13], for the proposed system, we describe the pilot signal received and processed in the subarray b as:

$$\mathbf{Y}_{(b)} = \sum_{l \in \mathcal{K}_b} \sum_{i \in \mathcal{C}_{kb}} \sqrt{p_{ul}} \mathbf{h}_{li(b)} \phi_l^T + \mathbf{N} \quad (1)$$

where $\mathcal{K}_b = \{l = 1, \dots, L_s\}$ and $\mathcal{C}_{kb} = \{i = 1, \dots, C_s\}$, with L_s users and C_s clusters active in the b th subarray (SA). p_{ul} is the transmit power, $\mathbf{h}_{li(b)} \in \mathbb{C}^{M_{vr} \times 1}$ is the channel between the cluster i of the l th UE and the b th subarray in the BS, $\mathbf{N} \in \mathbb{C}^{M_{vr} \times \tau_p}$ is the receiver noise with i.i.d. elements distributed as $\mathcal{CN}(0, \sigma^2)$, $\phi_l \in \mathbb{C}^{\tau_p \times 1}$ is the pilot assigned to UE i , in which $\|\phi_l\|^2 = \tau_p$.

To estimate the channel from the i th cluster of the l th UE, considering that in the proposed system every user shares the same pilot sequence, the BS first correlates the received signal with the associated pilot signal to obtain:

$$\mathbf{z}_{l(b)} = \mathbf{Y}_{(b)} \phi_l^* = \sum_{l \in \mathcal{K}_b} \sum_{i \in \mathcal{C}_{kb}} \sqrt{p_{ul}} \tau_p \mathbf{h}_{li(b)} + \mathbf{N} \phi_l^* \quad (2)$$

Adopting the MMSE channel estimator, the estimated channel is obtained by calculating:

$$\hat{\mathbf{h}}_{li(b)} = \Phi_{li(b)} \mathbf{Q}_{(b)}^{-1} \left(\frac{1}{\tau_p \sqrt{p_{ul}}} \mathbf{z}_{l(b)} \right) \quad (3)$$

where $\Phi_{li(b)}$ is the channel correlation matrix related to the b th subarray and channel response $\mathbf{h}_{li(b)}$; moreover, matrix $\mathbf{Q}_{(b)}$ is defined as

$$\mathbf{Q}_{(b)} = \mathbb{E}\{\mathbf{z}_{l(b)} \mathbf{z}_{l(b)}^H\} = \sum_{l \in \mathcal{K}_b} \sum_{i \in \mathcal{C}_{kb}} \Phi_{li(b)} + \frac{\sigma^2}{\tau_p p_{ul}} \mathbf{I}_{M_{VR}} \quad (4)$$

where $(\cdot)^H$ is the Hermitian operator.

Combiner: for detecting the *payload data transmission*, different low-complexity linear combining schemes can be deployed at the massive BS antennas. Starting with the received data signal at the subarray b in the BS:

$$\mathbf{Y}_{(b)}^u = \sum_{l \in \mathcal{K}_b} \sum_{i \in \mathcal{C}_{kb}} \sqrt{p_{ul}} \mathbf{h}_{li(b)} \mathbf{s}_l^T + \mathbf{N}^u \quad (5)$$

where $\mathbf{s}_l \in \mathbb{C}^{\tau_u \times 1}$ with τ_u i.i.d. elements distributed as $\mathcal{CN}(0, 1)$ are the data symbols from the l th UE, and $\mathbf{N}^u \in \mathbb{C}^{M_{VR} \times \tau_u}$ is the receiver noise with i.i.d. elements distributed as $\mathcal{CN}(0, \sigma^2)$.

Thus, the BS selects a combining scheme for each user's active cluster at each subarray, *i.e.*, the combiner vector $\mathbf{v}_{li(b)} \in \mathbb{C}^{M_{VR} \times 1}$ that uses the channel estimation obtained from the pilot signaling is correlated with the received signal $\mathbf{Y}_{(b)}^u$ as:

$$\begin{aligned} \mathbf{v}_{li(b)}^H \mathbf{Y}_{(b)}^u &= \underbrace{\mathbf{v}_{li(b)}^H \mathbf{h}_{li(b)} \mathbf{s}_l}_{\text{Desired signal}} + \\ &\quad \underbrace{\sum_{l' \in \mathcal{K}_b \setminus l} \sum_{i' \in \mathcal{C}_{l'b}} \mathbf{v}_{l'i'(b)}^H \mathbf{h}_{l'i'(b)} \mathbf{s}_{l'}}_{\text{Interference}} + \underbrace{\mathbf{v}_{li(b)}^H \mathbf{N}^u}_{\text{Noise}} \end{aligned} \quad (6)$$

generating three terms: desired signal, interference and noise.

B. Channel Model

In XL-MIMO the number of antennas and the array dimension can be considered extremely large, typically thousands of antennas, while the users distance to the array is very short compared to the array size, *i.e.*, the far-field assumption does not hold. Thus, due to such configuration, spatial non-stationarities arise; as a result, the signal from the user can be observed by different, small disjunct subsets of antennas, called *visibility region* (VR), where these regions generally does not include the *visibility* of the total array of antennas [14]. As reported by measurements in [15], it is necessary consider the non-stationary from a spatial perspective [16].

Two extreme-large MIMO channel models have been considered in this work: double-scattering XL channel and single-scattering XL channel.

1) *Double-scattering Model:* In this XL-MIMO channel model, the channel between the k th user and the BS is composed by clusters located at user and BS sides, respectively, as depicted in Fig. 1. In such scenario, the user presents a single cluster composed by S linear scatterers, while near to the BS there are C BS-clusters; besides, each BS-cluster contains S_i scatterers.

For the formulation of the XL channel model, in the sequel, the user's communication with the i th XL BS-cluster is modelled such that results in a specific subset of visible antennas at BS:

$$\tilde{\mathbf{h}}_{i,k} = \Upsilon_i \rho_i^{\frac{1}{2}} \mathbf{R}_i^{\frac{1}{2}} \mathbf{G}_i \tilde{\mathbf{R}}_{i,k}^{\frac{1}{2}} \mathbf{D}_{i,k} \mathbf{g}_k \quad (7)$$

where $\Upsilon_i \in \{0, 1\}^{M \times r_i}$ represents the indices of the visible antennas, $\rho_i \in$ is the visibility gain matrix, \mathbf{G}_i is the complex scattering amplitudes, r_i is the number of visible antenna elements in the i th BS-cluster, while $\mathbf{D}_{i,k} = \mathbf{1}^{S_i \times S_k}$ is a matrix of ones with $S_i \times S_k$ dimensions representing the visibility of the k th user regarding the i th BS-cluster, and $\mathbf{g}_k \sim \mathcal{CN}(0, 1) \in \mathbb{C}^{S_k \times 1}$ is the small-scale fading. The matrices $\mathbf{R}_i \in \mathbb{C}^{r_i \times r_i}$ and $\tilde{\mathbf{R}}_{i,k} \in \mathbb{C}^{S_i \times S_i}$ are the correlation matrices on the BS side and the user side, respectively. The \mathbf{R}_i defines the correlation matrix between the signals that arrive at BS, according to physical parameters, as location of each BS-cluster and the antenna spacing, being modelled as:

$$[\mathbf{R}_i]_{m,l} = \frac{1}{S_i} \sum_{n=\frac{1-S_i}{2}}^{\frac{S_i-1}{2}} e^{-2\pi j(m-l)d_r \cos\left(\frac{\pi}{2} + \varphi_i + \frac{n\vartheta_i}{S_i-1}\right)} \quad (8)$$

where (m, l) corresponds to the elements of the correlation matrix, d_r is the λ -normalized antenna spacing at BS, with λ being the carrier wavelength, φ_i is the azimuth angle between the BS and the i th BS-cluster and ϑ_i is the angular spread around to the azimuth angle. For the user side, the correlation matrix is defined as:

$$[\tilde{\mathbf{R}}_{i,k}]_{m,l} = \frac{1}{S_i} \sum_{n=\frac{1-S_i}{2}}^{\frac{S_i-1}{2}} e^{-2\pi j(m-l)d_s \cos\left(\frac{\pi}{2} + \tilde{\varphi}_{i,k} + \frac{n\tilde{\vartheta}_{i,k}}{S_i-1}\right)} \quad (9)$$

where d_s is the λ -normalized spacing between the elements of the i th scatterer S_i , while $\tilde{\varphi}_{i,k}$ is the azimuth angle between the UE-cluster and the i th BS-cluster correspond to the user k and $\tilde{\vartheta}_{i,k}$ is the angular spread around to $\tilde{\varphi}_{i,k}$.

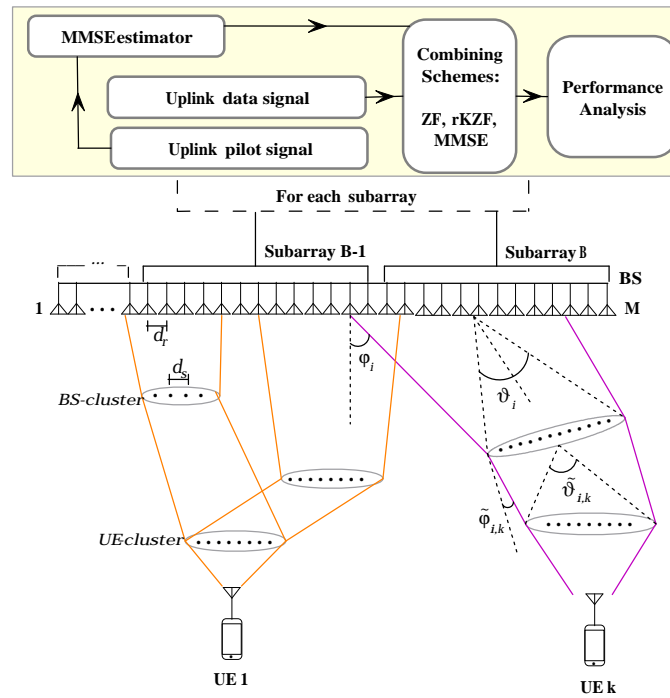


Fig. 1: Sketch of the uplink XL-MIMO system: (top) Combiner and channel estimation blocks; (bottom) the double-scattering channel model; (in between) M -antennas linear array with B subarrays. The distance between linear scattering-elements is d_s , while d_r holds for distance between antenna elements at BS.

The energy distribution ρ inside each cluster is defined as:

$$\rho_i = 10^{-\psi|c_i - d_r(n-1)|} \quad (10)$$

where n is the index of the antenna elements inside the cluster VR and ψ is a constant slop that attenuates the channel gain with the distance.

Thus, the k th user channel can be described combining all C clusters for the user k , such as:

$$\mathbf{h}_k = \sum_{i \in \mathcal{C}_k} \tilde{\mathbf{h}}_{i,k}, \quad (11)$$

where \mathcal{C}_k is the subset of active clusters visible to each user k .

2) *Single-scattering Model*: Unlike the double-scattering model, the single-scattering is composed by a single cluster between the BS and the UE. Thus the C clusters receive the signal from the UE and each cluster creates a VR at BS. The single-scattering description is a simplified but relatively generic XL model capable of describing and modeling the VRs due to the spatial non-stationarities. In our single-scattering model, the cluster is composed by S_i linear scatterers, being the formulation between the k th UE and the i th cluster given by:

$$\mathbf{h}_{i,k} = \Upsilon_i \rho_i^{\frac{1}{2}} \mathbf{R}_i^{\frac{1}{2}} \bar{\mathbf{g}}_k \quad (12)$$

where $\bar{\mathbf{g}}_k \in \mathbb{C}^{r_i \times 1}$ is the small-scale fading, while Υ_i , ρ_i , and \mathbf{R}_i are calculated in the same way as in eq. (7).

C. Processing Each Subarray

As well-known, in typical XL-MIMO scenarios, only some spatial regions of the XL array are visible to the user; hence, we split the large array of antennas into B subarrays with equal number M_b of antennas in each subarray. Hence, each subarray evaluates the received signal, and only the subset of subarrays that accumulate the most part of signal energy (say at least 90%) is selected. Such methodology for subarrays selection was presented in [2], where the algorithm, called Bipartite graph, determines which part of the matrix the user power is dominant. By using smaller subarrays for the signal processing, including the combiner, one is able to reduce the computational complexity, since a smaller number of antennas equal to M_b is deployed.

Thus, based on the choice of which subarray processes each user's signal, in the sequel we analyze the processing of each subarray separately. We build the combination schemes, using the massive channel estimate in the selected subarray and calculate the performance of each combiner in terms of spectral and energy efficiency of the XL-MIMO system.

Starting from the choice of the subarray for signal processing, the elements of the channel vector and the correlation matrix are defined. For example, if the chosen subarray represents the first 10 antenna elements of the BS, we select the first 10 elements of the channel vector for processing. However, for the correlation matrix, such selection is not straightforward, as its dimension depends on the length of the VR. Thus, we define two situations: *i*) the VR includes the first 10 antenna elements; *ii*) the VR does not include the first 10 antenna elements. If the VR covers the first 10 elements, such elements are selected from the correlation matrix. However, if the VR partially covers the first 10 antenna elements, then the correlation matrix is completed with zeros to obtain the dimension of the subarray and can perform the signal processing.

D. Combining Schemes

When a user transmits the signal to the BS, this signal suffers some effects of the channel, resulting in a received signal different from the transmitted signal. Thus, in order to identify the transmitted signal, it is fundamental a combining scheme, where, in this section, we define four combining schemes.

1) *Zero-forcing Combiner (ZF) for XL-MIMO*: A suboptimal combining is the ZF combiner, defined by the b th SA as:

$$\mathbf{v}_{(b)}^{\text{ZF}} = \hat{\mathbf{H}}_{(b)} (\hat{\mathbf{H}}_{(b)}^H \hat{\mathbf{H}}_{(b)})^{-1} \quad (13)$$

where $\hat{\mathbf{H}}_{(b)}$ is the estimated channel matrix of all clusters of each user of the b th subarray. The focus of the ZF is mitigate the interference of other users, however, the inverse of the matrix increases the computer complexity. The ZF is more recommended when the SNR is high.

2) *Randomized Kaczmarz Regularized Zero-Forcing (rKZF)*: The combining presented above are normally evaluated from the exact channel state information (CSI). However, it is a great challenge to estimate perfectly the channel due to the pilot contamination. Therefore, the authors in [11] propose a novel technique for computing the precoder/detector in a massive MIMO system, considering a imperfect channel estimation. The technique is based on the iterative Kaczmarz algorithm, where it was proposed initially for solving consistent over-determined (OD) set of linear equations (SLE). However, in [11] was extended this algorithm to the under-determined (UD) SLE, allowing the application of the algorithm to M-MIMO. Initially, we present the regularized KA represented to the RZF combining and then we described the randomized iterative KA algorithm.

rKZF Combiner for XL-MIMO: Considering the UL mode, the received signal is estimated as:

$$\hat{\mathbf{s}} = \mathbf{V}^H \mathbf{y} \quad (14)$$

where \mathbf{V} is the combining scheme and $\hat{\mathbf{s}} \in \mathbb{C}^K$ is the estimate vector of the transmitted symbols from each UE.

Defining the combining scheme as the regularized ZF (RZF), given by:

$$\mathbf{V}_{(b)}^{\text{RZF}} = (\hat{\mathbf{H}}_{(b)}^H \hat{\mathbf{H}}_{(b)} + \xi \mathbf{I}_K)^{-1} \hat{\mathbf{H}}_{(b)}^H \quad (15)$$

the estimate signal is:

$$\hat{\mathbf{s}} = (\hat{\mathbf{H}}_{(b)}^H \hat{\mathbf{H}}_{(b)} + \xi \mathbf{I}_K)^{-1} \hat{\mathbf{H}}_{(b)}^H \mathbf{y} \quad (16)$$

The signal estimation $\hat{\mathbf{s}}$ can be deduced as the optimum solution to the problem [11], [17]:

$$\arg \min_{\mathbf{w} \in \mathbb{C}^K} \|\hat{\mathbf{H}}_{(b)} \mathbf{w} - \mathbf{y}\|^2 + \xi \|\mathbf{w}\|^2 \quad (17)$$

where we can rewritten compactly the cost function above as $\|\mathbf{B}\mathbf{w} - \mathbf{y}_0\|_2^2$, in which $\mathbf{B} = [\hat{\mathbf{H}}_{(b)}; \sqrt{\xi} \mathbf{I}_K]$ is a $(M+K) \times K$ matrix and $\mathbf{y}_0 = [\mathbf{y}; \mathbf{0}]$ is a $(M+K) \times 1$ vector. An alternative to solve the compact optimization problem is $\mathbf{B}\mathbf{w} = \mathbf{y}_0$. The SLE is an overdetermined (OD) systems of equations, i.e., there are more equations than unknown variables; however, there is a inconsistency in the set equations due to the presence of the noise on the received signal \mathbf{y} . In [11], the inconsistency was removed by split the SLE in two steps.

Initially, we define a variable $\hat{\mathbf{y}}_0 \in \mathbb{C}^{(M+K)}$ as:

$$\hat{\mathbf{y}}_0 = \mathbf{B}\hat{\mathbf{s}} = \mathbf{B}(\mathbf{B}^H \mathbf{B})^{-1} \hat{\mathbf{H}}_{(b)}^H \mathbf{y} \quad (18)$$

where we can manipulate the equation by:

$$\mathbf{B}^H \hat{\mathbf{y}}_0 = (\mathbf{B}^H \mathbf{B})(\mathbf{B}^H \mathbf{B})^{-1} \hat{\mathbf{H}}_{(b)}^H \mathbf{y} = \hat{\mathbf{H}}_{(b)}^H \mathbf{y} \quad (19)$$

Let \mathbf{z}^t the estimation of $\hat{\mathbf{y}}_0$ at iteration t , the UD SLE above is consistent if \mathbf{z}^0 starts from the zero initialization $\mathbf{z}^0 = \mathbf{0}$ [11]. Thus, the UD SLE is consistent, because the estimate \mathbf{z}^t lies in the subspace generated by the columns of \mathbf{B} . Lastly, the estimate signal $\hat{\mathbf{s}}$ can be found by solve the consistent OD SLE:

$$\mathbf{B}\hat{\mathbf{s}} = \hat{\mathbf{y}}_0 \quad (20)$$

However, a direct way to estimate $\hat{\mathbf{s}}$ is through of the K last rows of $\hat{\mathbf{y}}_0$, dividing by $\sqrt{\xi}$. Thus, only the eq. (19) need to be solved by the rKA algorithm.

rKA: the Kaczmarz algorithm was described to solve equations in the form $\mathbf{A}\mathbf{w} = \mathbf{b}$. From an iterative way, the KA algorithm updates the \mathbf{w} in order to make equality close to the true value. At each iteration t , KA finds the closest vector \mathbf{w}^t and also approximates to $\langle \mathbf{a}_{r(t)}, \mathbf{w} \rangle = b_{r(t)}$, using the follow equation:

$$\mathbf{w}^{t+1} = \mathbf{w}^t + \frac{b_{r(t)} - \langle \mathbf{a}_{r(t)}, \mathbf{w} \rangle}{\|\mathbf{a}_{r(t)}\|^2} \mathbf{a}_{r(t)} \quad (21)$$

where $\mathbf{a}_{r(t)}$ is the r th row of \mathbf{A} , $b_{r(t)}$ is the r th element of \mathbf{b} and each row $r(t)$ is selected randomly with the probability $\frac{\|\mathbf{a}_{r(t)}\|_2^2}{\|\mathbf{A}\|_F^2}$.

As viewed before, to estimate the signal $\hat{\mathbf{s}}$, we need to solve the eq. (19). Thus, we assume $\mathbf{b} = \hat{\mathbf{H}}_{(b)}^H \mathbf{y}$ and we rewrote the eq. (21) as:

$$\mathbf{z}^{t+1} = \mathbf{z}^t + \underbrace{\frac{b_{r(t)} - \langle \mathbf{B}_{r(t)}, \mathbf{z}^t \rangle}{\|\mathbf{B}_{r(t)}\|^2}}_{\eta^t} \mathbf{B}_{r(t)} \quad (22)$$

where η is called as the residual term and the $r(t)$ row is selected randomly with the probability of:

$$\frac{\|\mathbf{B}_{r(t)}\|_2^2}{\|\mathbf{B}\|_F^2} = \frac{\|\hat{\mathbf{H}}_{(b),r(t)}\|_2^2 + \xi}{\|\hat{\mathbf{H}}_{(b)}\|_F^2 + K\xi} \quad (23)$$

As the K last rows contains the estimate signal, we can separate the \mathbf{z}^t as two vectors $\mathbf{u} \in \mathbb{C}^{M \times 1}$ and $\sqrt{\xi} \mathbf{v} \in \mathbb{C}^{K \times 1}$, where \mathbf{v} contains the estimate signal in each iteration t . Thus, by separate the vector \mathbf{z} , the residual term η can be rewritten as:

$$\eta^t = \frac{b_{r(t)} - \langle \hat{\mathbf{H}}_{(b),r(t)}, \mathbf{u}^t \rangle - \xi \mathbf{v}_{r(t)}^t}{\|\hat{\mathbf{H}}_{(b),r(t)}\|^2 + \xi} \quad (24)$$

where the vector \mathbf{u} and the r th element of \mathbf{v} are update by iteration, respectively, as:

$$\mathbf{u}^{t+1} = \mathbf{u}^t + \eta^t \hat{\mathbf{H}}_{(b),r(t)} \quad (25)$$

$$\mathbf{v}_{r(t)}^{t+1} = \mathbf{v}_{r(t)}^t + \eta^t, \text{ and } \mathbf{v}_j^{t+1} = \mathbf{v}_j^t \text{ for } j \neq r(t) \quad (26)$$

Algorithm 1 presents the rKA for estimate signal using the RZF combining.

Algorithm 1 rKA Signal Estimation

- 1: **Input** $\hat{\mathbf{H}}_{(b)}, \xi, T_{\text{rKA}}$
 - 2: Define $\mathbf{u}^0 = 0$ and $\mathbf{v}^0 = 0$
 - 3: **for** $t = 0 : T_{\text{rKA}} - 1$ **do**
 - 4: Pick a row $r(t)$ of $\hat{\mathbf{H}}_{(b)}$ with probability described in (23)
 - 5: Compute the residual term η as in (24)
 - 6: Update \mathbf{u} as in (25)
 - 7: Update \mathbf{v} as in (26)
 - 8: **end for**
 - 9: **Output** $\hat{\mathbf{s}} = \mathbf{v}^{T-1}$
-

Unlike Algorithm 1, in [17] it was studied a rKA version, in which the combining matrix is estimated instead of the data signal. Hence, in such rKA version, it were introduced a canonical basis vector $\mathbf{e}_k \in \mathbb{C}^K$, a vector $\mathbf{c}^t \in \mathbb{C}^{(M+K)} = [\mathbf{u}^t \mathbf{z}^t]$ and a matrix $\mathbf{D}^{\text{rKA}} \in \mathbb{C}^{K \times K}$. The elements of the canonical basis vector \mathbf{e}_k can assume two values: 1 or 0, where the k th element is 1 and otherwise is 0. Basically, the combining vector is obtained as $\mathbf{v}_k = \widehat{\mathbf{H}}_{(b)} \mathbf{d}_k$, where \mathbf{d}_k is the k th row of \mathbf{D}^{rKA} . The Algorithm 2 describes the rKA to estimate the RZF receive combining matrix.

Algorithm 2 rKZF Combiner for M-MIMO [17]

```

1: Input  $\widehat{\mathbf{H}}_{(b)}, \xi, T_{\text{rKA}}$ 
2: Define  $\mathbf{D}^{\text{rKA}} = \mathbf{0}_{K \times K}$ 
3: for  $k = 1 : K$  do
4:   Define  $\mathbf{u}^0 = \mathbf{0}_M$  and  $\mathbf{z}^0 = \mathbf{0}_K$ 
5:   Compute the  $\mathbf{e}_k$ 
6:   for  $t = 0 : T_{\text{rKA}} - 1$  do
7:     if  $t=0$  then
8:       Pick a  $k$ th row of  $\widehat{\mathbf{H}}_{(b)}$ 
9:     else
10:      Pick a row  $r(t)$  of  $\widehat{\mathbf{H}}_{(b)}$  with probability (23)
11:    end if
12:    Compute residue  $\eta^t = \frac{[\mathbf{e}_k]_{r(t)} - \langle \widehat{\mathbf{H}}_{r(t)}, \mathbf{u}^t \rangle - \xi z_{r(t)}^t}{\|\widehat{\mathbf{H}}_{r(t)}\|^2 + \xi}$ 
13:    Update  $\mathbf{u}^{t+1} = \mathbf{u}^t + \eta^t \widehat{\mathbf{H}}_{(b), r(t)}$ 
14:    Update  $z_{r(t)}^{t+1} = z_{r(t)}^t + \eta^t$ 
15:  end for
16:  Update  $[\mathbf{D}^{\text{rKA}}]_{:,k} = \mathbf{z}^{T_{\text{rKA}}-1}$ 
17: end for
18: Output  $\mathbf{V}^{\text{rKA}} = \widehat{\mathbf{H}}_{(b)} \mathbf{D}^{\text{rKA}}$ 

```

3) *MMSE Combiner for XL-MIMO*: A linear MMSE-based combining scheme for massive MIMO systems is presented in [6]. The M-MMSE combining maximizes the SINR by amplifying the desired signal and, in the case of M-MIMO systems, suppressing both intracellular and intercellular interference. The analysis indicate an unlimited spectral efficiency even with the presence of pilot contamination; however, it is showed that to mitigate the pilot contamination, the *covariance matrices of the users that share the same pilot sequence have to be asymptotically linearly independent*, i.e., from the theoretical analysis, the channel model hypotheses and implications affect the M-MIMO system performance in terms of SE.

Elaborating further, and adapting to the extra-large scale MIMO systems scenarios, indeed, in a XL-MIMO system, the theory behind the multicell channels is not suitable, because the context requires the large-antennas arrays deployment in environments where there are a lot of users clustered, i.e., single-cell crowded scenarios, as in stadium and huge open space environments. As well-known, the number of pilot sequences simultaneously available is limited, while the number of active UEs is large; as a result, in some practical XL-MIMO scenarios, pilot contamination effect is unavoidable.

Based on [6], [18], a MMSE combining scheme for XL-MIMO system can be conceived, in which the spatial region with K active users communicating with a BS equipped with an extreme-large antenna array, while the number of available pilot

sequences is insufficient, resulting in the reuse of the pilot sequences.

In the XL-MIMO context, the MMSE combiner scheme can be performed as (27), in which the MMSE combiner is defined by [13].

$$\mathbf{v}_{(b)}^{\text{MMSE}} = \left(\hat{\mathbf{H}}_{(b)} (\hat{\mathbf{H}}_{(b)})^H + \mathbf{Z}_{li} \right)^{-1} \hat{\mathbf{H}}_{(b)} \quad (27)$$

where $\mathbf{Z}_{l,i}$ in each subarray is defined as:

$$\mathbf{Z}_{(b)} = \sum_{l \in \mathcal{K}_b} \sum_{i \in \mathcal{C}_{kb}} (\Phi_{li} - \Phi_{li} \mathbf{Q}_{li}^{-1} \Phi_{li}) + \frac{\sigma^2}{p_{ul}} \mathbf{I}_{M_{VR}} \quad (28)$$

where $\Phi_{li} \in \mathbb{C}^{M_{VR} \times M_{VR}}$ is the correlation matrix of the i th user channel.

III. PERFORMANCE METRICS

In this section, we revisit relevant performance metrics aiming at comparing and analysing the different XL-MIMO linear combiners, including spectral efficiency (SE) and energy efficiency (EE) metrics, subject to channel error estimates.

A. MSE-RKZF Metric

The MSE metric is a measure of perfection in emulating the RZF combiner performance, defined as:

$$\text{MSE} = \frac{1}{MKN} \sum_{n=1}^N \sum_{k=1}^K \sum_{m=1}^M |v_{ml}^{\text{RZF}}(n) - v_{ml}^{\text{rKZF}}(n)|^2 \quad (29)$$

where M is the number of antennas at BS, K is the number of users, N is the number of realizations, $v_{ml}^{\text{RZF}}(n)$ is the (ml) th element of the n th realization of the combining matrix calculated by the conventional regularized ZF (RZF) (15), and $v_{ml}^{\text{rKZF}}(n)$ is the combiner vector element using rKA algorithm to emulate the RZF combiner.

B. Interference between users

With the aim of analyzing the interference that the UEs cause to each other when considered the single and double-scattering channel model, the variance of the favourable propagation is measured by:

$$\varsigma_{j,k} = \mathbb{V} \left\{ \frac{\mathbf{h}_{ji}^H \mathbf{h}_{ki}}{\sqrt{\mathbb{E}\{\|\mathbf{h}_{ji}\|^2\} \mathbb{E}\{\|\mathbf{h}_{ki}\|^2\}}} \right\} = \frac{\text{tr}(\Phi_{ji} \Phi_{ki})}{\text{tr}(\Phi_{ji}) \text{tr}(\Phi_{ki})} \quad (30)$$

This metric can perform how close the spatial correlation matrices related to the j th and k th users are, in which small values of variance $\varsigma_{j,k}$ results in small interference between the UEs channels, *i.e.*, the channels are closed to the orthogonality.

For this analysis, we evaluate the *interference* using the correlation matrix of each subarray separately. Thus, for single-scattering (SS) model (12), the correlation matrix of the i th cluster corresponding to the k th user is $\Phi_{ki}^{\text{SS}} = \mathbf{R}_i$. For the double-scattering (DS) in eq. (7), the channel matrix can be calculated as [19]:

$$\Phi_{ki}^{\text{DS}} = \text{tr}(\tilde{\mathbf{R}}_{i,k}) \mathbf{R}_i \quad (31)$$

C. Spectral Efficiency in XL-MIMO with Linear Combiners

The spectral efficiency (SE) measures the number of bits that can be transmitted across the channel free of errors, over a given channel bandwidth or equivalently per channel use (pcu) [20]. The sum-SE in the UL of XL-MIMO is defined according to:

$$\text{SE}^{\text{ul}} = \frac{\tau_u}{\tau_c} \sum_{b=1}^B \sum_{l \in \mathcal{K}_b} \sum_{i \in \mathcal{C}_{kb}} \log_2(1 + \gamma_{li(b)}^{\text{ul}}) \quad [\text{pcu}] \quad (32)$$

where the signal-to-interference-plus-noise ratio (SINR) is given by

$$\gamma_{ki(b)}^{\text{ul}} = \frac{|\mathbf{v}_{ki(b)}^H \hat{\mathbf{h}}_{ki(b)}|^2}{\mathbf{v}_{ki(b)}^H \left(\sum_{l \in \mathcal{K}_b} \sum_{i \in \mathcal{C}_{kb}} \hat{\mathbf{h}}_{li(b)} (\hat{\mathbf{h}}_{li(b)})^H - \hat{\mathbf{h}}_{ki(b)} (\hat{\mathbf{h}}_{ki(b)})^H + \mathbf{Z}^{(b)} \right) \mathbf{v}_{ki(b)}} \quad (33)$$

where τ_u is the UL data length, given by:

$$\tau_u = \tau_c - \tau_p - \tau_d \quad (34)$$

being τ_p and τ_d the length of the pilot sequence and downlink data, respectively. Notice that τ_c holds for the number of samples per coherence block, *i.e.*, the factor $\frac{\tau_u}{\tau_c}$ in eq. (32) refers to the fraction of samples per coherence block that is used for the UL data transmission. Indeed, inside the τ_c time interval occur the transmission of the pilot sequences (for channel estimation purpose), the DL data and UL data.

D. Energy Efficiency (EE)

The EE measures the amount of information that can be reliably transmitted per unit of energy, which is defined as the ratio of the sum-rate to the total power consumption:

$$\text{EE} = \frac{\text{SE}}{\text{ETP} + P_{\text{CP}}} \quad \left[\frac{\text{pcu}}{\text{W}} \right] \quad (35)$$

where ETP is the effective transmit power, calculated as $\text{ETP} = P_{\text{TX}}^{\text{ul}} + P_{\text{TX}}^{\text{tr}}$ and P_{CP} is the circuitry power. The variables $P_{\text{TX}}^{\text{ul}}$ and $P_{\text{TX}}^{\text{tr}}$ represent the power consumed by the RF amplifiers in the UL and UL pilot and data transmissions. It is common to find models that consider the circuit power as a constant term, normally, denominated P_{FIX} . However, this model is not accurate since it is not take accounts, *e.g.*, the digital signal processing and the network load. Thus, as presented in [21], [22], a realistic way to compute the circuit power consumption P_{CP} is given by:

$$P_{\text{CP}} = P_{\text{FIX}} + P_{\text{TC}} + P_{\text{CE}} + P_{\text{C/D}} + P_{\text{BH}} + P_{\text{LP}} \quad (36)$$

where P_{FIX} is a fixed power consumption corresponding, *e.g.*, to the control site-cooling and control signaling. The P_{TC} is the power consumption of the transceiver chains and calculated as:

$$P_{\text{TC}} = P_{\text{LO}} + M_b P_{\text{BS}} + K P_{\text{UE}} \quad (37)$$

where P_{LO} is the power consumed by the local oscillator, P_{BS} is the circuit power of each BS antenna and P_{UE} is the circuit power of each single-antenna UE. P_{CE} is the power consumption for the channel estimation, where the *computational efficiency* at the BS \mathcal{L}_{BS} is considered. The P_{CE} is calculated as:

$$P_{\text{CE}} = \frac{B_T}{\tau_c} \frac{\mathcal{C}_{\text{CHEST}}}{\mathcal{L}_{\text{BS}}} \quad (38)$$

where B_T the total bandwidth and $\mathcal{C}_{\text{CHEST}}$ is the number of complex multiplications, divisions, sums and subtractions to compute the channel estimate via (3), given by:

$$\mathcal{C}_{\text{CHEST}} = \sum_{b=1}^B C_b (2M_b^2 - M_b) + B (2M_b \tau_u - M_b) \quad (39)$$

considering C_b as the number of active clusters and M_b as the number of antennas, both associated with the subarray b . For the sake of simplicity, the complexity to estimate and compute the terms related to the correlation matrices are dropped.

This assumption is reasonable as the channel spatial correlation changes slower with time than the channel small-scale fading term, enabling the reuse of the computed matrices during many channel coherence blocks.

Also, the $P_{C/D}$ is the power consumption of the channel coding and decoding, given by:

$$P_{C/D} = B_T SE(\mathcal{P}_{\text{COD}} + \mathcal{P}_{\text{DEC}}) \quad (40)$$

where \mathcal{P}_{COD} and \mathcal{P}_{DEC} are the coding and decoding power densities, respectively. P_{BH} is the backhaul consumption power and it is calculated as:

$$P_{\text{BH}} = B_T SE \mathcal{P}_{\text{BT}} \quad (41)$$

where \mathcal{P}_{BT} is the backhaul traffic power density. Lastly, the power consumption of the linear processing at the BS P_{LP} that depends on the computational complexity of the combining/precoding.

Finally, the power consumed due to the signal processing is defined as:

$$P_{\text{LP}} = B_T \left(1 - \frac{\tau_u}{\tau_c} \right) \frac{\mathcal{C}_{\text{RECEP}}}{\mathcal{L}_{\text{BS}}} + \frac{B_T}{\tau_c} \frac{\mathcal{C}_{\text{COMB}}}{\mathcal{L}_{\text{BS}}} \quad (42)$$

where the first term represents the power consumed by the UL reception of the data signals, and the second one is the power consumed to compute the combining scheme. For the first term, the signal reception complexity of computing the combined signal, estimated by the number of complex operations to compute eq. (6), is equal to:

$$\mathcal{C}_{\text{RECEP}} = \sum_{b=1}^B (2M_b C_b \tau_u - C_b \tau_u) \quad (43)$$

Furthermore, the $\mathcal{C}_{\text{COMB}}$ complexity depends on each combiner; hence, for the ZF, RKZF and MMSE combiners the complexities is given by $\mathcal{C}_{\text{COMB}}^{(\text{ZF})}$, $\mathcal{C}_{\text{COMB}}^{(\text{RKZF})}$, and $\mathcal{C}_{\text{COMB}}^{(\text{MMSE})}$, respectively. The number of complex operations to compute the ZF combining matrix is defined as:

$$\mathcal{C}_{\text{COMB}}^{(\text{ZF})} = \sum_{b=1}^B \left(\frac{7}{3} C_b^3 + 3M_b C_b^2 - \frac{1}{2} C_b^2 - \frac{1}{2} C_b \right), \quad (44)$$

while, the complexity for the RKZF is computed by

$$\mathcal{C}_{\text{COMB}}^{(\text{RKZF})} = \sum_{b=1}^B [C_b T_{rKA} (4M_b + 4) + 2C_b^2 + 4M_b C_b - 3C_b] \quad (45)$$

Similarly to [17], we estimate the number of complex operations of the RKZF combiner by computing the most complex steps, indicated in the lines 12, 13 and 18 of Algorithm 2. Lastly, the complexity to compute the MMSE combining matrix is equal to

$$\mathcal{C}_{\text{COMB}}^{(\text{MMSE})} = \sum_{b=1}^B \left(\frac{7}{3} M_b^3 + 3M_b^2 C_b - \frac{1}{2} M_b^2 - \frac{1}{2} M_b \right) \quad (46)$$

IV. NUMERICAL RESULTS

In this section, extensive numerical results for the MSE, variance of XL-channel interference, SE, and EE are provided based on the performance metrics explored in Section III. The main adopted XL-MIMO system and channel parameters are listed in Table I for MSE analysis, Table II for the SE evaluation, and Table III for EE \times SE analysis.

TABLE I: Parameters values adopted for MSE evaluation.

Parameters	Values
System	
# antennas at the BS	$M = 256$
# UEs	$K = [16, 32, 64]$
Loading system	$\mathcal{L} = \frac{K}{M} \in [6.2; 12.5; 25.0]$ [%]
SNR	5 dB
Estimation quality	Perfect CSI
# Monte Carlo realizations	1000
Randomized Kaczmarz Algorithm	
# iteration	$T_{rKZF} = [20 : 300]$
RZF regularization factor	$\xi = 1/\text{SNR}$
Single scattering model	
# clusters	$C = 5$
Antenna spacing	$d_r = 0.0578$ m
Angular spread	$\vartheta = 3\pi/4$ rad
Azimuth angle	$\alpha_i \in \mathcal{U}(-\pi/2, \pi/2)$ rad
# scatterers	$S_i = 10$
Array length	$L = (M - 1)d_r$
VR center	$c_i \sim \mathcal{U}(0, L)$
VR size	$l_i \sim \mathcal{LN}(0.7, 0.2)$
Double scattering model	
# clusters	$C = 5$
Scatterer spacing	$d_s = 5$ m
Antenna spacing	$d_r = 0.0578$ m
Angular spread BS / UE	$\vartheta_i = 3\pi/4$ and $\tilde{\vartheta}_{i,k} = 7\pi/8$ rad
Azimuth angle BS / UE	$\alpha_i, \tilde{\alpha}_{i,k} \in \mathcal{U}(-\pi/2, \pi/2)$
# scatterers (BS-cluster)	$S_i = 10$
# scatterers (UE-cluster)	$S_k = 5$
Array length	$L = (M - 1)d_r$
VR center	$c_i \sim \mathcal{U}(0, L)$
VR size	$l_i \sim \mathcal{LN}(0.7, 0.2)$

A. Mean Squared Error of XL-MIMO Channel Estimates

We evaluate the MSE performance for the RKZF combiner when compared to the traditional RZF. From the parameters described in Table I, the MSE according to the number of iterations is presented in Fig. 2. In this analysis, we consider three channel models: uncorrelated, single-scattering and double-scattering. In all cases, the reduction in the number of users is beneficial for the convergence of the algorithm. Notice that the loading system $\mathcal{L} = \frac{K}{M}$ influences the convergence of the algorithm, presenting an exponential convergence time with increasing loading [23]. Moreover, Fig. 2 also reveals that the channel correlation influences the approximation given by the rKA algorithm. For a uncorrelated channels (unc), the obtained MSE is lower in all cases when compared to the correlated channel estimates. Among the correlated channel models, the single-scattering model presents a higher error estimates when the number of iterations is small; however, it tends to smaller errors than the double-scattering model when the number of iterations increases. Thus, it is seen that the rKA algorithm presents a slow-convergence in terms of MSE of channel estimates when the double model is used, even if

considering different loading systems $\mathcal{L} \in [6.2; 12.5; 25.0]\%$.

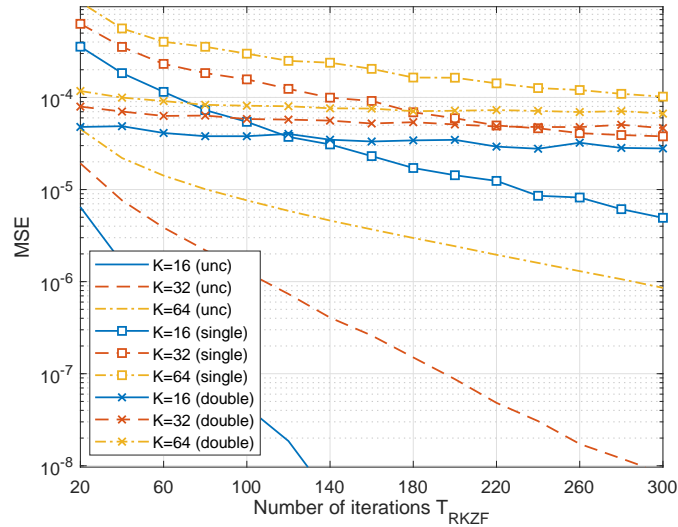


Fig. 2: MSE \times Iterations for the rKA-emulating the RZF combiner, $K \in [16, 32, 64]$ users.

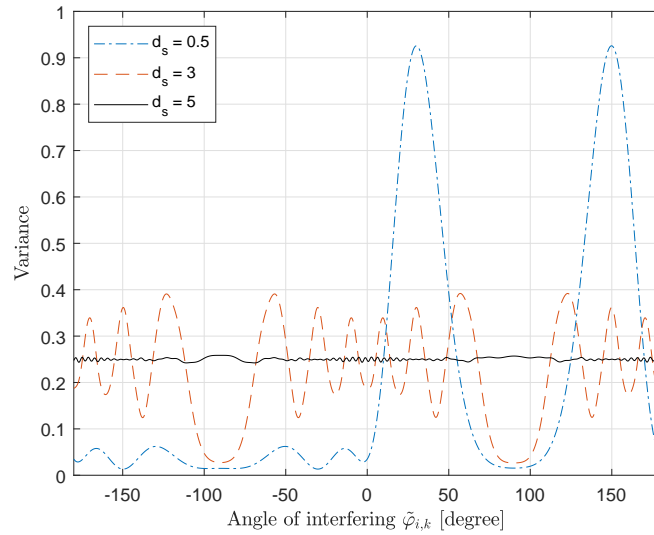
B. Favourable Propagation in XL-MIMO

We evaluate the interference between users at the BS massive antenna array using eq. (30). We consider two users, where the first one has a fixed location while the location of the second user varies angularly. Also, we consider that there is only one BS-cluster, being shared among users. Using eq. (30), the interference obtained are presented in Fig. 3.a) for double-scattering model, and Fig. 3.b) for single-scattering channel model, both evaluations with 2 users. For the analysis of model a), we fixed the user with the angle $\tilde{\varphi}_{i,k}$ of 30° and we varied the second user by $[-180^\circ, 180^\circ]$. In Fig. 3.a), we evaluate how the spacing between the scatterers influences the variance, using three cases: $d_s = [0.5, 3, 5]$ m. We observe higher and lower values of variance when the spacing decreases, where $d_s = 5m$ the variance is $\varsigma_{\ell,k} \approx 0.25$ across the angular range. In addition, we observed that at $d_s = 0.5m$ the highest interference values occur when the interfering angle is equal to 30° or 150° . With higher values of d_s , the correlation between scatterers decreases, and with $d_s = 5m$, the massive channels are approximately uncorrelated from the interfering angle (full favourable propagation condition). However, when the linear scatterers spacing decreases and both users have the near or same angular location, or even if the interfering user is close to the mirror reflection angle $180^\circ - 30^\circ = 150^\circ$, one can observe a very high variance of $\varsigma_{\ell,k} > 0.9$, due to the similarity between the users' correlation matrices. However, when the distance between linear scatterers is reduced, *i.e.*, $d_s < 0.5$, and users are well-separated angularly (spatially localization), one can observe that the channels present near orthogonality, resulting in much less interference $\varsigma_{\ell,k}$ than in other cases. Similar conclusions can be obtained for the single-scattering model in Fig. 3.b).

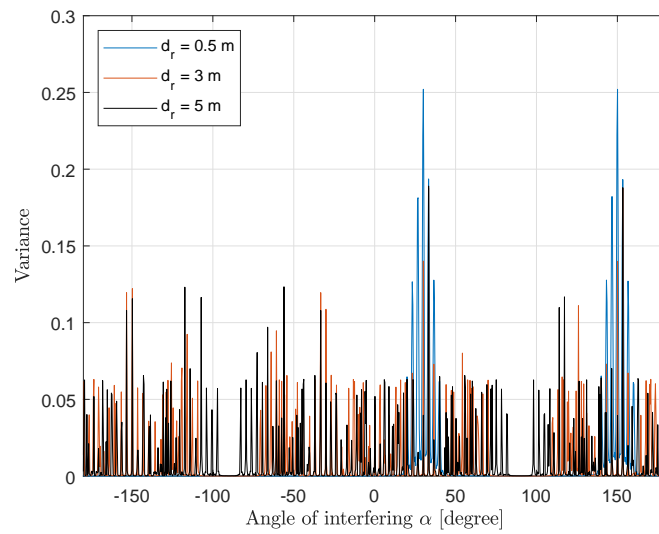
C. Spectral Efficiency in XL-MIMO Single-scattering Model

In this section, we evaluate the SE according to the SNR and the VR length. For the first simulation, we considered the behavior of SE vs SNR for different numbers of clusters, in which the adopted parameter values are described in Table II.

Let's consider two users sharing the same pilot sequence and with the same cluster number. Thus, it was defined that each cluster generates the same length of VR and each VR is positioned as depicted in Fig. 4. Thus, the signal from the



a) Double-scattering model; 2-users.



b) Single-scattering model; 2-users.

Fig. 3: Interference analysis between two users, considering the a) double-scattering b) single-scattering model.

first user is observed by the first (left) antennas and the increase in the number of clusters implies a VR adjacent to the previous cluster. Similarly, we have that the last (right) antennas get visible the signal of the second user and the increase in the number of clusters represents a visualization of the array from the last to the first antennas. Note that the VRs of the same user do not result in overlapping; however, VRs of different users may overlap with the increase in the number of clusters.

The three combiners are evaluated, considering different numbers of clusters per user. To generate each VR as sketched in Fig. 4, we define the center and length of the VR given by c_i and l_i , respectively. The VR center is calculated as $c_i = a_1(L/M) + (l_i/2)$, where a_1 is the first antenna element inside the i th cluster VR. Thus, the interference between users occurs only with $C = 12$ and $C = 16$, and with $C = 8$, the signal of UE 1 is observed by the first half of the array while the signal of UE 2 is observed by the last half of the array. In all configurations, the MMSE performed better than the ZF, as revealed in fig. 5. Indeed, it is observed that the increase from 1 to 8 clusters increased the SE performance

TABLE II: Parameters values adopted for SE \times SNR evaluation.

Parameters	Values
System	
BS antennas	$M = 256$
UEs	$K = 2$
Number of subarrays	$B = 4$
Number of antennas per subarray	$M_b = 64$
SNR _{dB}	$[-10 : 10 : 60]$ dB
SNR	$10^{\text{SNR}_{dB}/10}$
Power noise	$\sigma^2 = 0.05$ W
Power signal	$p_{ul} = \sigma^2 \text{SNR}$
Channel Estimator	MMSE
Length pilot sequence	$\tau_p = 1$ symbol
Length coherence block	$\tau_c = 200$ symbols
Monte Carlo realizations	2000
Single scattering model	
Number of clusters	$C = [1, 8, 12, 16]$
Wavelength	$\lambda = 0.125$ m
Antenna spacing	$d_r = 0.5\lambda$
Angular spread	$\vartheta = [3\pi/4]$ rad
Azimuth angle	$\varphi_i \in \mathcal{U}(-\pi/2, \pi/2)$ rad
Number of scatterers	$S_i = 5$
Array length	$L = (M - 1)d_r$
VR center	$c_i = a_1(L/M) + (l_i/2)$
VR size	$l_i = 0.9$ m (16 antennas)
Constant slop	$\psi = 0.21$ dB/m

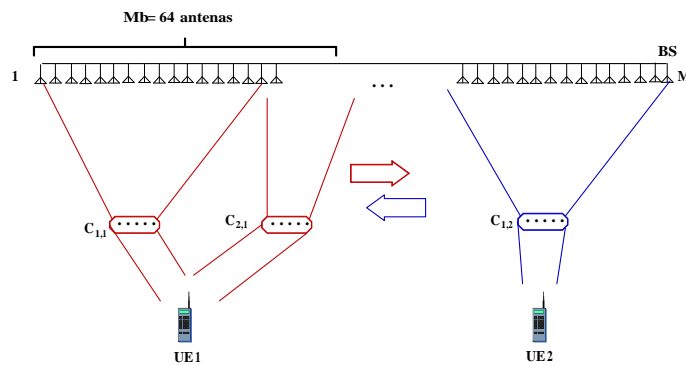


Fig. 4: Sketch of the scenario for the SE versus SNR analysis.

substantially, attaining a huge SE gap of ≈ 37 bit/s/Hz at SNR=60dB with the MMSE w.r.t. the ZF combiner. In these two initial configurations ($C = 1$ and 8), one can observe that increasing the number of clusters without interference between the UEs, it can improve the SE, since a greater number of antennas improve the diversity gain. However, when interference appears (when $C > 8$), in Fig. 5.c) and 5.d), SE performance decreases, because the increase in overlapping VRs results in an increase in the level of interference. Thus, considering the all clusters configurations of Fig. 5, for the worst case of interference, $C = 16$ (all signals from all clusters receive interference), the SE performance is reduced below than for

$C = 1$, where fewer antennas receive the UE signal, but without interference.

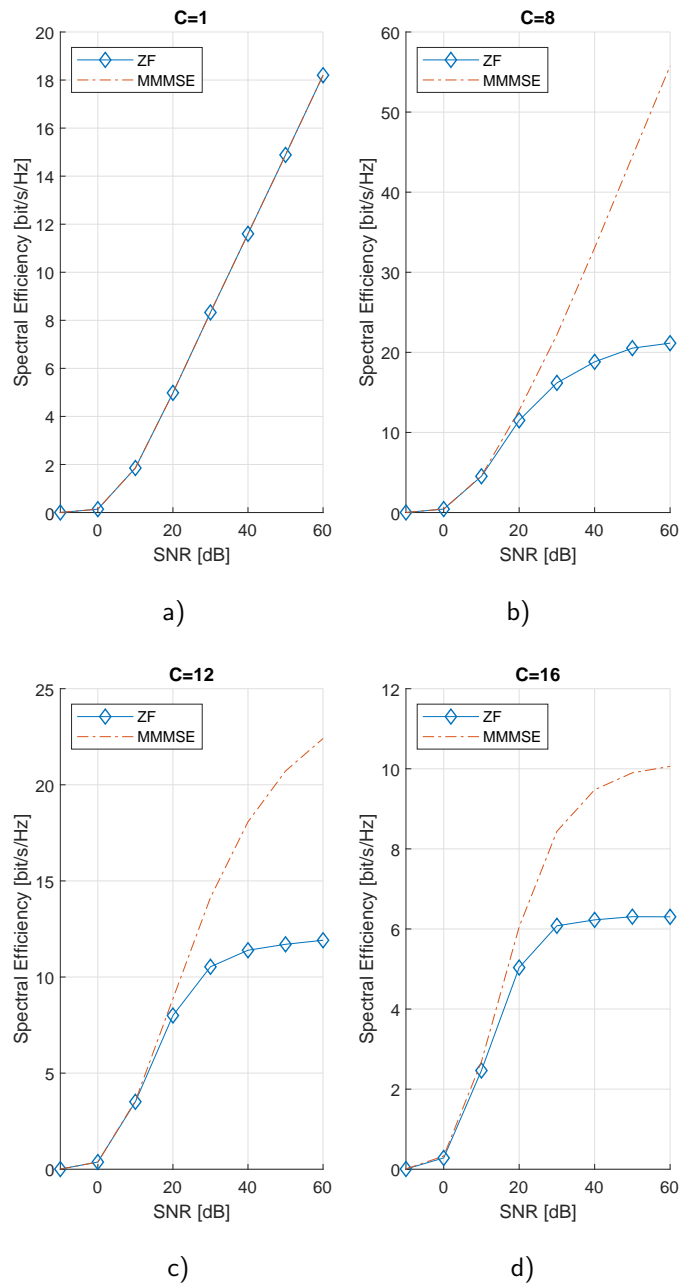


Fig. 5: SE vs SNR, considering the ZF and MMSE combiner, where $C = [1; 8; 12; 16]$ clusters, $M = 256$ antennas.

SE \times VR size: The SE is analyzed according to the number of visible antennas, using the VR length as metric. In this scenario, the *VR length effect* is evaluated, for two users with the second user with different θ . Fig. 6 depicts the SE against VR length, for the RKZF, ZF and MMSE combiners operating under two VR profiles, ρ uniform and triangular, and $\theta = 5^\circ$ or 135° . The case of full VR size, i.e. $M_{\text{VR}} = M$ (massive MIMO configuration) is plotted for reference. In both cases, i.e., $M_{\text{VR}} < M$ and $M_{\text{VR}} = M$, the MMSE combiner resulted in higher SE performance, $\forall M$, compared to the ZF and rKZF combiners. In fact, such behavior is observed due to the possibility of MMSE to better mitigate the inter-user interference, specially increasing when $\theta \rightarrow 0$. We also observed that the increase in the number of clusters results in a reduction in SE.

As the system performance was performed individually for each cluster, it was considered that the signal from the same user, but propagated by different clusters, is seen as interference between them. Thus, the reduction in SE is due to the increase in interference associated with the number of clusters. Despite of that, the SE with MMSE tendency increases unlimitedly with M , while the SE obtained with the ZF and rKZF combiners saturates with M , specially under higher levels of interference (when $\theta \rightarrow 0$, in the analysed 2-user scenario), corroborating the fact that under certain system and channel conditions the MMSE combiner is able to completely mitigate the pilot contamination in asymptotic regime ($M \rightarrow \infty$).

TABLE III: Parameters values adopted for EE, SE $\times M$ analysis.

Parameters	Values
System	
BS antennas	$M = [16 \ 32 \ 64 \ 128 \dots \ 256 \ 512 \ 1024]$
UEs	$K = 2$
subarrays	$B = 4$
antennas per subarray	$M_b = 64$
SNR	10dB
Power noise	$\sigma^2 = 0.05 \text{ W}$
Power signal	$p_{ul} = 0.5 \text{ W}$
Channel Estimator	MMSE
Length pilot sequence	$\tau_p = 1 \text{ symbol}$
Length coherence block	$\tau_c = 200 \text{ symbols}$
Transmission bandwidth	$B_T = 20 \text{ MHz}$
Power amplifier efficiency at the BS	$\kappa^{UL} = 0.5$
Computational efficiency at the BS	$\mathcal{L}_{BS} = 75 \left[\frac{\text{Gflop/s}}{\text{W}} \right]$
Fixed power consumption	$P_{\text{FIX}} = 10 \text{ W}$
Power by local oscillators at BS	$P_{\text{LO}} = 1 \text{ W}$
Power by circuit components at BS	$P_{\text{BS}} = 0.5 \text{ W}$
Power by circuit components at UE	$P_{\text{UE}} = 0.2 \text{ W}$
Power density coding of data signals	$\mathcal{P}_{\text{COD}} = 0.1 \left[\frac{\text{W}}{\text{Gb/s}} \right]$
Power density decoding data signals	$\mathcal{P}_{\text{DEC}} = 0.8 \left[\frac{\text{W}}{\text{Gb/s}} \right]$
Power density for backhaul traffic	$\mathcal{P}_{\text{BT}} = 0.25 \left[\frac{\text{W}}{\text{G/s}} \right]$
Monte Carlo realizations	2000
Randomized Kaczmarz Algorithm	
Number of iteration	$T_{\text{RKZF}} = 20 \text{ iterations}$
RZF regularization factor	$\xi = 1/\text{SNR}$
Single scattering model	
Number of clusters	$C = [1, 4]$
Antenna spacing	$d_r = 0.5\lambda$
Angular spread	$\vartheta = 3\pi/4 \text{ rad}$
Azimuth angle	$\varphi_i \in \mathcal{U}(-\pi/2, \pi/2) \text{ rad}$
Number of scatterers	$S_i = 5$
Array length	$L = (M - 1)d_r$
VR center	$c_i = a_1(L/M) + (l_i/2)$
VR size	$l_i = (MVR - 1)d_r$
Constant slop	$\psi = 0.21 \text{ dB/m}$

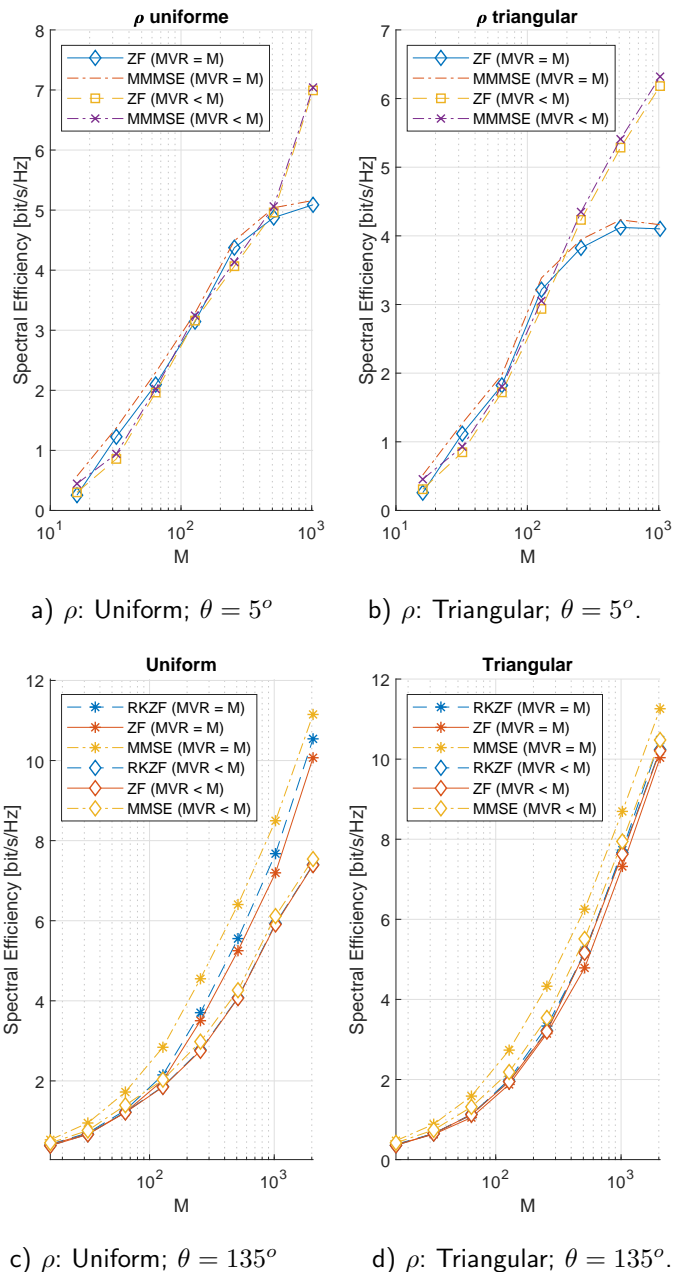


Fig. 6: SE \times VR length, for the RKZF, ZF and MMSE combiners and different VR profiles and θ .

D. Energy Efficiency in XL-MIMO with Linear Combiners

For single-scattering channel model, we evaluate the EE against the number of BS antennas, according to the VR length. Table III summarizes the parameters values adopted for the EE analysis carried out in this subsection. Fig. 7 confirms the best EE value attained with the MMSE combiner for both scenarios: a) massive MIMO condition, when all BS antennas are visible ($M_{\text{VR}} = M$), and b) XL-MIMO with spatial non-stationarities, *i.e.*, when $M_{\text{VR}} < M$. Besides, the MMSE attains higher EE values with less M antenna, *i.e.*, for the power consumption model and values of Table III, the maximum EE achieved with MMSE occurs for $M = 128$ (M-MIMO scenario), and $M = 64$ (XK-MIMO). With the ZF and rKZF combiners, the EE values results reduced and requires more massive antennas M to achieve the maximum EE condition.

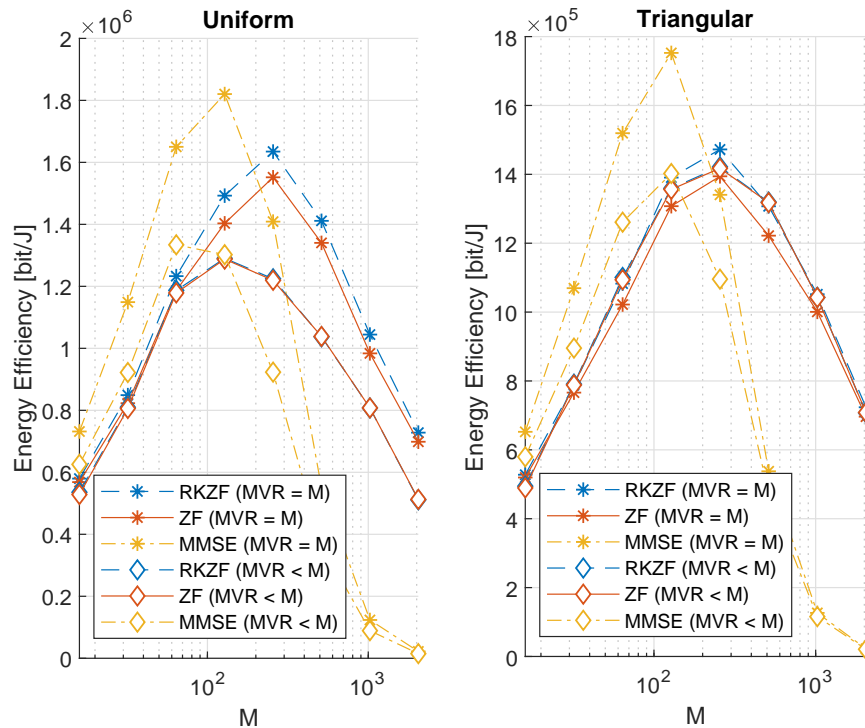


Fig. 7: EE vs VR length, considering the RKZF, ZF and MMSE combiner ($\theta = 5^\circ$).

V. CONCLUSIONS

In this paper we elaborate on the MMSE combiner for XL-MIMO system applications, where the pilot contamination effects have been analysed. We have deployed rKA-based RZF combiner approach aiming at improving the performance-complexity tradeoff of the linear combining schemes for XL-MIMO application scenarios.

Numerical simulation results corroborate that for rKA algorithm application, the number of users is crucial to its performance. Thus, is recommended scenarios, where the number of users is not close to the number of antennas at BS. Also, we observe the possibility to control complexity based on the number of iterations of the rKA algorithm, resulting in the performance quality of the RZF-rKA combiner.

ACKNOWLEDGMENT

This work was supported in part by the Coordenação de Aperfeiçoamento de Pessoal de Nível Superior - Brazil (CAPES) - Finance Code 001, in part by the National Council for Scientific and Technological Development (CNPq) of Brazil under Grant 304066/2015-0, and by the Fundação Araucária under Grant PBA-3673/2016.

REFERENCES

- [1] A. Ali, E. D. Carvalho, and R. W. Heath, "Linear receivers in non-stationary massive MIMO channels with visibility regions," *IEEE Wireless Communications Letters*, vol. 8, no. 3, pp. 885–888, Jun. 2019.
- [2] A. Amiri, M. Angelichinoski, E. de Carvalho, and R. W. Heath, "Extremely large aperture massive MIMO: Low complexity receiver architectures," in *2018 IEEE Globecom Workshops (GC Wkshps)*, 9–13 Dec. 2018, pp. 1–6.
- [3] A. Amiri, C. N. Manch'on, and E. de Carvalho, "Deep learning based spatial user mapping on extra large MIMO arrays," *arXiv 2002.00474*, Feb. 2020.

- [4] V. C. Rodrigues, A. Amiri, T. Abrão, E. de Carvalho, and P. Popovski, "Low-complexity distributed XL-MIMO for multiuser detection," in *2020 IEEE International Conference on Communications Workshops (ICC Workshops)*, 7-11 Jun. 2020, pp. 1–6.
- [5] Y. Han, S. Jin, C.-K. Wen, and X. Ma, "Channel estimation for extremely large-scale massive MIMO systems," *IEEE Wireless Communications Letters*, vol. 9, no. 5, pp. 633–637, Jan. 2020.
- [6] E. Björnson, J. Hoydis, and L. Sanguinetti, "Massive MIMO has unlimited capacity," *IEEE Transactions on Wireless Communications*, vol. 17, no. 1, pp. 574–590, Jan. 2018.
- [7] L. May Taniguchi and T. Abrão, "Stochastic channel models for massive and extreme large multiple-input multiple-output systems," *Transactions on Emerging Telecommunications Technologies*, vol. 31, no. 9, p. e4099, Aug. 2020.
- [8] A. Amiri, S. Rezaie, C. N. Manchon, and E. de Carvalho, "Distributed receivers for extra-large scale MIMO arrays: A message passing approach," *arXiv. 2007.06930*, Jul. 2020.
- [9] J. C. Marinello, T. Abrão, A. Amiri, E. de Carvalho, and P. Popovski, "Antenna selection for improving energy efficiency in XL-MIMO systems," *IEEE Transactions on Vehicular Technology*, vol. 69, no. 11, pp. 13 305–13 318, Sep. 2020.
- [10] J. H. I. de Souza, A. Amiri, T. Abrão, E. de Carvalho, and P. Popovski, "Quasi-distributed antenna selection for spectral efficiency maximization in subarray switching XL-MIMO systems," *arXiv 2102.11438*, Feb. 2021.
- [11] M. N. Boroujerdi, S. Haghghatshoar, and G. Caire, "Low-complexity statistically robust precoder/detector computation for massive MIMO systems," *IEEE Transactions on Wireless Communications*, vol. 17, no. 10, pp. 6516–6530, Oct. 2018.
- [12] T. L. Marzetta, "Noncooperative cellular wireless with unlimited numbers of base station antennas," *IEEE Transactions on Wireless Communications*, vol. 9, no. 11, pp. 3590–3600, Nov. 2010.
- [13] L. Sanguinetti, E. Björnson, and J. Hoydis, "Toward massive MIMO 2.0: Understanding spatial correlation, interference suppression, and pilot contamination," *IEEE Transactions on Communications*, vol. 68, no. 1, pp. 232–257, Jan. 2020.
- [14] Jq. Chen, Z. Zhang, T. Tang, and Yz. Huang, "A non-stationary channel model for 5G massive MIMO systems," *Frontiers of Information Technology & Electronic Engineering*, vol. 18, no. 12, pp. 2101–2110, Dec. 2017.
- [15] E. D. Carvalho, A. Ali, A. Amiri, M. Angjelichinoski, and R. W. Heath, "Non-stationarities in extra-large-scale massive MIMO," *IEEE Wireless Communications*, vol. 27, no. 4, pp. 74–80, Aug. 2020.
- [16] C. Oestges and B. Clerckx, *MIMO Wireless Communications: From Real-World Propagation to Space-Time Code Design*. Elsevier Science, 2007.
- [17] V. C. Rodrigues, J. C. Marinello Filho, and T. Abrão, "Randomized Kaczmarz algorithm for massive MIMO systems with channel estimation and spatial correlation," *International Journal of Communication Systems*, vol. 32, no. 18, p. e4158, Sep. 2019.
- [18] E. Björnson and L. Sanguinetti, "Making cell-free massive MIMO competitive with MMSE processing and centralized implementation," *IEEE Transactions on Wireless Communications*, vol. 19, no. 1, pp. 77–90, Jan. 2020.
- [19] Q.-U.-A. Nadeem, A. Kammoun, M. Debbah, and M.-S. Alouini, "Asymptotic analysis of rzf over double scattering channels with mmse estimation," *IEEE Transactions on Wireless Communications*, vol. 18, no. 5, pp. 2509–2526, 2019.
- [20] T. L. Marzetta, E. G. Larsson, H. Yang, and H. Q. Ngo, *Fundamentals of Massive MIMO*. Cambridge University Press, 2016.
- [21] E. Björnson, L. Sanguinetti, J. Hoydis, and M. Debbah, "Optimal design of energy-efficient multi-user MIMO systems: Is massive MIMO the answer?" *IEEE Transactions on Wireless Communications*, vol. 14, no. 6, pp. 3059–3075, Jun. 2015.
- [22] J. C. M. Filho, C. Panazio, T. Abrão, and S. Tomasin, "Total energy efficiency of TR-MRC and FD-MRC receivers for massive MIMO uplink," *IEEE Systems Journal*, vol. 13, no. 3, pp. 2285–2296, Sep. 2019.
- [23] K. B. Rosa, J. C. Marinello, and T. Abrão, "Low-complexity Kaczmarz precoding in DL massive MIMO with partial CSI and correlation," *Physical Communication*, vol. 37, p. 100902, Dec. 2019.